Finite Element Parametric Study Involving the Effect of Cooling Channels on the Thermo-mechanical Behavior of a High Pressure Airplane Turbine Blade

Ricardo Pedro Arraial Mendes

Thesis to obtain the Master of Science Degree in

Mechanical Engineering

Supervisors:	Prof. Augusto Manuel Moura Moita de Deus
	Prof. Virgínia Isabel Monteiro Nabais Infante

Examination Committee

Chairperson:	Prof. Luís Filipe Galrão dos Reis
Supervisor:	Prof. Augusto Manuel Moura Moita de Deus
Member of the Committee:	Prof. Maria de Fátima Reis Vaz

November 2021

Acknowledgements

First, I would like to thank my co-supervisor, Professor Virgínia Infante, for suggesting this thesis to me, for the valuable advice, but mainly for giving me another opportunity.

Second, and certainly not least, I would like to thank my supervisor, Professor Augusto Moita de Deus, for accompanying me in this project, for his suggestions, understanding, patience, for his willingness to help and for always pointing me in the right direction. And also for his great taste in music and football clubs.

I would like to thank Engineer Pedro Viveiros from SATA Air Açores for providing me with the materials and information necessary for the development of this project. Also from SATA, I would like to thank Dr. Filipe Raposo, for supplying me with additional information required to complete this study.

I would like to thank Engineer Pedro Brandão, the author of the Master of Science degree thesis to which this project is a continuation, for his excellent work and for providing a very solid base on which I could build my thesis.

I would also like to thank and dedicate this work to the following people who have helped me out along the way, in one way or another:

To Dr. Margarida Casimiro, for lending me her ears (poor things!), for the useful advice and for her friendship;

To my Aunt Telminha, for the continuous support and for providing me a Home away from Home;

To Bruno and Juliana, for their friendship, comradery, for the laughs and for being my social pillow; a special word to my Dear cousin Juliana who, more than anyone, has been my main company and foundation for the better part of a decade – Love you to bits, Jupac!

To my nieces, Joana and Margarida, for always making me laugh, even when they're not too happy about it;

To my sister Susana, for pushing me to be a better version of myself and for the tough love;

And finally, to my parents, for being the radio beacon that never allowed this aircraft to get too lost or stray too far away from its homebase.

Resumo

Na indústria competitiva da aviação, as aeronaves operam em horários apertados e em condições de trabalho extremas. Os componentes de motores de turbina a gás são solicitados a elevadas temperaturas e velocidades de rotação, sendo a turbina de alta pressão particularmente afetada por altas temperaturas. Para o contrariar, são introduzidos mecanismos de arrefecimento de forma a baixar as temperaturas das pás de turbina de alta pressão e assegurar a sua estabilidade mecânica.

O objetivo deste trabalho é estudar a influência do modo de arrefecimento na temperatura e deformação da pá. Para isto, foi criado um modelo da pá usando o método dos elementos finitos.

Para o concretizar, uma pá de turbina descartada foi facultada por uma companhia aérea regional e uma rota aérea operada pela mesma companhia foi estudada, sendo a informação relativa às condições de voo a que a turbina está sujeita obtida através dos registos de voo.

Um modelo CAD 3D da pá de um motor similar foi obtido e adaptado, tendo servido como base do modelo de elementos finitos da pá.

Foram efetuadas análises térmicas e de fluência num bloco rectangular de teste, de modo a validar o modelo, que depois foi aplicado ao modelo da pá.

As simulações efetuadas no modelo da pá, apesar das aproximações feitas, geraram resultados satisfatórios e este modelo demonstrou ser útil na análise de temperaturas, deslocamentos e em apresentar uma previsão da deformação da pá no fim da sua vida útil.

Palavras-Chave

Pá de Turbina de Alta Pressão, Método dos Elementos Finitos, Fluência, Temperatura, Arrefecimento, Deformação.

Abstract

With the competitiveness of the airline industry, aircrafts have to operate on tight schedules and extreme work conditions. Gas turbine engine components function under conditions of high temperatures, pressure and rotation speeds, with the high pressure turbine (HPT) experiencing some of the highest temperatures. To counter this, cooling mechanisms are introduced in order to lower the temperatures of the HPT blades and therefore assure their mechanical stability.

The objective of this work is to study the cooling mechanisms' influence on the temperature and deformation of an HPT blade. To do so, a blade model was created using the finite element method (FEM).

To create the model, a blade scrap was obtained from a regional airline company. Also, a flight route operated by the same company was studied and information regarding the flight conditions of the turbine was retrieved from flight data records.

A CAD 3D blade model from a similar engine was obtained, adapted and served as the basis of the FEM blade model created.

After the data input, thermal and creep analyses were run on a rectangular block in order to validate the model, and were then performed on the blade model.

The simulations run were successful and, despite the assumptions and approximations made, the blade model offered reasonable results and proved itself a useful model in analyzing temperatures, displacements and predicting the deformation by the end of the blade's lifetime.

Keywords

Table of Contents

List of Tables

x

List of Figures

List of Symbols

A	Surface Area
$\mathbf{C_p}$	Specific Heat Capacity
E	Young's Modulus
e	Elongation
E22	Longitudinal Strain Component
G	Shear Modulus
h	Cooling Flow Convection Coefficient
hc	Surface Film Cooling Flow Convection Coefficient
he	Heating Flow Convection Coefficient
heb	Platform Heating Flow Convection Coefficient
hec	Averaged Heating Flow Convection Coefficient
hecx	Convex Surface Heating Flow Convection Coefficient
hecv	Concave Surface Heating Flow Convection Coefficient
het	Blade Tip Heating Flow Convection Coefficient
hev	Variable Heating Flow Convection Coefficient
k	Thermal Conductivity
$\mathbf{K_1}$	Temperature Dependent Material Constant
n	Creep Stress Exponent
$\boldsymbol{q''}$	Convective Heat Transfer Rate
$\mathbf{Q_c}$	Activation Energy for Creep
s	Seconds
S22	Longitudinal Stress Component
SMises	von Mises Stress
T	Temperature
Te	Heating Flow Temperature
$\mathbf{T_m}$	Melting Point Temperature
$\mathbf{T_s}$	Surface Temperature
$\boldsymbol{T_\infty}$	Temperature of the Enveloping Fluid
U2	Longitudinal Displacement
UMag	Displacement Magnitude

Greek

α	Mean Thermal Expansion Coefficient
ε_{pl}	Plastic Strain
$\dot{\varepsilon}_s$	Creep Strain Rate
ν	Poisson's Ratio
ρ	Density
σ	Stress
$\sigma_{0.2}$	0.2% Proof Stress
σ_{UTS}	Ultimate Tensile Stress
ω_{HPT}	HPT Rotation Speed in Radians Per Second

Abbreviations

CAD	Computer-Aided Design
CAE	Complete Abaqus Environment
CBC	Convection as Boundary Condition
EAT	Exterior Atmospheric Temperature
FDR	Flight Data Record
FEM	Finite Element Method
HP	High Pressure
HPT	High Pressure Turbine
LP	Low Pressure
PT	Power Turbine
TBC	Temperature as Boundary Condition
TIT	Turbine Inlet Temperature
UTS	Ultimate Tensile Stress

1. Introduction

The aviation mode of transport has become increasingly more common and accessible in these current times. The air transport industry has radically changed over the last twenty years. New firms, like low-cost airline companies, have been benefitted by the liberalization and deregulation of the aviation sector [1]. The adding of these companies, to the traditional and more established airline companies, has led to an increase of competition and innovation in this industry. Eager to provide the customer with the widest range of offers – from low fares to comfortability – airline companies make the most of the aircrafts in their fleet, taking advantage of them to the limits of their capacities.

With the high competitiveness of the airline industry, aircrafts have to operate, on a daily basis, on tight schedules and under extreme work conditions. Gas turbine engine components function under conditions of very high temperatures, pressure and rotation speeds, with the ultimate goal of extracting the necessary energy from a gas flow to power the aircraft.

In a gas turbine engine, the components that are under the most rigorous conditions are the combustion chamber and the high pressure turbine, with this section of the engine working under the influence of the highest temperatures in the engine. These high temperatures though, particularly the turbine inlet temperatures, are necessary and must be elevated so that it is possible to increase the power output and thermodynamic efficiency of the engine [2] [3]. In this situation, the high pressure turbine blades usually operate at temperatures that could reach their constituting materials' maximum service temperature. To counter this effect, it is vital to introduce cooling mechanisms in order to lower the temperatures of the turbine blades and therefore assure their mechanical integrity [2] [4].

This thesis work's main objective is to study the cooling mechanisms' influence in the overall temperature of a turbine blade, as well as the effect that such temperature decrease can have on the overall deformation of the blade.

This study gives sequence to a previous Master of Science degree thesis made by Pedro Brandão [2] at Instituto Superior Técnico. In it, a predictive model was built in order to study the effects that the mechanical and thermal loads have on the turbine blades for several flight routes performed by a regional airline company that flies within the Azores islands and also between the island of São Miguel and the island of Madeira. To do so, in-flight information was retrieved from the flight data record (FDR) for several flight routes, and by the use of a finite element software, a blade model without cooling mechanisms was created, and several analyses were performed in order to determine the level of creep that the blades experience, and also to predict their creep behavior by the end of their 3000 flight-hours lifetime [2].

The contribution of this current thesis is the creation of a new blade model, using the finite element method (FEM), in which the cooling mechanisms' influence is considered. To create the FEM blade model, a CAD 3D blade model from a similar engine was adapted until its dimensions were very close to those of a turbine blade scrap obtained from the regional airline company.

The PDL-FNC (São Miguel Island – Madeira Island) flight route was the object of the study, and its FDR data (temperatures and rotation speeds) was retrieved from the former thesis, as well as the

blade material's properties, and this information was used in the construction of the blade model for this work.

In order to study how the cooling can influence the blade's temperature and deformation, thermal and creep analyses were performed using the finite element software ABAQUS, with the thermal analyses being run using two different approaches. Both the thermal and creep analyses were initially tested and validated in several rectangular block models with similar dimensions to the blade.

With both the thermal and creep analyses properly defined in the blade model, a study on the accumulation of flight cycles was performed in order to predict the deformation of the blade by the end of its lifetime.

Thesis Outline

This thesis is divided into five Chapters:

- In Chapter 1, an introduction to this study is made, and the background, motivation for the study and main objectives are presented;
- In Chapter 2, a brief state of the art is made;
- In Chapter 3, the methods, data and other information necessary for the making of this study are presented;
- In Chapter 4, the results obtained are presented, analyzed and discussed;
- In Chapter 5, conclusions are drawn regarding the results obtained, and suggestions for future work are made.

2.State of the Art

2.1. Gas Turbine Engine

The Bombardier DHC8-Q400 is a turboprop aircraft that is equipped with a PW150A gas turbine engine from the manufacturer Pratt & Whitney. A gas turbine is an internal combustion engine based on the Brayton cycle, which is a thermodynamic cycle that extracts energy from a fuel and flowing air and uses it to generate usable mechanical work. This engine has three main components: a compressor, a combustion chamber and a turbine, as can be seen in **Figure 2.1**. [5]
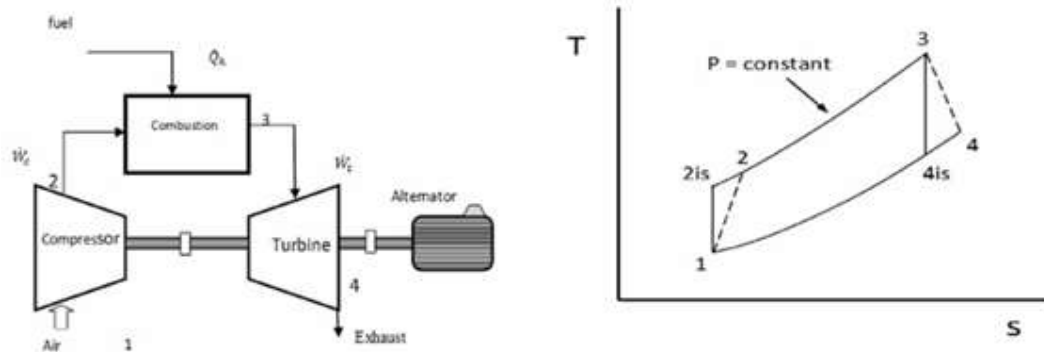
Figure 2.1 - Air-standard Brayton cycle [6]

Atmospheric air is drawn into the compressor where its pressure is increased. This compressed air enters the combustion chamber where it is ignited by fuel injected into the air. The high-temperature and pressurized gas enters a gas turbine where it is expanded and produces shaft work. A portion of the shaft work, which is the total work output of the turbine, is extracted to operate the compressor. The remainder of the shaft work is made available as the net-work output of the engine – this energy, which is provided by the exhaust gases, can be reutilized for external work, like producing thrust in a turbojet engine, or for the rotation of a second turbine – or power turbine - that is connected to a fan or a generator.

From **Figure 2.1**, it is also possible to observe how the Brayton cycle models the gas turbine cycle. The first process in this cycle is the isentropic compression process (state 1 – state 2is) in which the atmospheric air is compressed to a high pressure. The second process is the heat addition at constant-pressure (state 2is – state 3) in which the compressed air is heated in the combustion chamber. The third process is the isentropic expansion process (state 3 – state 4is) in which the high-pressure and high-temperature air is expanded until it reaches the atmospheric pressure.

It is important to note that both the isentropic compression process and the isentropic expansion process are ideal processes, in which both the compressor and turbine efficiencies are 100%. Realistically, the efficiencies of both the compressor and turbine have to be taken into account and, therefore, neither the compression nor the expansion process can be considered isentropic. As can be

seen in **Figure 2.1,** the compression process in the actual cycle goes from state 1 to state 2 and the expansion process from state 3 to state 4. [7] [8]

2.1.1. Turboprop

The turboprop is a type of engine that generates thrust and also moves a propeller. Propeller engines develop thrust by moving a significant amount of air through a small change in velocity. This type of engine is very efficient at low speeds (less than 725 Km/h) and is particularly adequate to short-distance travel, being mostly used for low-speed transport aircraft and cargo planes.

A turboprop engine is composed of an intake, a reduction gearbox, a compressor, a combustion chamber, a turbine and a propelling nozzle, as can be seen in **Figure 2.2**. [9] [10]
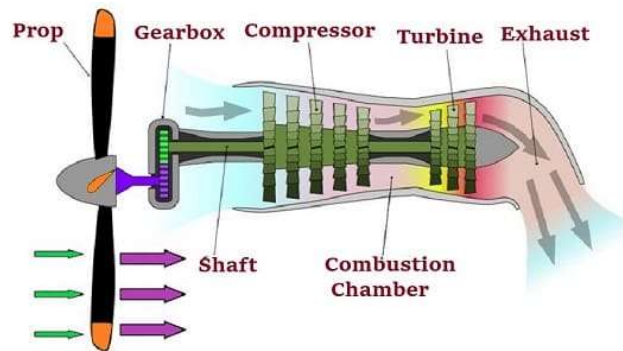
Figure 2.2 - Turboprop gas turbine engine [10]

Turboprop propulsion systems have two main parts, the core engine and the propeller. Unlike the turbojet core engine, which produces the necessary thrust to propel the aircraft forward by expanding all the hot exhaust air through the nozzle, the turboprop core engine uses most of the energy of the exhaust to rotate the turbine. An additional turbine - the previously mentioned power turbine - is connected to a drive shaft. This drive shaft is connected to the reduction gearbox, which in turn is connected to the propeller that generates most of the thrust that drives the aircraft forward. A portion of the exhaust air produces some thrust, but most of the energy of the exhaust is used to turn the drive shaft and, therefore, almost all of the engine's power is directed to drive the propellers. [9] [10]

2.1.2. PW150A Turboprop Engine

The PW150A gas turbine engine, especially designed for the Bombardier DHC8-Q400 aircraft, is composed of two modules, the reduction gearbox module and the turbomachinery module, as can be seen in **Figure 2.3**.
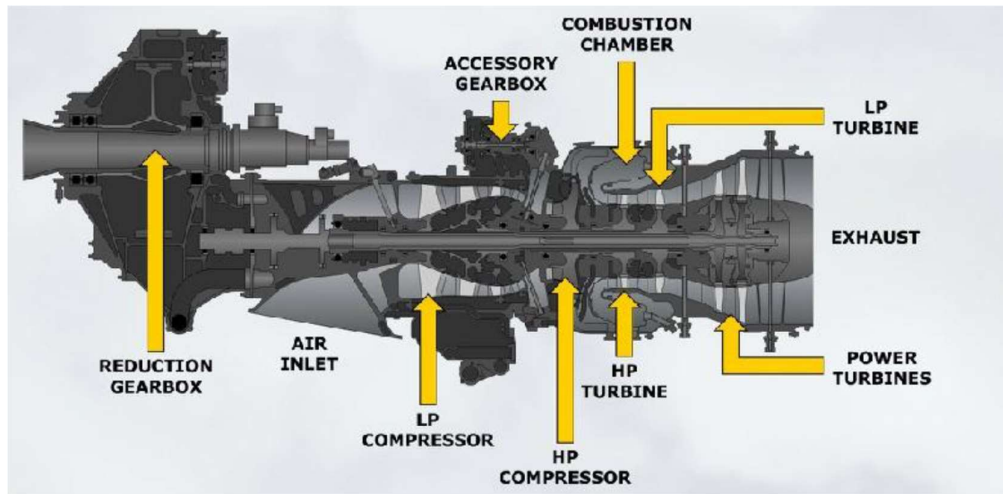
Figure 2.3 - PW150A turboprop gas turbine engine [11]

The reduction gearbox's function is to reduce the power turbine input and increase the torque. The turbomachinery module is composed of an air inlet, a compressor section (LP compressor and HP compressor), a combustion chamber and a turbine section. This module is responsible for generating power that, via the reduction gearbox, will enable the rotation of the propeller and generate the thrust necessary to propel the aircraft forward. [2] [12]

Considering that the main purpose of this work is to study the thermo-mechanical behavior of an HPT blade, a larger focus was given to the turbine section, and more specifically to the HP turbine and the HPT blades.

Turbine Section

The turbine section is composed of all the turbines contained in the engine (in a turbine support case). These turbines are the high pressure (HP) turbine, the low pressure (LP) turbine and the power turbines [13]. A schematic of this section can be seen in **Figure 2.4.**

As previously explained, the turbines extract energy from the expanding gases that derive from the combustion chamber. This energy, in turn, is converted into shaft horsepower that will be used to operate the compressors and the propeller. The hot high pressure gases exit the combustion chamber and are directed initially through the HP turbine. After exiting the HP turbine, the gases enter the LP turbine and are then finally directed to the power turbines.

It is of interest to note that both the HP and LP turbines power the HP and LP compressors respectively, by means of their own respective shafts, while the power turbines operate the propeller by means of the power turbine shaft and the reduction gearbox. These three shafts are concentric and turn independently from each other. When the engine starts, only the HP compressor and HP turbine begin to operate. The HP turbine rotates clockwise (from the pilot's point of view) to a maximum speed

of 31150 rpm, the LP turbine rotates counterclockwise to a maximum speed of 27000 rpm, and the power turbine rotates clockwise to a maximum speed of 17501 rpm. [2] [14]

LEGEND
1. HP Vane.
2. HP Turbine.
3. LP Turbine.
4. PT Vanes.
5. Combustion Chamber.
6. LP Vane.
7. Power Turbines.
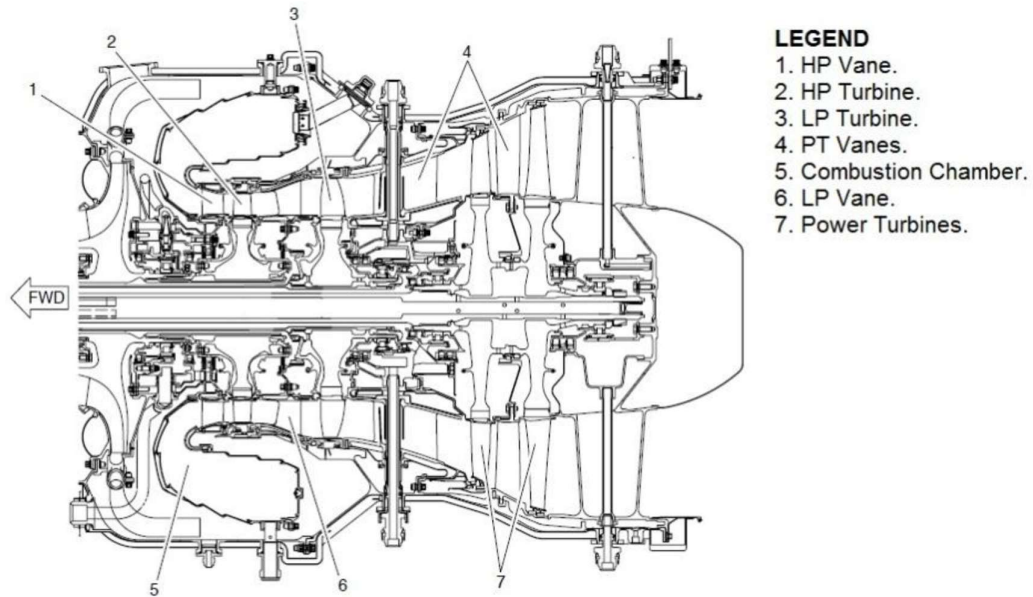
Figure 2.4 - Turbine Section [14]

HP turbine and HPT blades

The HP turbine is a nickel alloy disc in which are distributed 41 air cooled blades, as can be seen in **Figure 2.5**. [2] [14]
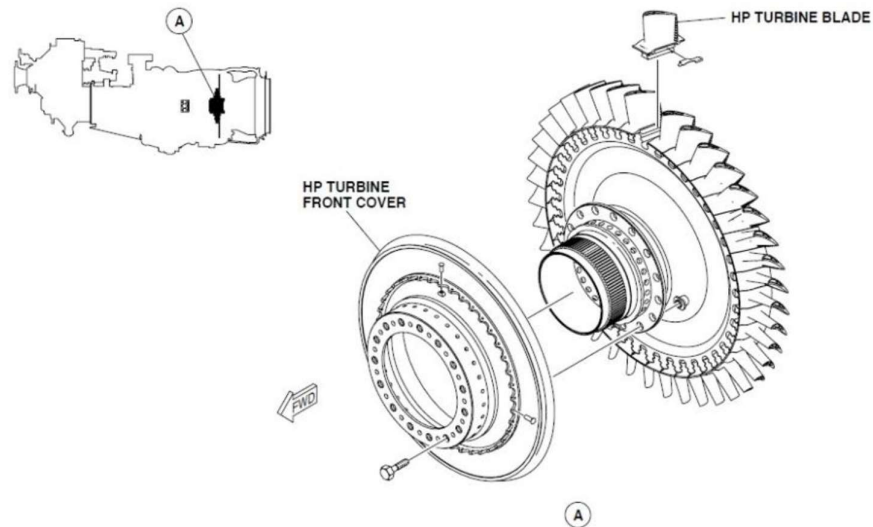
Figure 2.5 - HP Turbine [14]

The HPT blades' material is a single-crystal nickel-based superalloy, as it is a material capable of withstanding high temperatures and also possesses high creep strength. An HPT blade can be seen in **Figure 2.6.** [2] [15]

Figure 2.6 - HPT Blade [16]

Because the HPT blades are exposed to a very harsh environment in terms of temperature, which can reach its material's maximum service temperature, cooling mechanisms have to be employed in order to lower the blade's temperatures [4]. The HPT blades in use in the PW150A engine are cooled by cooling air provided through showerhead, tip and platform cooling holes with trailing edge ejection. A schematic of several cooling techniques can be seen in **Figure 2.7**. [14]
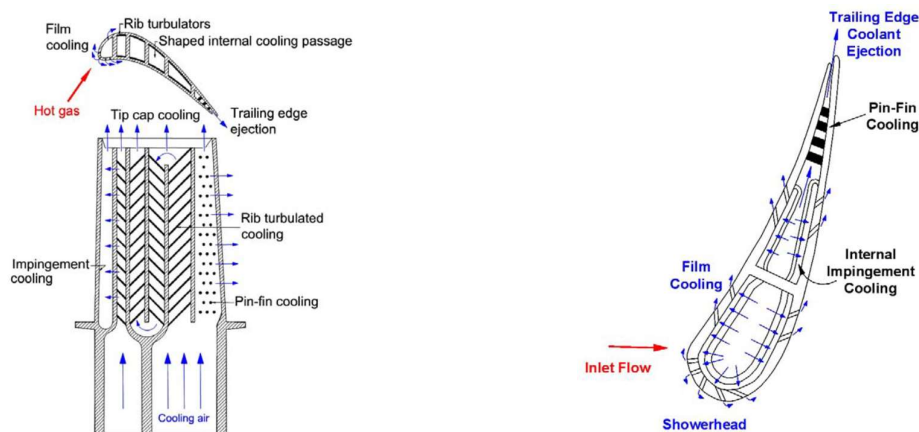
Figure 2.7 - Schematic of cross-sections of a turbine blade with common cooling techniques [17]

From **Figure 2.7** it is possible to observe that each section of the HPT blade - leading edge, mid-body, trailing edge – whether internally or on the surface, has its own suitable cooling technique.

For the leading edge, where the heat loads are the highest in all the blade, impingement cooling is the technique most commonly used. This technique consists in striking/impinging the inner blade wall with internal high-velocity cooling air jets.

For the mid-body, impingement cooling can also be used, though the most widely used method of cooling is through the internal distribution of a cooling air flow that circulates through cooling passages that follow a serpentine-like geometry.

The trailing edge, due to manufacturing constraints as this is the narrowest section of the blade, is cooled by means of pin-fin cooling. In a pin-fin array, there is the transfer of heat from both the smooth channel endwall and the multitude of pins that connect the opposing walls. The cooling air flows through the array of pins allowing for heat transfer to occur.

As for the surface, it is cooled via the film cooling technique. In this method, the cooling air exits the internal passages through cooling holes (showerhead) and forms an insulating film of cool air that covers and partially protects the external blade surface from the influence of the hot gas. [4] [17] [18] [19]

2.2. Creep

As seen in **Subchapter 2.1**, HPT blades are subjected to extremely high temperatures and stresses. In these conditions, the main mode of deformation of the HPT blades can be attributed to creep.

Creep is a time-dependent deformation under an applied load and usually occurs at high temperatures, though it can also happen at room temperature in certain materials, although at a much slower rate. This rate of deformation continues with time and under stresses that are inferior to the yield strength of the metals and alloys being subjected to the applied loads.

As a result of creep, the material goes through an increase in length, which could be hazardous while in service, especially for an HPT blade, as it can, in very rare cases, elongate enough that their tips come into contact with the casing, making the replacement of both parts a necessity. [2] [20] [21]

Creep can be represented by a creep curve and the rate of deformation, or creep rate, can be defined as a creep strain vs. time curve, as can be seen in **Figure 2.8**.
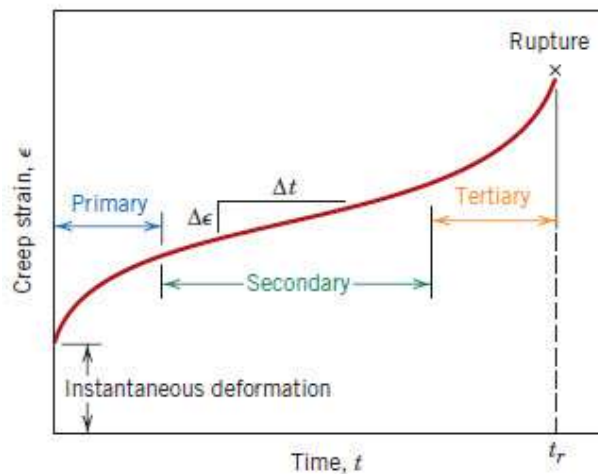
Figure 2.8 - Creep Curve [22]

From **Figure 2.8** it is possible to observe that there are three distinct creep stages at play, after an initial instantaneous deformation.

The first stage, which is the primary creep stage, is of a transient nature and starts at a rapid rate and slows down as time progresses. In this stage there is the occurrence of work hardening which in turn leads to a decrease of the creep strain rate until it reaches a constant.

The second stage, the secondary creep stage, has a relatively uniform rate and begins when the strain rate has stabilized at the end of the primary stage and becomes a constant. During this stage, the creep strain rate is at a minimum due to the attaining of a balance between the work hardening rate and the recovery rate. This stage, being the longest and most uniform of the stages, characterizes the material's creep rate as a function of stress and temperature.

The third stage, the tertiary creep stage, is the final phase of the creep deformation process. This stage is characterized by an accelerated creep strain rate which leads in the end to the occurrence of material fracture. It begins when damage to the microstructure of the material takes place and voids in the grain boundaries expand to form microcracks. As these microcracks grow they interconnect, reducing the load-bearing cross-sectional area which ultimately leads to the complete failure of the material. [2] [20] [21]

As noted earlier, creep is a time-dependent deformation under an applied load and usually occurs at high temperatures. Therefore, it is important to define how temperature and stress can affect the behavior of the creep strain curves. This influence of temperature and stress on the creep strain curves can be seen in **Figure 2.9**
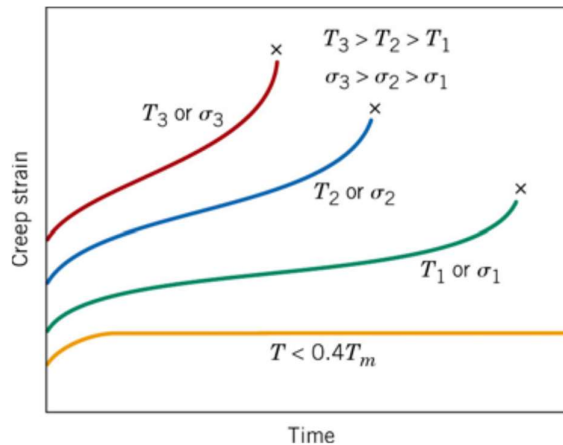
Figure 2.9 - Influence of temperature and stress on creep strain [23]

When it comes to temperature, it is possible to observe that creep in metals only becomes important at temperatures above 0.4 T_m, where T_m is the melting point temperature of the material.

With the increase of stress and temperature, as can be seen in **Figure 2.9** there is a consequential increase of the initial instantaneous deformation. Also observable is a reduction of both the primary and secondary creep stages as the steady-state creep strain rate increases. This

ultimately leads to a decrease of the time it takes for the material to rupture, emphasizing the influence that the temperature and stress has over the creep strain rate. [24]

2.3. Convection Heat Transfer

As previously mentioned, HPT blades operate under very high temperatures. Taking this into consideration, it is important to understand the basic principles of the heat transfer mechanisms that have an effect on the temperature distribution of the HPT blades, most specifically heat transfer by convection.

Heat transfer can be defined as the process of thermal energy being transferred due to a temperature difference between two systems. Whenever there is a gradient in temperatures, heat transfer must occur. The amount of thermal energy available in a system is determined by temperature and heat transfer is achieved by means of a heat flow that represents the movement of thermal energy.

There are three different types of heat transfer methods: conduction, convection and radiation.

Conduction is the most common method of heat transfer. It occurs through physical contact in both solids and fluids, whenever a temperature gradient exists in a stationary medium.

Radiation is the transmission of energy from one surface to another by means of the emission of electromagnetic waves, irrespective of an intervening medium. This phenomenon occurs as all surfaces emit energy by electromagnetic radiation. [25] [26] [27]

The third method of heat transfer is convection, and this method is the most relevant to this study, particularly concerning the cooling mechanisms of the HPT blade.

Convection heat transfer occurs between a fluid in movement and a surface when the two are at different temperatures. There are two methods of convection heat transfer which can be characterized by the nature of the flow: natural convection and forced convection.

Natural convection is generated by natural buoyancy forces that originate due to density differences caused by temperature variations in the fluid. For example, when a fireplace is lit, the surrounding air increases in temperature which leads to its expansion and a reduction of its density. This, in turn, originates the movement of fluid as the hotter less dense fluid tends to rise and the denser fluid sinks due to the effect of gravity, as can be seen in **Figure 2.10** [25] [28]
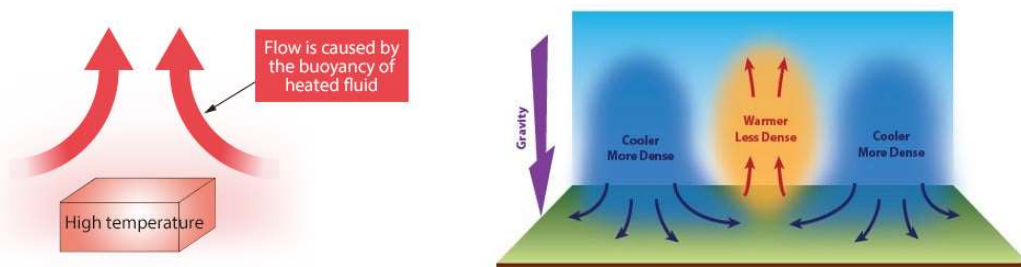
Figure 2.10 – Natural Convection [29] [30]

Forced convection occurs when a fluid is forced to flow due to external means, such as a fan or a pump. This method of heat transfer is particularly effective in allowing the transportation of considerable amounts of heat energy. It is therefore the principal method of cooling that the HPT blade goes through.

Regardless of the method of convection, the heat transfer rate can be defined by the equation

$$q'' = hA(T_\infty - T_S) \tag{2.1}$$

where q'' is the convective heat transfer rate, h is the convection heat transfer coefficient, A is the surface area of the object being cooled or heated, T_∞ is the temperature of the enveloping fluid and T_S is the surface temperature of the object. [25] [28]

This equation is also known as Newton's law of cooling and the convection heat transfer method can be observed in **Figure 2.11**
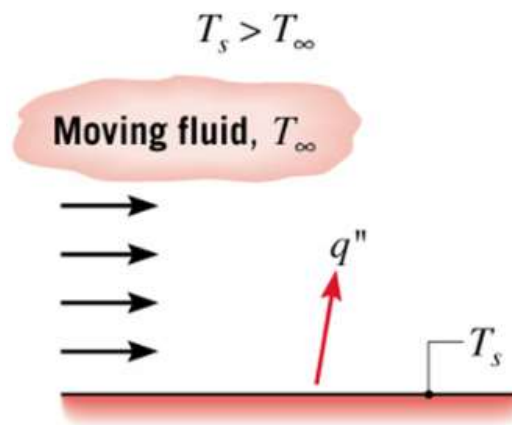
Figure 2.11 - Convection heat transfer [25]

3. Materials and Methods

3.1. HPT Blade and Rectangular Blocks

As mentioned in **Chapter 2**, the aircraft that operates the PDL-FNC flight route is a Turboprop Bombardier DHC8-400, seen in **Figure 3.1 a)**. It is equipped with the PW150A engine from the manufacturer Pratt & Whitney, in which the turbine blade studied in this work operates.

HPT blades are the components most susceptible to damage and failure [2] and its study is crucial in order to understand how it deforms throughout a flight, when it is under rigorous conditions, and also to predict the extent of its deformation by the end of its lifetime. For this effect, it was necessary to build a blade model using the finite element method in order to run simulations that would provide results that could be analyzed. To build this model, an HPT blade was requested and supplied by the regional airline company. The HPT blade and its dimensions can be seen in **Figure 3.1 b)**.

a)   b)
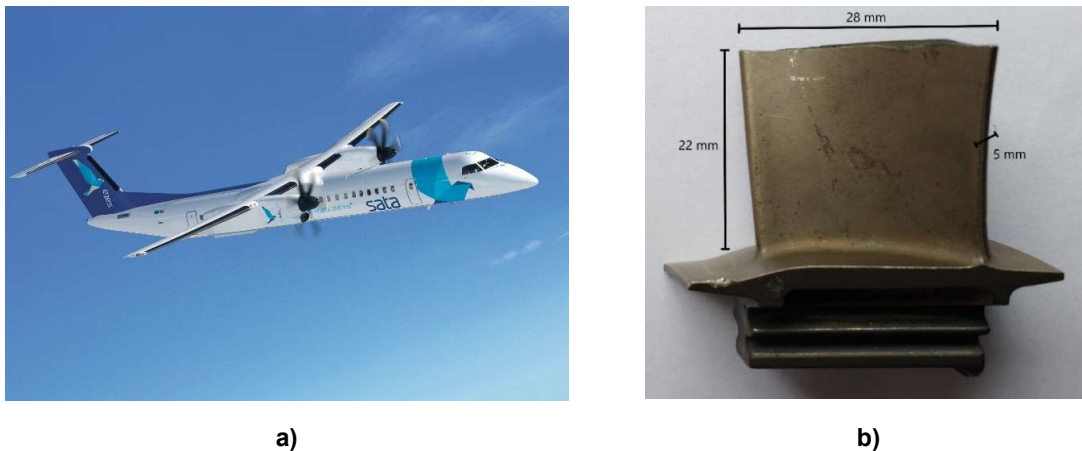
Figure 3.1 - a) Bombardier DHC8-400 [31]**; b) Discarded turbine blade dimensions**

With the ultimate intention of building and studying the blade model, a rectangular block model was created with the dimensions of the HPT blade in order to test the simulations that would later on be applied on the blade model. This rectangular block would validate the finite element model built using the ABAQUS finite element software (version 6.13-4), which would ultimately be used to study the blade model. The rectangular block built on ABAQUS can be seen in **Figure 3.2 a)**. Given that the rectangular block is symmetrical in two axis, a decision was made to study one quarter of the rectangular block in order to have a more refined finite element mesh, and therefore more precise results, and also to save computing time. This symmetrical rectangular block and its dimensions can be seen in **Figure 3.2 b).**
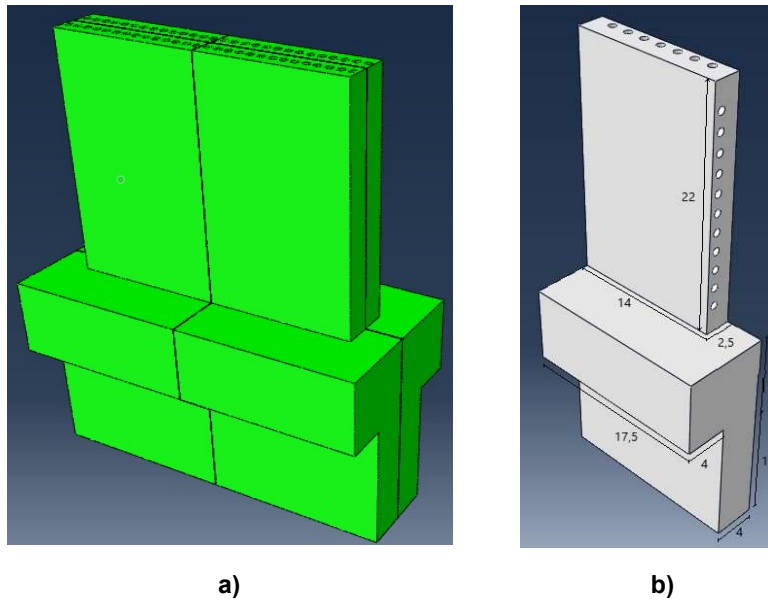
Figure 3.2 - a) Rectangular block; b) Symmetrical rectangular block with dimensions

Given that the main objective of this work is to study the effect of the cooling mechanisms on the temperatures and deformation of the HPT blade, it was of interest to design several symmetrical block geometries with different numbers, sizes, orientations and locations of cooling channels, with the goal of studying the effect of the cooling flow that passes through the cooling channels on the temperatures and deformation of the several blocks. These geometries were designed to have the same volume and can be seen in **Figures 3.3** and **3.4**. The descriptions of the different geometries and cooling channels can be seen in **Table 3.1** and all the results obtained from the analyses of these geometries can be consulted in **Chapter 4**.
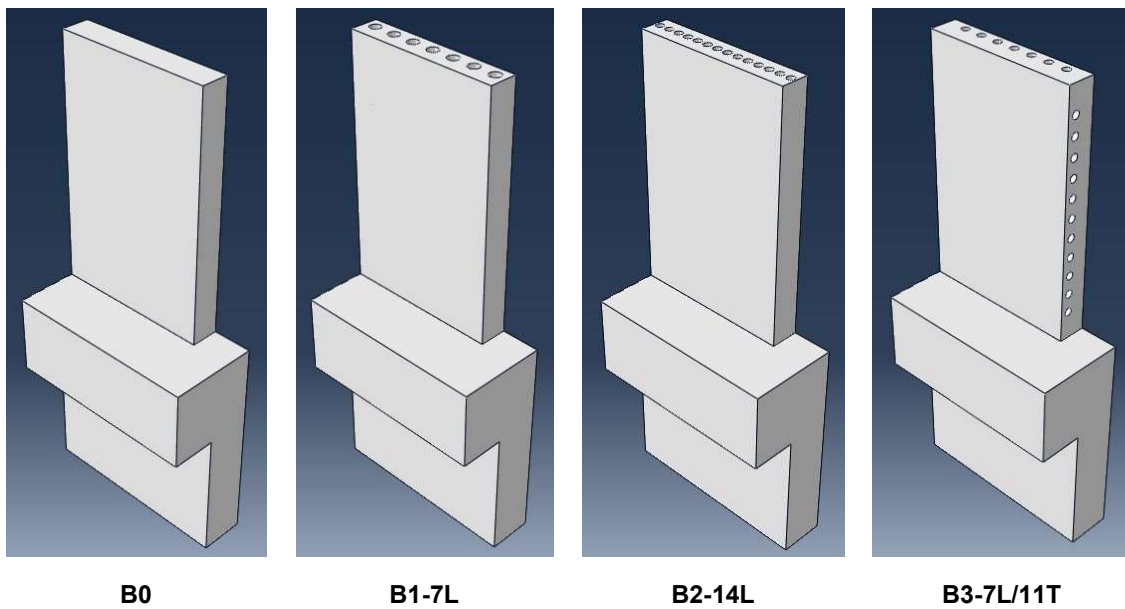
Figure 3.3 - Symmetrical rectangular block geometries (B0-B3)
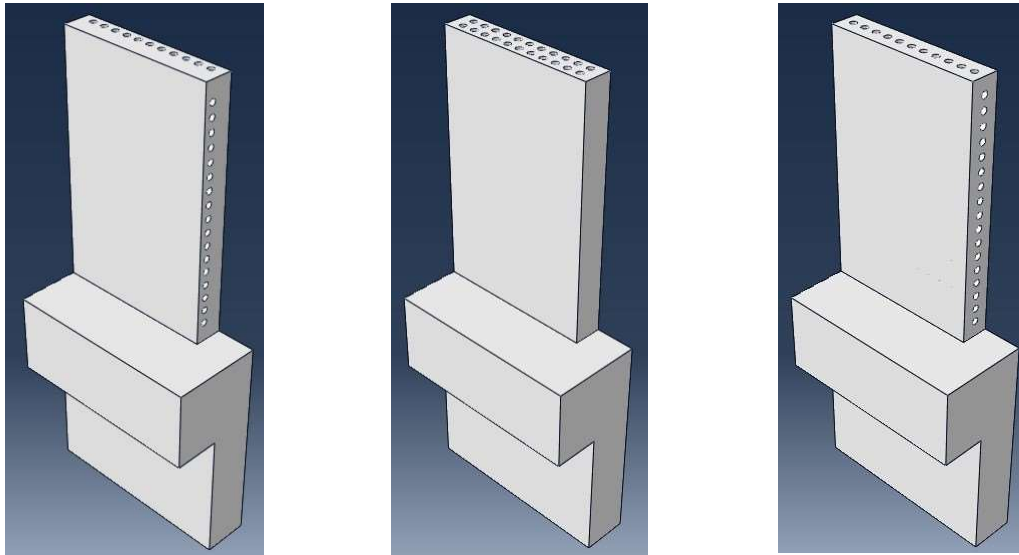
B4-11L/17T   **B5-11L/11L**   **B6-11L/17T-Net**

Figure 3.4 - Symmetrical rectangular block geometries (B4-B6)

Table 3.1 - Description of the symmetrical rectangular block geometries

B0	No cooling channels
B1-7L	7 longitudinal cooling channels
B2-14L	14 longitudinal cooling channels
B3-7L/11T	7 longitudinal / 11 transversal cooling channels
B4-11L/17T	11 longitudinal / 17 transversal cooling channels
B5-11L/11L	11 longitudinal / 11 longitudinal cooling channels
B6-11L/17T-Net	11 longitudinal / 17 transversal cooling channels in a net-like disposition

After the study of the several rectangular block geometries, and the validation of the finite element model built, the study of the blade model was to follow. To do so, it was necessary to obtain a CAD drawing of a turbine blade model. It was initially considered to perform a scan on the blade acquired from the regional airline company and, from there, build a blade model with cooling channels to be analyzed by the validated finite element model. However, due to external circumstances, it was not possible to scan the blade and obtain the CAD drawing in this fashion. To circumvent this, a CAD drawing of a similar HPT blade was searched and found online in the GrabCAD site [32], a site where a library of CAD drawings are uploaded and shared by a community. This particular blade CAD drawing was uploaded by the user Axel.

The turbine blade CAD drawing found online is a component of the SNECMA M88 turbofan engine which equips the French Dassault Rafale fighter [33]. This blade, obtained in the CATIA CAD format, was, in its initial dimensions, approximately seven times larger than the blade from the PW150A engine. However, proportionately, it was very similar, and so, after the application of a

reductive factor using the CAD software SOLIDWORKS 2019, the blade CAD drawing was obtained. This drawing and its dimensions can be seen in **Figure 3.5**.
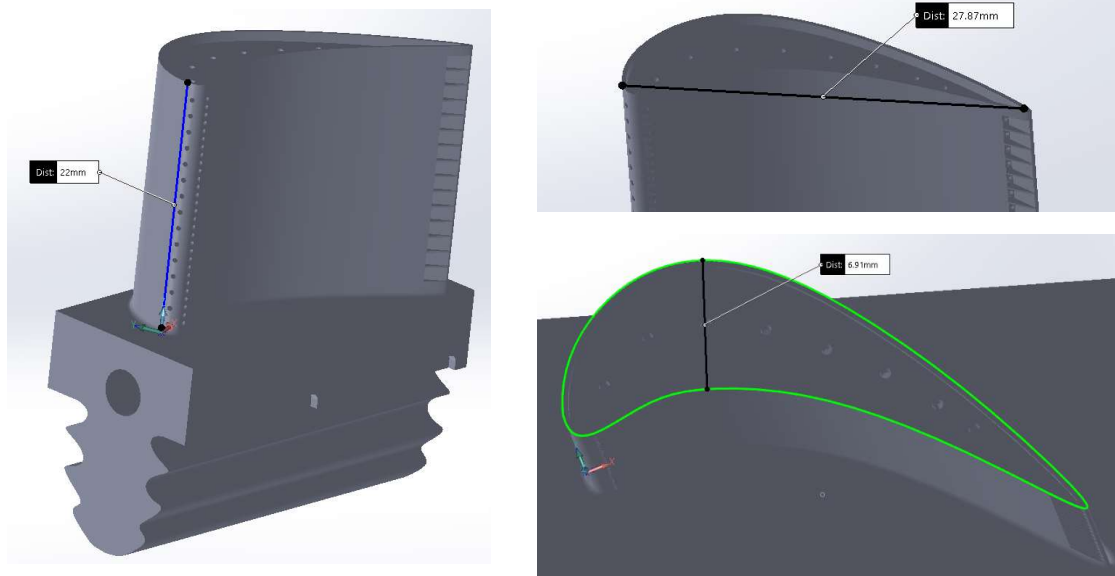
Figure 3.5 - Turbine blade dimensions

From the observation of the adapted blade CAD drawing, and comparing to the dimensions of the HPT blade obtained from the airline company, it is clear that the dimensions are very close with only the width of the blade being larger than the width of the discarded blade. Given that the differences between both blades are not significant, this drawing was considered a good replacement and was used as the base of the blade model to be analyzed by the ABAQUS software.

3.2. Material Properties

With the CAD drawings for both the rectangular blocks and the HPT blade obtained and, in order to continue building the finite element model, the next step would be to choose the material of the blade – knowing that modern turbine blades often use nickel-based superalloys [34]. Given that the blade manufacturer does not supply information regarding the material of the blade, it was necessary to find a suitable replacement.

As explained in the **Introduction**, this work gives sequence to a previous thesis. In it, the turbine blade acquired was, through reverse engineering, analyzed in order to determine its density and chemical composition, with the finality of choosing a material. In function of this information, several nickel superalloys were compared in order to determine which would be the most suitable. That choice fell on the TMS-75 superalloy, and its thermal and mechanical properties can be seen in **Table 3.2,** as well as its temperature and stress dependent plastic strains in **Table 3.3** [2].

Table 3.2 - Thermal and mechanical properties of the TMS-75 superalloy [2] [35]

Temp. T (ºC)	Thermal Conductivity k (Wm^{-1}K^{-1})	Density ρ (kg m^{-3})	Specific Heat Capacity C_p (J kg^{-1} K^{-1})	Young's Modulus along (001) E (MPa)	Poisson's ratio v (-)	Mean Thermal Expansion Coefficient α (×10^{-6})
20	-	8894	-	-	-	11.7
50	8.909	8880	401	145980	0.392925	11.7
100	9.563	8857	407	144650	0.3918	11.7
150	10.266	8833	412	143710	0.390925	11.7
200	10.928	8810	417	142560	0.3903	11.7
250	11.571	8787	421	140820	0.389925	12.3
300	12.225	8764	425	138800	0.3898	12.9
350	12.899	8741	428	136750	0.389925	13.4
400	13.624	8718	431	134630	0.3903	13.9
450	14.404	8695	435	132720	0.390925	14.4
500	15.240	8672	439	130740	0.3918	14.9
550	16.195	8649	448	128420	0.392925	15.3
600	17.301	8626	465	126610	0.3943	15.7
650	18.543	8603	480	124520	0.395925	16.1
700	19.764	8580	493	122560	0.3978	16.5
750	20.699	8557	502	119990	0.399925	16.8
800	21.293	8534	509	117340	0.4023	17.1
850	21.506	8512	513	114540	0.404925	17.4
900	21.594	8489	517	111340	0.4078	17.7
950	21.820	8466	520	107490	0.410925	17.9
1000	22.111	8444	524	104490	0.4143	18.1
1050	22.374	8421	528	100900	0.417925	18.3

Table 3.3 - Temperature and stress dependent plastic strain for the TMS-75 superalloy [2] [35]

Temperature T ºC (K)	0.2% Proof Stress $\sigma_{0.2}$ (MPa)	Plastic Strain ε_{pl} (-)	UTS σ_{UTS} (MPa)	Plastic Strain ε_{pl} (-)
20 (293)	850	0	898	0.06414988
550 (823)	805	0	863	0.0587315
750 (1023)	972	0	1287	0.06889932
850 (1123)	893	0	1179	0.13220359
950 (1223)	564	0	932	0.19477584
1050 (1323)	513	0	717	0.15491575

To analyze the deformation of the blade, creep analyses were performed using the ABAQUS FEM software. This software requires data in terms of a steady-state creep rate as seen in **Equation 3.1.** As for the steady-state creep constants, they can be consulted in **Table 3.4.**

$$\dot{\varepsilon}_s = K_1 \sigma^n \tag{3.1}$$

Table 3.4 – Steady-state creep constants for the TMS-75 [2]

Temperature T ºC (K)	Temperature dependent material constant K_1 (SI)	Creep Stress Exponent n (-)
900 (1173)	5.575×10^{-23}	1.75
1100 (1373)	9.062×10^{-22}	1.75
1150 (1423)	1.610×10^{-21}	1.75

3.3. Flight-Cycle Conditions

With the block and blade CAD models built and the blade's material chosen, to continue building the FEM model it was now necessary to simulate the in-flight conditions that the HPT blade goes through during the duration of a flight-cycle. This information was obtained from the previous thesis where the analysis of Flight Data Records (FDR) for several flight routes, supplied by the regional airline company, resulted in the plots for the turbine-inlet-temperature (TIT) and the rotation speed (ω_{HPT}), which can be seen, in an approximate fashion as the original FDR records were unavailable, in **Figures 3.6 a)** and **b)**, respectively.

a)   b)
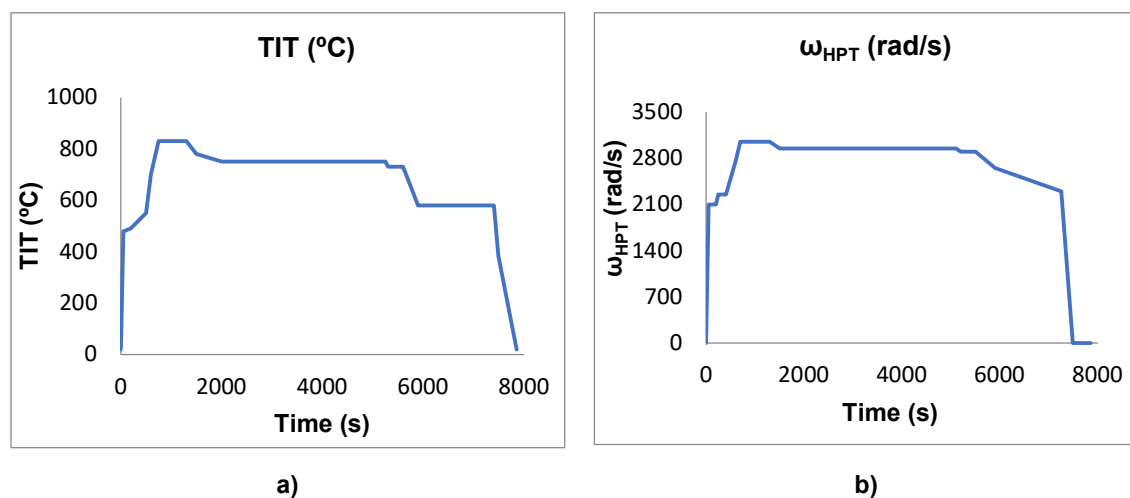
Figure 3.6 - a) Turbine Inlet Temperature (TIT) for a PDL-FNC flight cycle; b) Rotation speed - ω_{HPT} for a PDL-FNC flight cycle [2]

The TIT plot simulates the thermal flight conditions, and the turbine rotation speed plot simulates the mechanical flight conditions imposed on the HPT blade.

To achieve the main objective of this work, it was imperative to acquire information regarding the cooling flow that is bled from the compressor stages [2] [4] [19] and passes through the channels of the blocks/blade . Information like the temperature of the cooling flow and its convection coefficients had to be obtained. As for the temperature of the cooling flow, it was assumed to be the ambient temperature, which, during the flight, is the exterior atmospheric temperature (EAT).

The EAT, which is to say the temperature at the exterior of the airplane, varies during the flight as the airplane gains and loses altitude. To know the evolution of the EAT, it was necessary to first know the evolution of the altitude. However, given that the access to the FDR records was unavailable, it was necessary to make an approximation. Knowing that the DHC8-400 aircraft can fly at a maximum operating altitude of 25000 feet (7600 meters) [36], and that the 973 Km flight route between PDL and FNC is flown in approximately 2 hours (7492 s) [2] - which means an average ground speed of 467 Km/h - several flights were researched that resembled these settings.

A good approximation to the PDL-FNC flight was a London-Amsterdam flight, which, as can be seen in **Figure 3.7 b),** has a travel distance of 450 Km and a maximum altitude of 23000 feet. Knowing that a flight between London-Amsterdam takes approximately one hour, the average ground speed of 450 Km/h was calculated. With these flight settings – ground speed, altitude – being very similar, it was possible to use the London-Amsterdam altitude profile as a reference for the PDL-FNC altitude profile. Of course, being that the PDL-FNC flight is twice the size of the London-Amsterdam flight, the cruise flight phase would naturally be longer. With this in mind, from the comparison between the London-Amsterdam flight altitude profile seen in **Figure 3.7 b),** the typical flight profile seen in **Figure 3.7 a),** and the TIT plot seen in **Figure 3.6 a),** an approximated flight altitude profile for the PDL- FNC flight was obtained and can be seen in **Figure 3.8**.

a)   b)
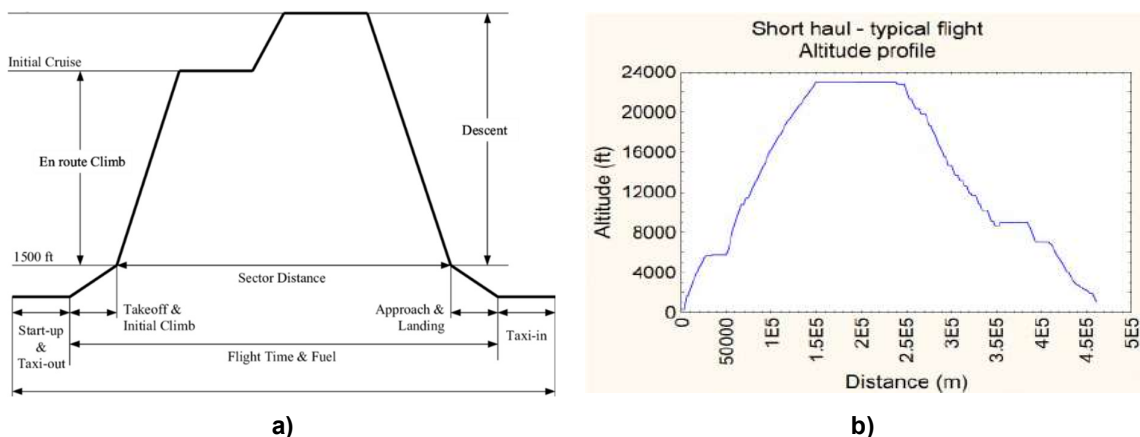
Figure 3.7 - a) Typical flight profile [37]**; b) Flight altitude profile for a London-Amsterdam flight**
[38]
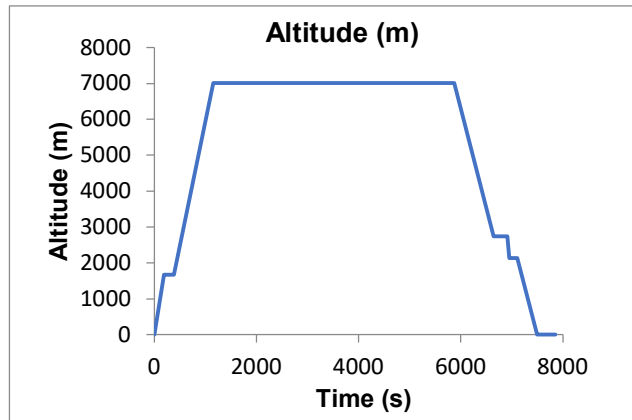
Figure 3.8 - Approximated flight altitude profile for a PDL-FNC flight

With the information regarding the flight altitude profile, it was now possible to obtain the EAT temperatures at the exterior of the airplane. Using a web calculator provided by the website "Aerodynamics for Students" [39], and inserting the altitude values, the temperature values were obtained. It is of importance to note that this calculator uses 15 ºC as the sea level temperature – given that in the Azores islands, where the regional airline company operates, the sea level temperature is considered to be 20 ºC, 5 ºC were added to all the temperature values obtained in the calculations. The final EAT plot for the PDL-FNC flight can be seen in **Figure 3.9.**
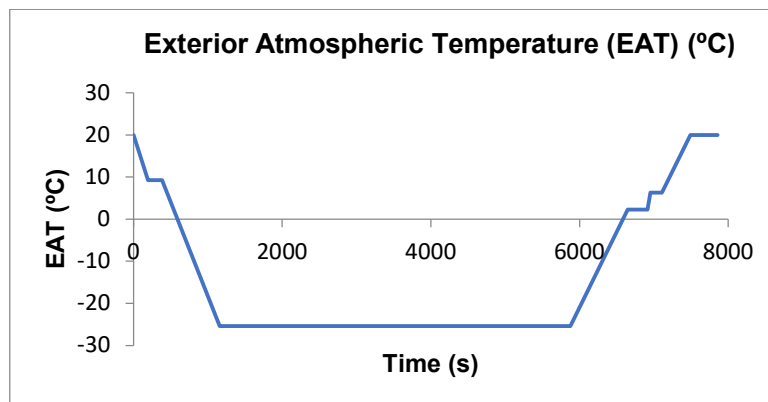
Figure 3.9 - Exterior atmospheric temperature plot of the PDL-FNC flight

3.4. Thermal Loading - Heating and Cooling Mechanisms

Regarding the cooling mechanisms of the model and knowing the EAT temperature, the characterization of the channels' cooling flow was now closer to what was required by the ABAQUS FEM software. This software requires both a "sink temperature" (EAT) and a "film coefficient" (cooling convection coefficient) to define the "surface film condition" (flow) in the Interaction module as can be seen in **Figure 3.10** for both the block and blade model.

| a) | b) |
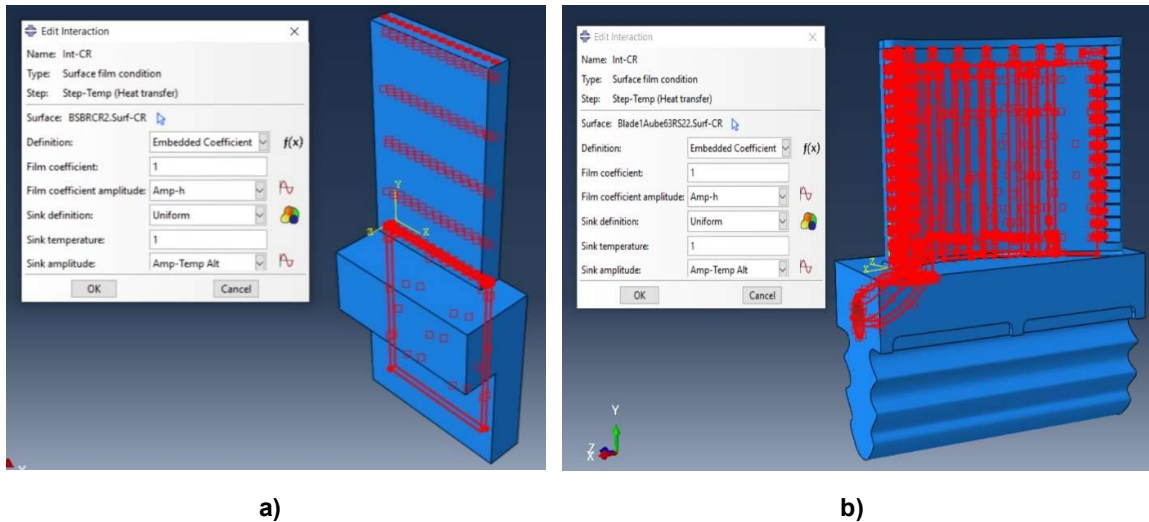
Figure 3.10 - Cooling flow applied on the cooling channels as a surface film condition on the a) rectangular block model; b) blade model

As for the cooling channels' flow convection coefficients, two were considered in this study. The first convection coefficient was assumed to be 500 W/m^{2}K, as the channels' cooling flow can be considered a high pressure gas inside tubes [40]. However, a more appropriate second convection coefficient was obtained from calculations made considering the diameter of the cooling channels [41]. The FEM simulations were run using both convection coefficients and their results were compared in order to assess the influence of the convection coefficient value on the temperature and deformation of both the block and blade models. Both convection coefficients can be consulted in **Table 3.5** and a convection coefficient plot (used for all flow coefficients) for the flight cycle can be seen in **Figure 3.11**.

It is important to note that the convection coefficient plot stabilizes at 10 W/m^{2}K by the end of the 7492 s flight cycle, in order to simulate the engine shutdown and the evolution of the heating flow and cooling flows heat transfer from forced convection to natural convection, as the block/blade starts cooling down naturally. This will be important later on when discussing the results in **Chapter 4**.

Table 3.5 - Thermal analysis cooling channels' flow convection coefficients [40] [41]

Cooling flow convection coefficients, h (W/m^{2}K)	
First convection coefficient	**Second convection coefficient**
500	923
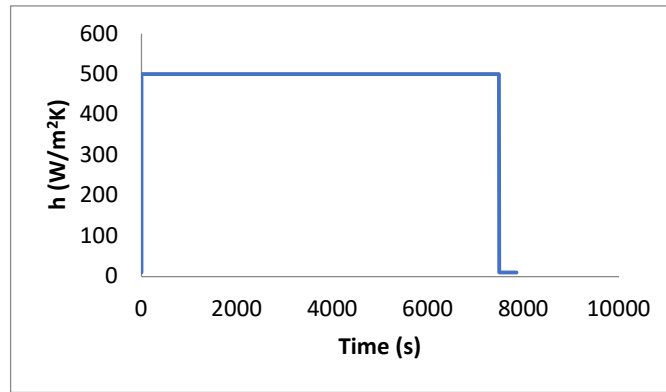
Figure 3.11 - Convection coefficient plot for the PDL-FNC flight cycle

As for the heating mechanisms, two heating approaches were followed. The first one defines the TIT temperature plot as the temperature of the outside walls/surfaces of the blocks/blade during the duration of the flight cycle. In this approach, the temperature is defined as the boundary condition (temperature as boundary condition – TBC). It is the simplest approach as a temperature is applied on the walls and a cooling flow is applied on the cooling channels. The temperature being defined on the walls as a boundary condition can be seen in **Figure 3.12** for both the block and blade model.

a)   b)
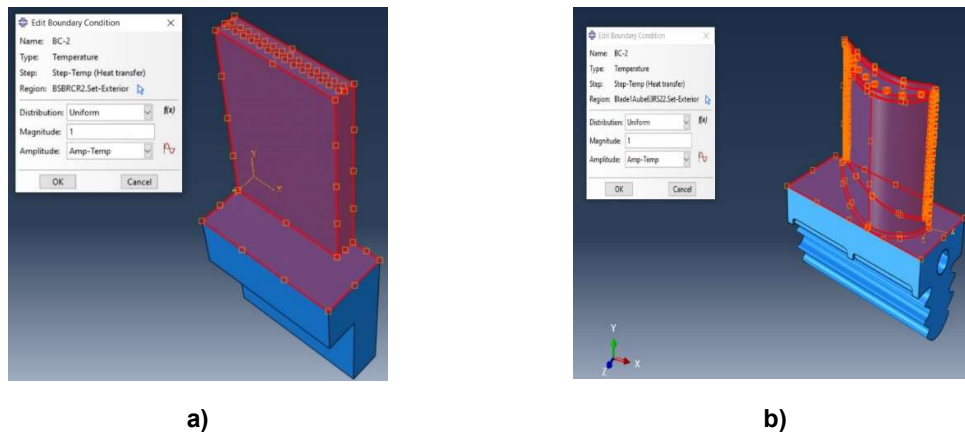
Figure 3.12 - Temperature applied as a boundary condition on the a) block's walls; b) blade's walls (TBC)

The second heating approach defines the TIT temperature plot as the temperature of a heating flow applied on the walls/surfaces of the blocks/blade during the duration of the flight cycle. In this approach, the heating of the block/blade is provided by convection heat transfer, and therefore convection is the boundary condition (CBC).

Also in effect are the cooling channels' flow and a surface film cooling flow that is applied on the outside surfaces. This cooling flow originates from the cooling channels through tip cap cooling holes and film cooling holes and forms a protective surface film that envelops the blade's surfaces and reduces the influence of the heating flow, which is to say, the hot gases from the combustion chamber.

This method of cooling is called film cooling and a schematic on the different heating and cooling flows at play in the interior and exterior of the blade can be seen in **Figure 3.13** [2] [4] [18]**.**
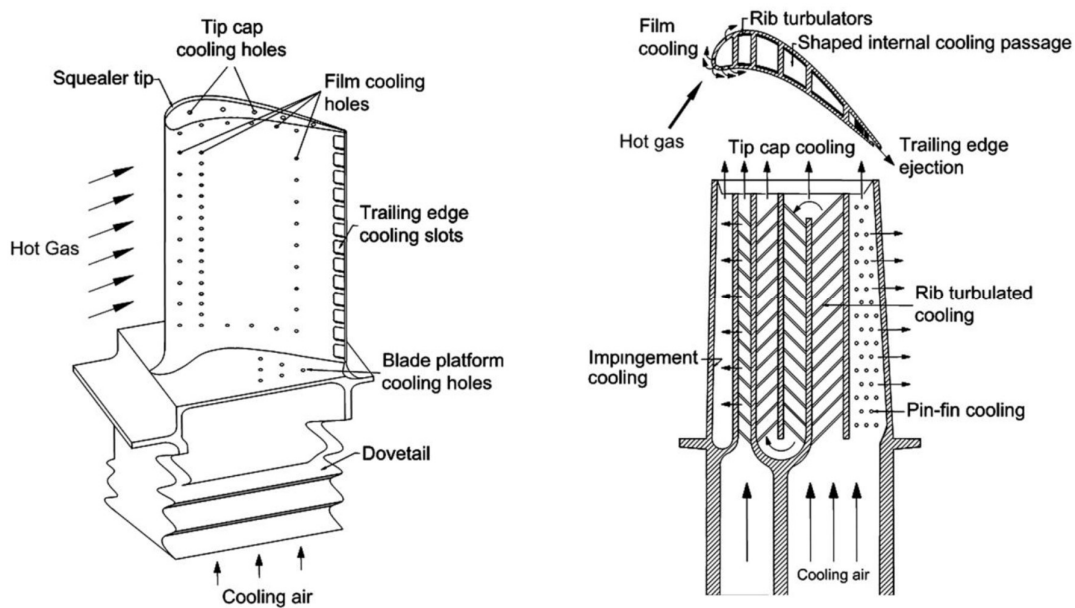
Figure 3.13 - Schematic of a modern gas turbine with common cooling techniques [2] [18]

To simulate both the heating flow and surface film cooling flow, these flows were applied on the outside surfaces of the block and blade models using the ABAQUS Interaction module and applying them as a surface film condition on each surface separately, as can be seen in **Figure 3.14** through **3.16.**
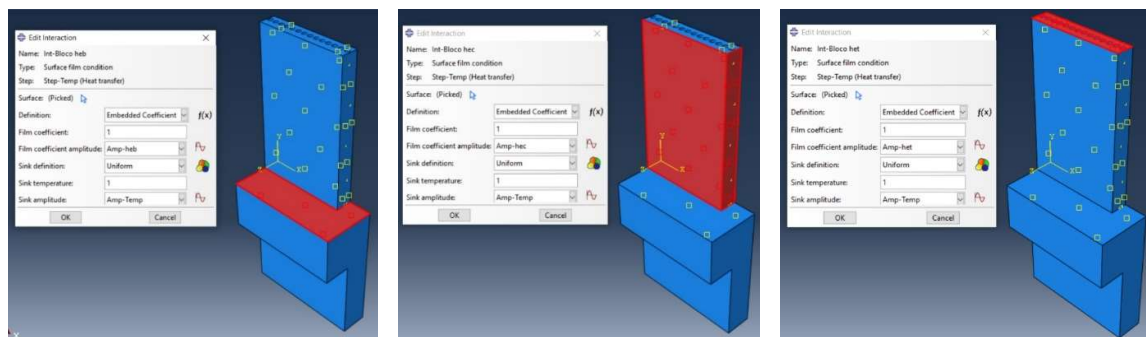
Figure 3.14 - Heating flow applied on the blade's walls (CBC)

a)   **b)**
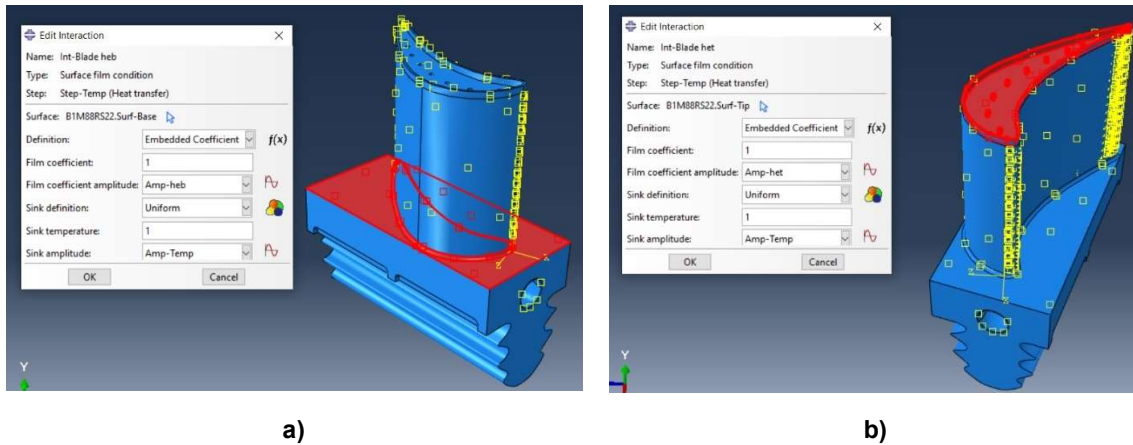
Figure 3.15 - Heating flow applied on the a) blade's platform surface; d) blade's tip (CBC)

a)   **b)**
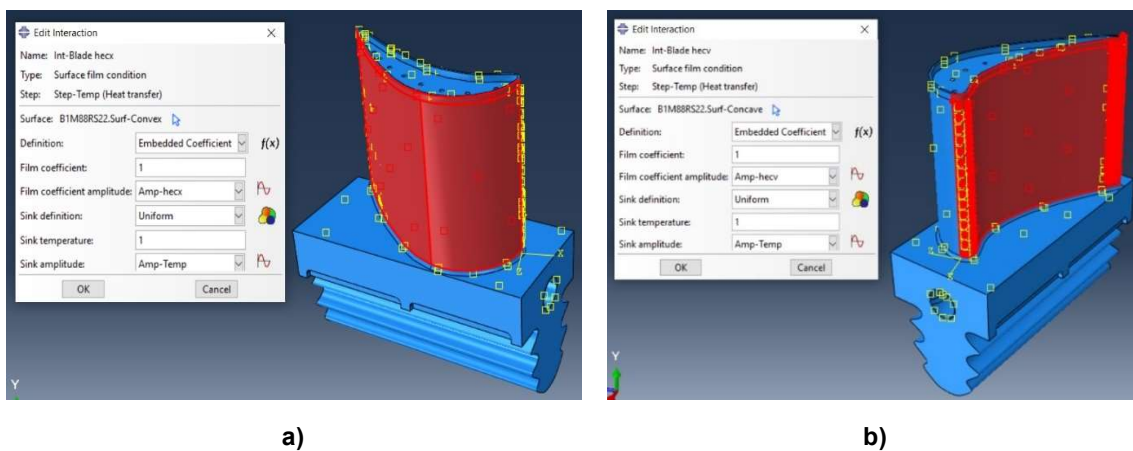
Figure 3.16 - Heating flow applied on the a) blade's convex surface; d) blade's concave surface (CBC)

As for the convection coefficients, in this CBC analysis two sets of heating and cooling flow coefficients were employed to study the temperatures and deformation of the block/blade, and like the TBC analysis, their results were compared in order to verify the effect of the different sets of convection coefficients. When it comes to the heating flow's coefficient, the first set presented a convection coefficient of 500 W/m^{2}K for all surfaces of the block/blade, the same as the cooling channels' flow coefficient. The second set though presented a more realistic approach, as a different convection coefficient was assigned to each surface of the block/blade – naturally the hot gas flow impacts the distinct surfaces of the HPT blade in differing ways, as the hot gas behaves differently, for example, when flowing by the convex surface than when flowing by the blade's platform, due to the geometry of the surfaces. Both sets of convection coefficients of the heating flow for the different block/blade surfaces can be consulted in **Table 3.6**

A note must be made concerning the TBC thermal analysis of the rectangular block model. Because a symmetrical block was used on the analyses, it was not possible to differentiate between the convex and concave surface. When it comes to the second set of convection coefficients, there are different values being applied on the convex and concave surfaces. To address this, an average

was made of the hecx and hecv coefficients, which resulted in a hec coefficient of 1120 W/m²K, to be applied on the surfaces, with the exception of the top of the block and the platform surface, which maintain the coefficient value seen in **Table 3.6.**

Table 3.6 - CBC thermal analysis heating flow convection coefficients [42]

	Heating flow convection coefficients (W/m²K)	
	First set of convection coefficients [he]	**Second set of convection coefficients [hev]**
Blade's Convex surface - Block's equivalent wall	500	1265 [hecx]
Blade's Concave surface - Block's equivalent wall	500	975 [hecv]
Blade - Tip surface - Top of the block	500	840 [het]
Blade - Platform surface - Block's platform surface	500	839 [heb]

As for the cooling flows' convection coefficients, the same values that were previously explained were used for the cooling channels' flow. The surface film cooling flow coefficient though, was assumed to be approximately half of the cooling channels' flow, as information about the surface film cooling flow convection coefficient is scarce. This was assumed due to the fact that when the surface film cooling flow exits the cooling channels, it bears the impact of the heating flow, which could reduce its velocity and convection coefficient.

Both sets of cooling flow convection coefficients can be consulted in **Table 3.7**.

Table 3.7 - CBC thermal analysis cooling flow convection coefficients

Cooling flow convection coefficients (W/m²K)			
First set of convection coefficients		**Second set of convection coefficients**	
Cooling channels' flow [h]	**Surface film flow [hc]**	**Cooling channels' flow [h]**	**Surface film flow [hc]**
500	250	923	450

All the heating and cooling flows applied on the models followed the same convection coefficient plot for the flight cycle seen in **Figure 3.11**, with the only difference being its maximum value.

With the different heating approaches defined, and all temperatures and convection coefficients sets identified, both the TBC and CBC thermal analyses could be run on the block and blade model.

3.5. Mechanical Loading and Model Mesh

With the thermal loading defined, the next step would be to apply the mechanical loading on the block and blade model. After the application of the boundary conditions on the base of the block/blade – symmetry in the XX axis and symmetry and pinned in the ZZ axis – the rotation speed load (**Figure 3.6 b)**) was applied as a rotational body force around an axis of rotation using the ABAQUS Load module, as can be seen in **Figure 3.17**.

a)   b)
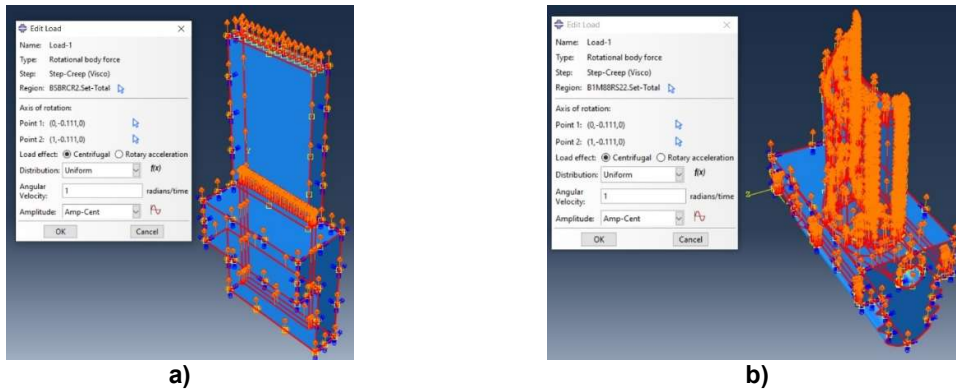
Figure 3.17 - Centrifugal load applied on the a) block model; b) blade model

With the mechanical loading defined, the final step in the construction of the FEM model would be to build a finite element mesh for both thermal and creep analyses to be simulated by ABAQUS. For the thermal analysis, a Standard Heat Transfer DC3D10 element was used - a 10-node quadratic heat transfer tetrahedron. As for the creep analysis, a Standard 3D Stress C3D10 element was used – a 10-node quadratic tetrahedron. After performing a mesh convergence study on both the block and blade model that can be consulted in **Appendix A**, a seed size element of 1 mm for both models was chosen as it presented very small errors between the displacement values. The mesh for both models can be seen in **Figure 3.18**.

a)   b)
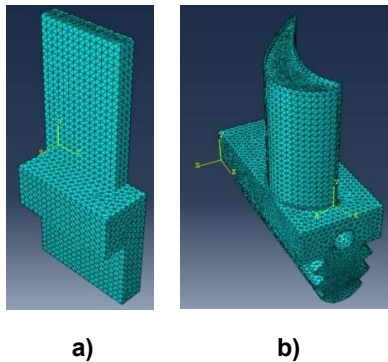
Figure 3.18 - a) Rectangular block mesh; b) Blade mesh

The definition of the mesh concluded the construction of both the block and blade models. With these models built, simulations were run and results were extracted. These results and their study can be consulted in **Chapter 4.**

4. Results and Discussion

4.1. Rectangular Block

As previously explained in **Chapter 3**, before conducting the computational analyses on the blade model, these were initially performed and validated on several rectangular block models with different numbers, sizes and orientations of cooling channels.

The computational analysis is performed in two parts: the first part is a thermal analysis, in which the temperature distribution on the block/blade is calculated; the second part is a creep analysis, where the temperature distribution results/output obtained in the previous analysis are inserted as a Predefined Field using the ABAQUS Load module, and results for stresses, strains and displacements are obtained.

In order to properly evaluate the numerical results and compare them between different block geometries, six points were chosen for which results were calculated. Points 1-4 were chosen due to their location at the top of the symmetrical block, where the displacements relevant to this study take place. Points 5T and 6T are thermal points, where temperatures were gauged to determine the temperature performance of the block cooling. These points and their coordinates can be viewed in **Figure 4.1** and **Table 4.1.**
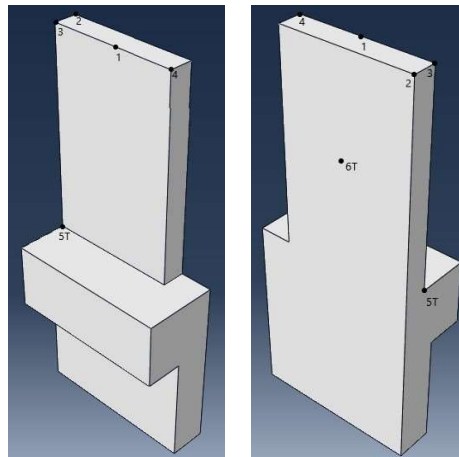
Figure 4.1 - Points selected for the symmetrical block

Table 4.1 - Point coordinates for the symmetrical block

	Point Coordinates (mm)		
Points	**x**	**y**	**z**
1	7	22	2.5
2	0	22	0
3	0	22	2.5
4	14	22	2.5
5T	0	0	2.5
6T	7	11	0

4.1.1. Thermal Analysis Results – Temperature as Boundary Condition (TBC)

In **Chapter 3**, two distinct thermal analyses approaches were introduced: the temperature as boundary condition (TBC) thermal analysis and the convection as boundary condition thermal analysis (CBC). The TBC analysis consists in applying the turbine inlet temperature (TIT) values obtained by the flight data records (FDR) directly on the block's walls, as a boundary condition. Therefore, throughout the analysis, the wall temperature mirrors the evolution of the TIT for the duration of the flight.

The cooling of the block is achieved by means of an air flow that is bled from the compressor stages [2] [4] [19] and is directed through the cooling channels of the block/blade. This flow's cooling power is characterized by its convection coefficient, h, and its temperature, which can be assumed as being the exterior atmospheric temperature (EAT).

As presented before, several block geometries with different numbers, sizes and orientations of cooling channels were used in order to study its effects on the cooling of the blocks. Also, a study on the influence of several convection coefficients was conducted (in this case, on a baseless block) and it can be consulted in **Appendix B**.

To study the temperature distribution on the several rectangular blocks, a time instant of approximately 3000 s was chosen, due to it belonging to the aircraft's cruise flight phase, the longest period of time during the flight in which the TIT remains a constant, as can be seen in the TIT plot (**Figure 3.6 a)**) in **Chapter 3**.

After implementing a convection coefficient of h = 500 W/m^{2}K on this thermal analysis, results for the B2-14L geometry (14 longitudinal cooling channels) were obtained and can be viewed in **Figure 4.2**.

From its observation one can easily see that a cooling effect is taking place. The block's walls and base top are at 750ºC, the TIT for the chosen instant of time. The bottom of the base presents the part's lowest temperatures, which is expected considering that it's farthest away from the walls and base top, while at the same time benefiting from the cooling flow. As for the block itself, by observation of **Figure 4.2**, its interior's temperature has decreased in comparison to the wall's temperature, again proving that the cooling channels and cooling flow are having the desired effect on the block's temperature distribution.
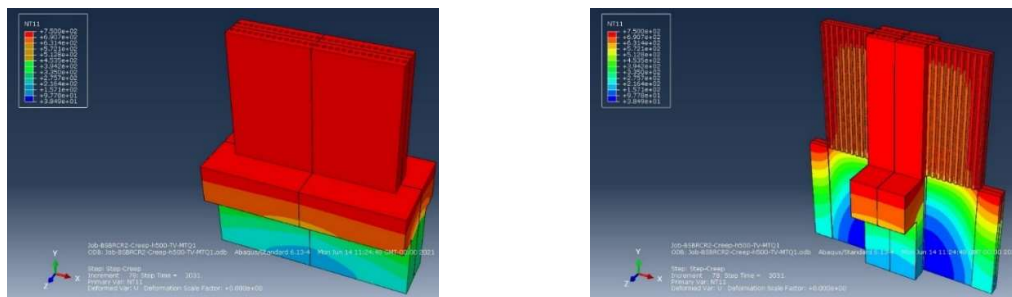
Figure 4.2 - Temperature distribution for the B2-14L rectangular block geometry – Temperature as boundary condition (TBC)

As for the temperature distributions of the remaining rectangular block geometries, these can be viewed in **Figures 4.3** through **4.7**, in a symmetrical presentation.
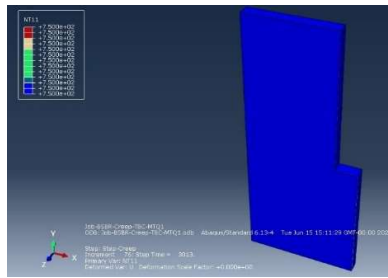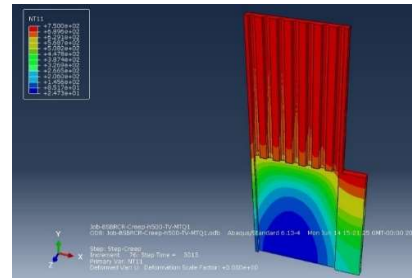
a)   b)

Figure 4.3 - Temperature distribution for the a) B0 geometry; b) B1-7L geometry (TBC)

Figure 4.4 - Temperature distribution for the B2-14L geometry (TBC)
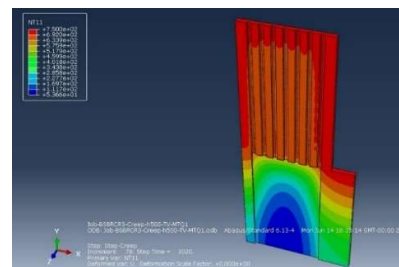
a)   b)

Figure 4.5 - Temperature distribution for the B3-7L/11T geometry: a) cut detail of the transversal cooling channels ; b) cut detail of the longitudinal cooling channels (TBC)
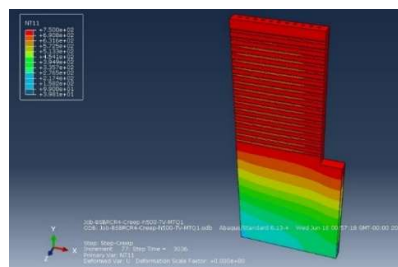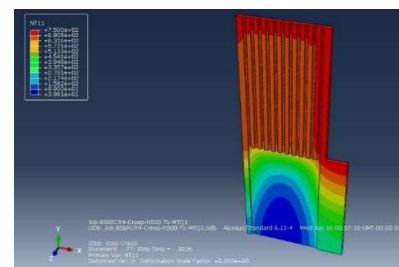
a)   b)

Figure 4.6 - Temperature distribution for the B4-11L/17T geometry: a) cut detail of the transversal cooling channels; b) cut detail of the longitudinal cooling channels (TBC)
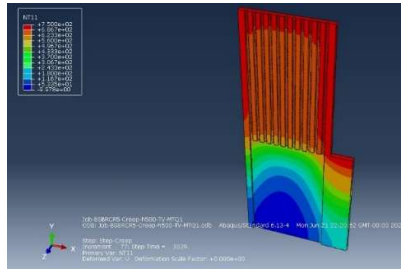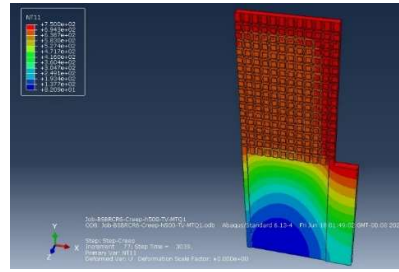
| a) | b) |

Figure 4.7 - Temperature distribution for the a) B5-11L/11L geometry; b) B6-11L/17T-Net geometry (TBC)

By observing the **Figures 4.3** through **4.7**, it can be assessed that, graphically, there are slight variations of the temperature distributions between the different block geometries. However, through the collection of the temperature values on point 6T, these temperature variations are made clearer, as can be seen in **Table 4.2.**

Table 4.2 - Temperature results for the rectangular block geometries (TBC)

Rectangular Block Geometry	Number of Elements	Number of Nodes	Cooling Channels' Surface Area (m²)	h (W/m²K)	Time (s)	Temperature (ºC)	
						Wall Temperature	Point 6T
B0	19877	30666	0	0	3013	750	750
B1-7L	40539	65223	4.836E-04	500	3013	750	692.5
B2-14L	71852	118343	6.770E-04	500	3031	750	673.8
B3-7L/11T	124029	188180	6.770E-04	500	3020	750	669.1
B4-11L/17T	240494	359590	8.440E-04	500	3036	750	656.9
B5-11L/11L	229976	345951	8.511E-04	500	3039	750	657.3
B6-11L/17T-Net	106896	174221	7.985E-04	500	3039	750	674.1

Starting with the geometry B0 with no cooling channels, at the selected time instant the block has achieved thermal equilibrium and is therefore at a constant temperature of 750 ºC, due to the aforementioned lack of a cooling flow.

As for the block geometries with cooling channels, there is a decrease in temperature when there's a corresponding increase of the number of cooling channels, with the exception of the B6-11L/17T-Net geometry which has a net-like disposition of cooling channels. This exception may be due to the fact that, even though the number of cooling channels are the same as the B4-11L/17T

geometry, these channels are positioned in a net-like shape in the center of the symmetrical block, whereas on the B4-11L/17T geometry, the cooling channels are more evenly distributed throughout the block and therefore assure a more efficient distribution of the cooling flow.

Considering the cooling channels distribution, the geometries that contain a mixture of separated longitudinal and transversal channels present lower temperature results for point 6T when compared to geometries with solely longitudinal channels. For example, when comparing B3-7L/11T with B2-14L, the former delivers lower temperatures as opposed to the latter, even though both geometries have exactly the same cooling channels' surface area. Of course, B2-14L only has one line of 14 cooling channels while B3-7L/11T has more cooling channels distributed in two lines in different orientations, therefore ensuring a more consistent cooling flow distribution.

With the increase of the cooling channels' surface area, there is consequentially a larger interaction between the cooling flow and the blocks, and the results in most cases indicate that there is a decrease of temperature with the increase of the cooling channels' surface area. However, taking into account the comparison between B4-11L/17T and B5-11L/11L, one can observe that despite the larger cooling channels' surface area B5-11L/11L has over B4-11L/17T, that does not translate into a lower temperature. In this example, the distribution of the cooling channels seems to take precedence over their surface area. This leads back to the previous conclusion that block geometries that contain a mixture of longitudinal and transversal channels (like B4-11L/17T) yield lower temperature results, because they're more efficient in distributing the cooling flow when compared to geometries with solely longitudinal channels.

To conclude this thermal analysis in which the temperature is the boundary condition, an analysis of the B2-14L geometry was made using a cooling flow with a convection coefficient of h=923 W/m²K. These results and their comparison to previous results can be viewed in **Figure 4.8** and **Table 4.3**.

a)   b)
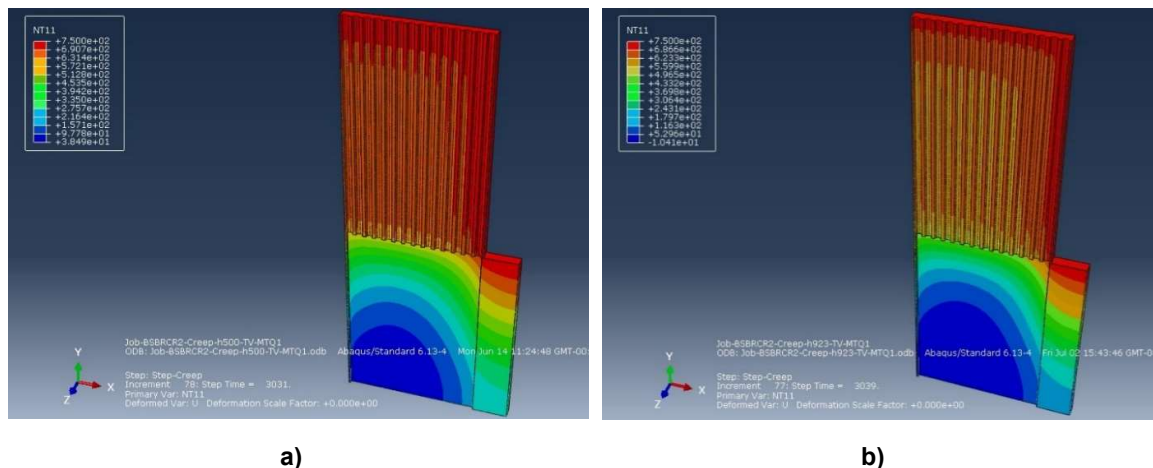
Figure 4.8 - Temperature distribution for the B2-14L geometry when a) h=500 W/m²K; b) h=923 W/m²K (TBC)

Table 4.3 - Temperature results for the B2-14L geometry for h=500 W/m2K and h=923 W/m2K (TBC)

Rectangular Block Geometry	Number of Elements	Number of Nodes	Cooling Channels' Surface Area (m²)	h (W/m²K)	Time (s)	Temperature (ºC)	
						Wall Temperature	Point 6T
B2-14L	71852	118343	6.770E-04	500	3031	750	673.8
B2-14L	71852	118343	6.770E-04	923	3039	750	614.8

The temperature results of point 6T are clear in pointing out that a significant increase in the convection coefficient also led to a decrease in temperature. This was to be expected when taking into account the conclusions drawn in the convection coefficient study that can be found in **Appendix B,** which confirmed that with an increase of the convection coefficient comes a decrease of temperature, due to an improved cooling performance of the cooling channel's flow.

4.1.2. Thermal Analysis Results – Convection as Boundary Condition (CBC)

As stated in **Subchapter 4.1.1.**, two distinct thermal analyses approaches were introduced in **Chapter 3**. The second thermal analysis, addressed in this section, consists on providing heating to the part, whether block or blade, by means of a heating fluid flow, in this case the hot gases that originate from the engine's combustion chamber.

This heating air flow is characterized by a convection coefficient, he, and a temperature Te, in this case the turbine inlet temperature (TIT) affected by a multiplying factor. The inclusion of this multiplying factor was a necessity when taking into consideration that equating the TIT data to the heating flow temperature (Te), resulted in significantly lower block temperature values when compared to the TIT values. Therefore, a multiplying factor was employed in order to raise the temperature values of the heating flow, and by consequence, elevate the block's temperature until reaching a close equivalent to TIT.

The heating flow temperature (Te) was achieved through trial and error, by applying an initial multiplying factor to the TIT data (converted from Celsius to Kelvin for this purpose) and then running an analysis in which the heating air flow and cooling air flow are both in effect. After the conclusion of the analysis, a time instant during the cruise flight phase was chosen, in this case t=3000 s, and the temperature of the block at a specific surface point was read and compared to the TIT value, which at 3000 s corresponds to 750 ºC, the same temperature applied to the block's walls in the TBC analysis. To choose this surface point though, it was first necessary to observe the graphic results of the analysis, which can be seen in **Figure 4.9**. After its observation, point 3 was chosen due to its location mid-block and at the top, and mostly because its temperature is in-between the highest temperatures, which are localized at the upper edges of the leading and trailing edge (point 4), and the lowest

temperatures which can be found mid-block and at the bottom by the base (point 5T). Point 3 was then monitored so that it read as approximately 750 ºC. If the temperature obtained was too far off the desired value, then the multiplying factor was adjusted and a new analysis was run, a procedure that was repeated until reaching 750 ºC at the chosen point and time instant.

Finally, the same process was repeated on all block geometries which, due to different cooling efficiencies between them, resulted also in different multiplying factors.

As for the cooling of the block, two different cooling flows were considered in this analysis, as previously seen in **Chapter 3**. The first and main one is the cooling flow that is directed through the cooling channels and is responsible for most of the temperature reduction. This flow is characterized by a convection coefficient, h, and a temperature considered to be the exterior atmospheric temperature (EAT). The second cooling flow implemented on the analysis was a surface film cooling flow. This flow originates from the tip cooling holes and film cooling holes and forms a surface film that envelops the block/blade and offers a degree of protection against the high temperatures of the hot gas. This flow was also considered in the analyses as representing the hot gas heat losses to the surrounding air as well as to the turbine rotation speed. This second cooling flow is characterized by a convection coefficient, hc, and the same temperature of the main cooling flow (EAT). Having all flows' properties inserted into ABAQUS, the analysis was then submitted and the temperature distribution results for the rectangular block B2-14L may be viewed in **Figure 4.9.**
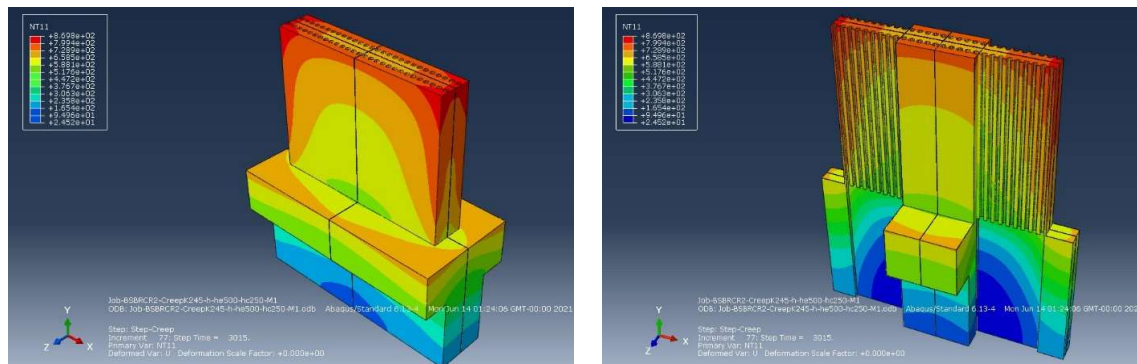
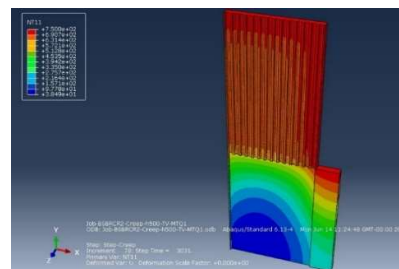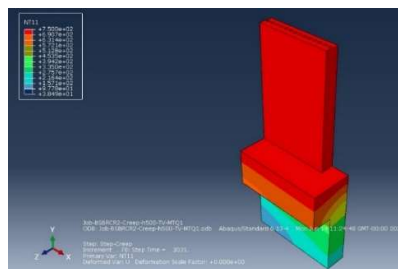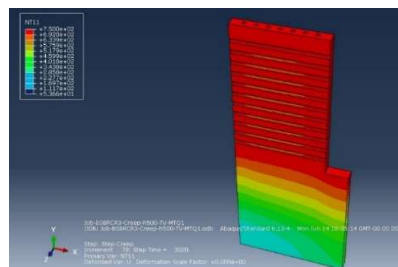**Figure 4.9 - Temperature distribution for the B2-14L geometry – Convection as boundary condition (CBC)**

Through the graphical analysis of **Figure 4.9**, the first noticeable factor is that the temperature distribution of the CBC thermal analysis is quite different than the temperature distribution of the TBC thermal analysis. Whereas in the TBC analysis the entire outside surface is at the same temperature and the cooling effect is noticeable when examining the interior of the block (**Figure 4.2**), in the CBC analysis there is an observable layer-like pattern in the block's temperature distribution.

The highest temperatures are localized at the upper edges of the leading and trailing edge, but very high temperatures can also be observed along the edges of the top of the block, in the transversal direction, and along the edges of the leading edge and trailing edge, in the longitudinal direction. This is consistent with the mode of analysis chosen when it is taken into consideration that in

areas where there is an intersection of two or more surfaces, there is a convergence of surface heating flows which emphasizes the heat transfer from the flow to the block surface.

As for the lowest surface temperatures, they can be found mid-block and at the bottom. This can be explained by the fact that the lower section of the block is being more affected by the cooling flow of the cooling channels than the upper section of the block. This cooling effect is even more noticeable when observing cut details of the block section in the ZZ axis direction, as can be seen if **Figure 4.9**. When advancing into the interior of the block, in the ZZ axis direction, it is possible to perceive that the lower temperature layers are expanding, while at the same time the high temperature layers are receding. This difference between the surface temperatures and internal temperatures demonstrates again that the cooling channels and cooling flow are effectively reducing the block's temperature, a conclusion that is also consistent with the results obtained in the TBC thermal analyses.

The temperature distributions of the remaining rectangular block geometries at the time instant of approximately t=3000 s can be viewed in **Figures 4.10** through **4.16**, in a symmetrical presentation.

a)　　　　　　　　　　　　　　　　　　b)
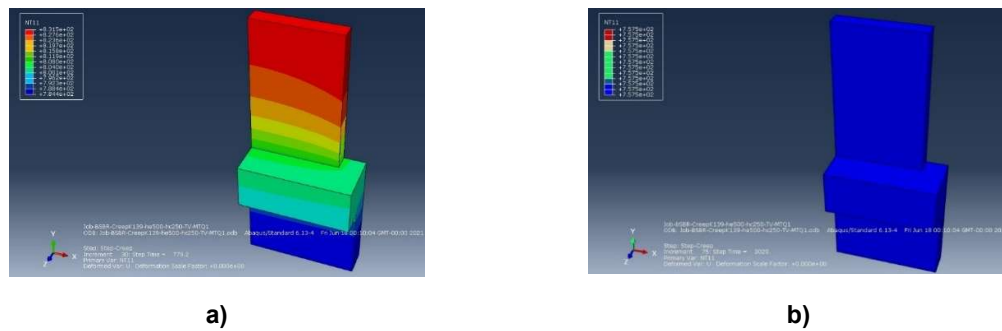
Figure 4.10 - Temperature distribution for the B0 geometry a) before temperature equilibrium; b) after temperature equilibrium (CBC)
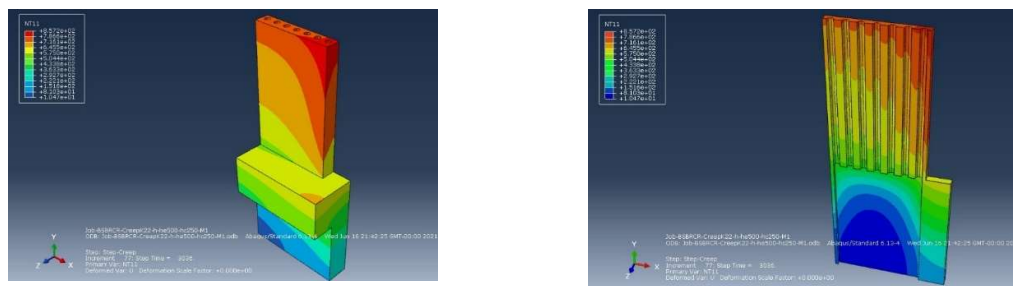
Figure 4.11 - Temperature distribution for the B1-7L geometry (CBC)
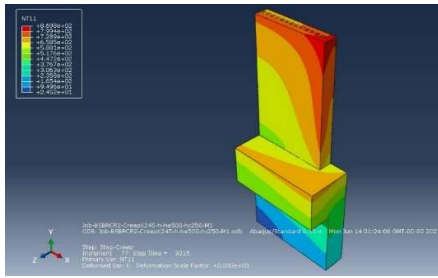
Figure 4.12 - Temperature distribution for the B2-14L geometry (CBC)
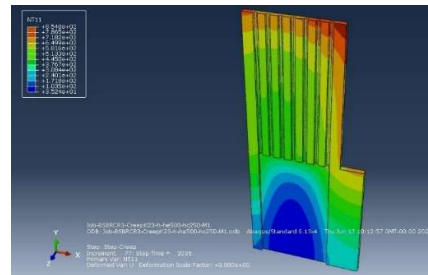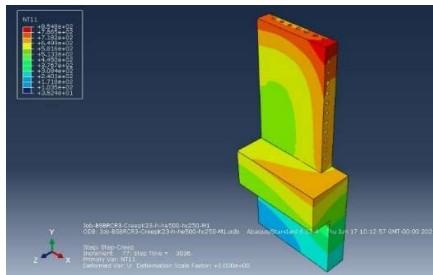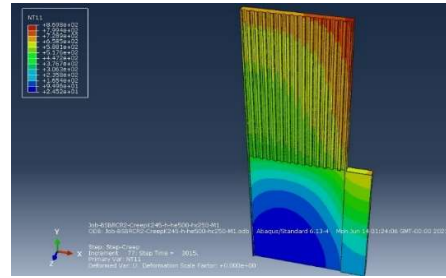
Figure 4.13 - Temperature distribution for the B3-7L/11T geometry (CBC)
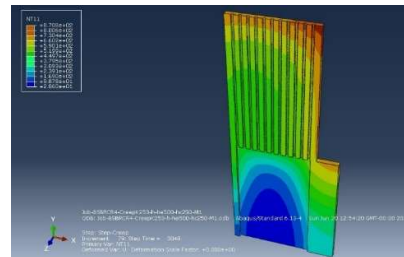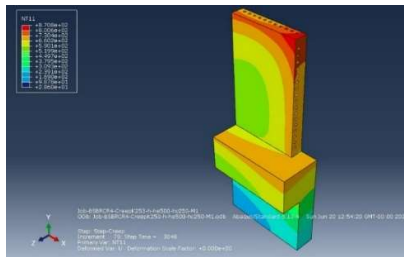
Figure 4.14 - Temperature distribution for the B4-11L/17T geometry (CBC)
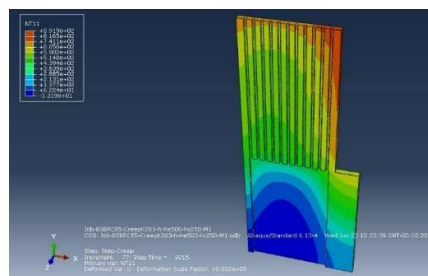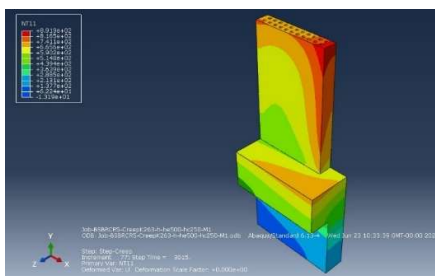
Figure 4.15 - Temperature distribution for the B5-11L/11L geometry (CBC)
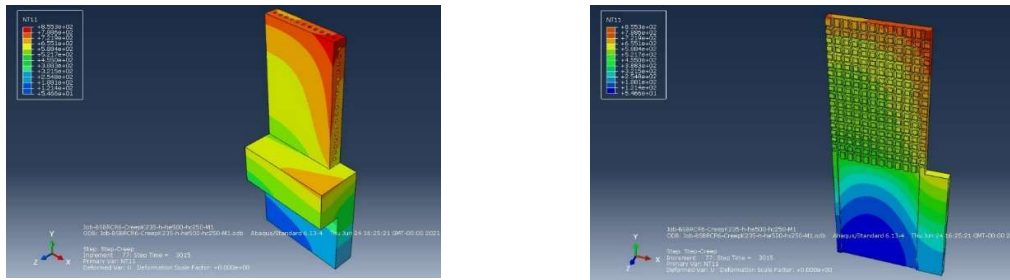
Figure 4.16 - Temperature distribution for the B6-11L/17T-Net geometry (CBC)

Analyzing the temperature distributions of the rectangular block geometries (**Figures 4.10** through **4.16**) it is possible to notice that all temperature distributions follow similar layer-like behaviors. However, by close observation, it is clear that the different cooling channels are producing its effect. This effect is particularly noticeable in the size of the different temperature layers.

By comparison of the block geometries with solely longitudinal channels, B1-7L, B2-14L and B5-11L/11L, it is possible to conclude that as the cooling channels increased in numbers, the block's refrigeration improved, as translated by the size increase of the layers corresponding to the lower temperatures and, consequently, the resulting decrease of the layers' size corresponding to the higher temperatures.

Another comparison to make is the one between the geometries with solely longitudinal channels and those with both longitudinal and transversal channels. For example, when comparing B2-14L with B3-7L/11T, the most relevant aspect observed is that the latter presents lower temperature values on both the leading and trailing edge when compared to the former. In the case of block geometries with longitudinal and transversal channels like B3-7L/11T and B4-11L/17T, the higher temperatures are mostly confined to the top section of the block, as opposed to the geometries B1-7L, B2-14L and B5-11L/11L, where the higher temperatures distribution reaches closer to the base. This difference in temperature distribution behavior is clearly the effect of the transversal cooling channels. These channels go all the way through from the leading edge to the trailing edge, proceeding to transversally cool the block, as well as the edges themselves, hence why geometries that possess transversal channels exhibit lower temperatures on the leading and trailing edge.

To a lesser extent, this effect can also be seen on the geometry B6-11L/17T-Net. However, as seen and explained before, this geometry's cooling channels are positioned in a net-like shape in the center of the symmetrical block and are not as evenly distributed throughout the block as in the cases of the B3-7L/11T and the B4-11L/17T geometries. This centered positioning of the cooling channels ensures a more localized cooling effect, and thus reduces the extension of the distribution of the cooling flow, which in turn leads to less global cooling and higher temperature values.

Having made these comparisons, it is possible to conclude that, just like in the TBC thermal analysis case, geometries with both longitudinal and transversal cooling channels (B3-7L/11T and B4-11L/17T) are, in general, the more effective geometries at lowering the block's temperature.

After observing the graphical results of the CBC thermal analyses, it is also possible to observe their numerical results as can be seen in **Table 4.4**. Numerically, the comparison of point

temperature results between different geometries in the CBC thermal analysis case isn't as direct as when doing the same comparison in the TBC thermal analysis case. In the TBC thermal analysis, to evaluate the cooling efficiency of a geometry, it was merely necessary to register the difference between the wall temperature and an inner point temperature (point 6T). In the CBC thermal analysis, because every geometry has a different heating flow applied to it, with different temperatures due to the effect of a different multiplying factor, it is not as simple as to compare temperature values like in the TBC thermal analysis case, as these temperatures fluctuate significantly between geometries. However, it is possible to calculate the difference between the temperatures of point 1 (high temperature point) and point 5T (low temperature point) for all geometries. These temperature gradients are a result of the effect that the combination of both the heating flow and cooling flows are having on the block. Taking this into account, it is possible to assume that a lower temperature gradient, or a smaller difference between high temperatures (point 1) and low temperatures (point 5T), can provide an indication of a closer equilibrium between the heating flow and the cooling flows. With this in mind, the temperature gradient can be used as a comparative tool between geometries in order to evaluate their cooling efficiencies.

Table 4.4 - Temperature results for the rectangular block geometries (CBC)

Rect. Block Geometry	Temp. (K) Multip. Factor	h (W/m²K)	he (W/m²K)	hc (W/m²K)	Temperature (ºC) (t ≈ 3000 s)			Temp. Difference (ºC)
					Point 4 (High Temp. Point)	Point 3 (Approx. 750 ºC)	Point 5T (Low Temp. Point)	Point 4 – Point 5T
B0	1.39	0	500	250	757.5	757.5	757.5	0
B1-7L	2.2	500	500	250	857.2	766.8	544.2	312.9
B2-14L	2.45	500	500	250	869.8	759.9	568.5	301.3
B3-7L/11T	2.3	500	500	250	854.8	760.5	569.5	285.3
B4-11L/17T	2.53	500	500	250	870.7	760.4	582.8	288
B5-11L/11L	2.63	500	500	250	891.9	760.3	530.2	361.7
B6-11L/17T-Net	2.35	500	500	250	855.3	761.2	549.7	305.6

By analyzing and comparing these temperature gradients, it is possible to observe that, despite the small differences between each geometry's temperature gradient, the geometries that present lower temperature gradients are B3-7L/11T and B4-11L/17T, the ones that possess both longitudinal

and transversal cooling channels. This again coincides with all the conclusions that have been drawn so far, that geometries with a combination of longitudinal and transversal cooling channels showcase, in general, an improved cooling efficiency when compared to geometries with solely longitudinal channels, due to a more thorough distribution of the cooling flow across the rectangular block.

To finalize this thermal analysis in which convection is the boundary condition, analyses of the B2-14L and B3-7L/11T geometries were made by using the second set of convection coefficients. This way, for the heating flow, a variable convection coefficient hev, depicted in **Chapter 3** was employed. As for the cooling flows, convection coefficients of h=923 W/m²K and hc=450 W/m²K were used for the cooling channels' flow and for the surface film cooling flow respectively. These results can be viewed in **Figure 4.17** and **Figure 4.18.**
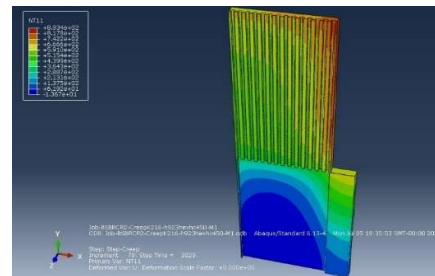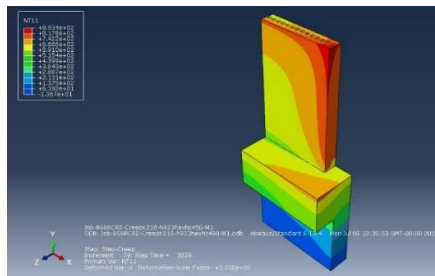
Figure 4.17 - Temperature distribution for the B2-14L geometry for the second set of convection coefficients (CBC)
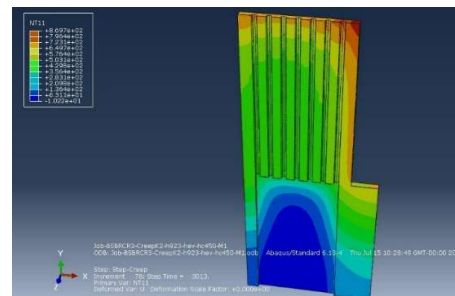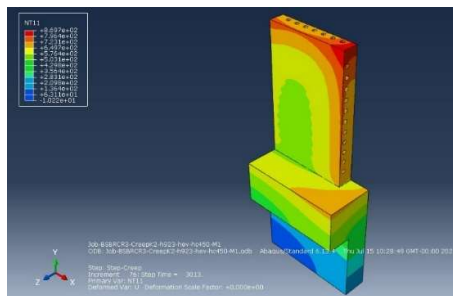
Figure 4.18 - Temperature distribution for the B3-7L/11T geometry for the second set of convection coefficients (CBC)

From these figures it is possible to observe that the graphical results obtained by the CBC thermal analyses with the second set of convection coefficients are quite similar to those obtained by using the first set of convection coefficients.

Like previously seen in the former analyses, it is noticeable that in the B3-7L/11T geometry, the higher temperatures are mostly localized at the top of the block and that both the leading and trailing edge exhibit lower temperatures when compared to the B2-14L geometry. This leads to the same conclusion that the transversal cooling channels are responsible for this difference in cooling effect, due to their cooling flow distribution from leading edge to trailing edge.

Having obtained the thermal analysis results for the B2-14L and B3-7L/11T geometries when using the second set of convection coefficients, it was of interest to compare them to those obtained by using the first set of convection coefficients. A graphical comparison of both these geometries' temperature results can be seen in **Figure 4.19** and **Figure 4.20**.

| a) | b) |
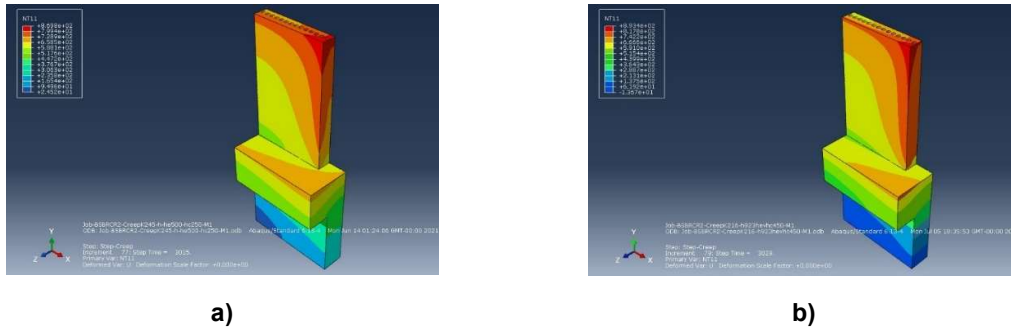
Figure 4.19 - Temperature distribution for the B2-14L geometry when using a) the first set of convection coefficients; b) the second set of convection coefficients (CBC)

| a) | b) |
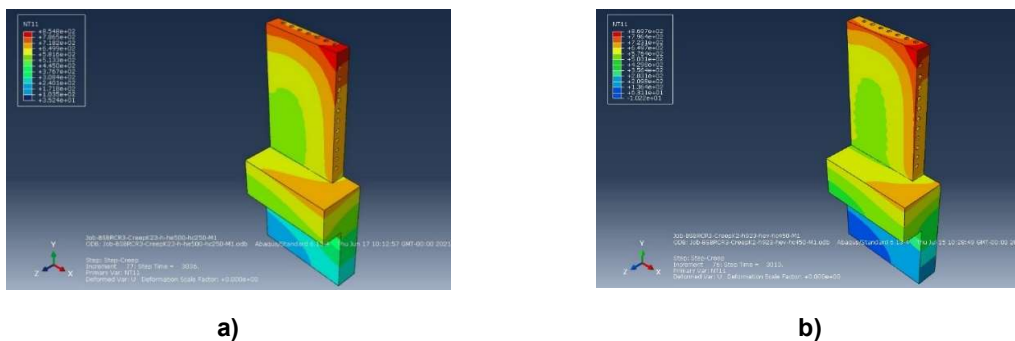
Figure 4.20 - Temperature distribution for the B3-7L/11T geometry when using a) the first set of convection coefficients ; b) the second set of convection coefficients (CBC)

As seen in **Figures 4.19** and **4.20**, the differences between both temperature results are slight. The most relevant differential aspect concerning the temperature distribution in both geometries can be found at the top of the block. Here, both geometries in which the second set of convection coefficients is being used in the analyses, present visibly lower temperatures when compared to the results obtained by the analyses in which were used the first set of convection coefficients. This can be explained in large margin by the cooling channels' flow convection coefficient. This coefficient, from the second set of convection coefficients, is h=923 W/m^{2}K, which is significantly larger than h=500 W/m^{2}K, from the first set. Consequently, this leads to higher heat transfer rates between the block and the cooling flow, which in turn leads to a more effective cooling and temperature reduction at the top of the block.

It's also important to point out that, in this second case, a heating flow convection coefficient of he=840 W/m^{2}K was in effect at the top of the block, which in turn is also quite superior to the convection coefficient used in the first case, he=500 W/m^{2}K. This could, as a possibility, balance out

the cooling efficiency gained with the increase of the cooling channels' convection coefficient in this second case. However, by the results seen above, that is not the case, and it is possible to conclude that the increase of the cooling channels' convection coefficient, from the first case to the second, is more than enough to compensate for the increase of the heating flow's convection coefficient at the top of the block – especially when taking into consideration that the difference between the cooling channels' convection coefficients (from the second case to the first), is larger than the difference between the heating flow convection coefficients.

As for the numerical results, these can be seen in **Table 4.5**.

Table 4.5 - Temperature results for the B2-14L and B3-7L/11T geometries with two sets of convection coefficients (CBC)

Rect. Block Geometry	Temp. (K) Multip. Factor	h (W/m²K)	he (W/m²K)	hc (W/m²K)	Temperature (ºC) (t ≈ 3000 s)			Temp. Difference (ºC)
					Point 4 (High Temp. Point)	Point 3 (Approx. 750 ºC)	Point 5T (Low Temp. Point)	Point 1 – Point 5T
B2-14L	2.45	500	500	250	869.8	759.9	568.5	301.4
B3-7L/11T	2.3	500	500	250	854.8	760.5	569.5	285.3
B2-14L	2.16	923	hev	450	893.4	758.2	553.7	339.7
B3-7L/11T	2	923	hev	450	869.7	756.6	550.2	319.5

Considering the second case in which the second set of convection coefficients were used in the analyses, it is observable that, just like in the first case, the temperature gradient of the B3-7L/11T geometry is lower than the one presented by the B2-14L geometry. Thus, the alteration of the convection coefficients doesn't change the conclusion attained previously – that geometries with both longitudinal and transversal cooling channels are more effective at cooling the block than those which offer only longitudinal channels.

Drawing conclusions from the numerical results comparison of both cases of different sets of convection coefficients isn't as linear as drawing from the comparison of graphical results. A direct comparison of temperature gradients of the same geometry in both cases isn't very reliable, considering that both sets of convection coefficients are quite different, as well as the conditions of both heating flows. Therefore, in order to properly compare the cooling efficiency of both these cases, the variation of the displacement (U2) at the top of the block was the variable considered to be the most appropriate. The displacement variable was addressed and studied in the following sections.

4.1.3. Creep Analysis Results – Temperature as Boundary Condition (TBC)

The first creep analysis run using ABAQUS was made with the thermal analysis results when the temperature is the boundary condition (TBC), that were obtained previously. After running the analysis and before proceeding into the study of the results, it was first necessary to choose an instant of time for which these results would be obtained graphically and numerically.

Considering that, when the airplane's engines are started and the flight cycle begins, the turbine blade temperature is at the room temperature of 20 ºC, it is only appropriate that all study variables obtained are at a time instant after the flight cycle time and cooling time has taken place and, therefore, the blade is at the same room temperature of 20 ºC as in the beginning. With that said, it is important to define for all rectangular block geometries, the time periods relevant for this study.

The first time period to consider is the flight cycle time. A flight cycle begins when the engine is started before takeoff, and ends after the airplane lands, when the engine is shut down. For the PDL-FNC flight considered in this study, the flight cycle takes 7492 s from beginning to end [2].

a)	b)
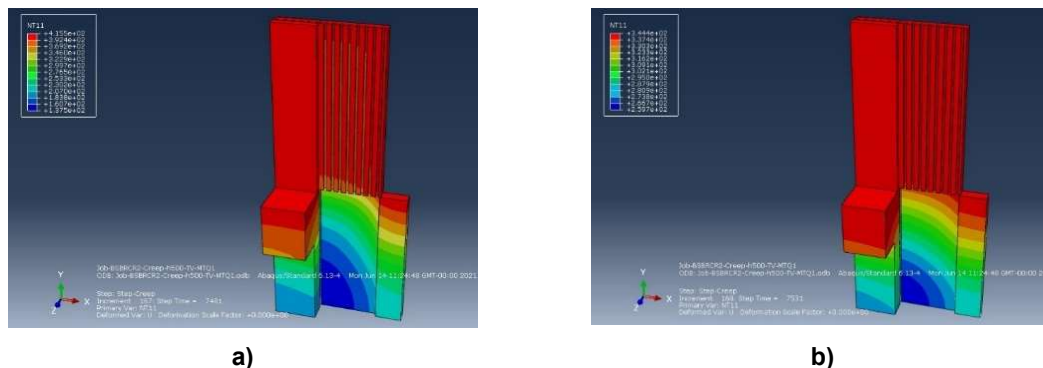
Figure 4.21 - Temperature distribution for the B2-14L geometry a) right before engine shutdown; b) right after engine shutdown (TBC)

At this time instant (engine shutdown), as can be seen in **Figure 4.21 a)** and **b)**, the rectangular block is still at very high temperatures. In fact, the wall temperature at 7492 s should be at 383 ºC according to the TIT data that was implemented in these analyses. This can be confirmed in **Figure 4.21 a)**, at a time instant immediately before the engine shutdown (7481 s), demonstrates that the wall is at a temperature of 415.5 ºC. Also at this time instant, it is possible to observe that the cooling channels' cooling flow is still in performance and effectively cooling the block. At the time instant immediately after the engine shutdown (7531 s), as can be seen in **Figure 4.21 b)**, the wall temperature is already at 344.4 ºC, lower than the 383 ºC that occurs at 7492 s , when the engine shuts down. It is also noticeable graphically and by the temperature gradients that the cooling fluid has ceased to flow in the cooling channels due to the engine shutdown, and so all block cooling will be achieved by natural convection and conduction.

An important note to make is that, as seen in the previous paragraph, there are variables calculated (in this case the temperature variable) for the time instants of 7481 and 7531 s, but no

variables were calculated for the time instant of 7492 s by the ABAQUS software. This is because when defining time increment sizes in the Step Module of the ABAQUS software, a maximum time increment of 50 s was specified for the step analysis. This means that, in most time increments, ABAQUS will calculate the requested variables in time intervals of 50 s - this is true for the majority of the analysis, though, in some of its more complex stages, ABAQUS will calculate variables for much smaller time intervals (down to a minimum of 0.0001 s). Because in this analysis it was left up to ABAQUS to define the time increments (within the intervals specified) for which the solicited variables would be calculated, and no specific time stamps were defined by the user, ABAQUS made its calculations for the aforementioned time instants of 7481 and 7531 s (with the already explained 50 s interval between both time instants).

The second time period relevant to the analysis is the surface cooling period. From the temperature data obtained from the flight data records, it was possible to extract the TIT values that were used in these analyses. However, when the engine is shut down and the flight cycle has reached its conclusion, the FDR ceases to be updated. Therefore, for the PDL-FNC flight studied in this thesis, the last temperature registered was 383 ºC at the time instant of 7492 s, which is the end of the flight cycle. So, to calculate the cooling of the block, it was necessary to assume a time period during which the wall temperature would decrease until the room temperature of 20 ºC. For this effect, a cooling rate of 1 ºC/s was added to the TIT data after the 7492 s mark and so, after 363 s, the wall temperature decreased from 383 ºC to 20 ºC, thus reaching the room temperature at the time instant of 7855 s [2]. In **Figure 4.22 a)** it is possible to observe that, at the time instant of 7881 s (ahead of the 7855 s time mark), the wall temperature is at 20 ºC, and other sections of the block are still, naturally, at higher temperatures.

| a) | b) |
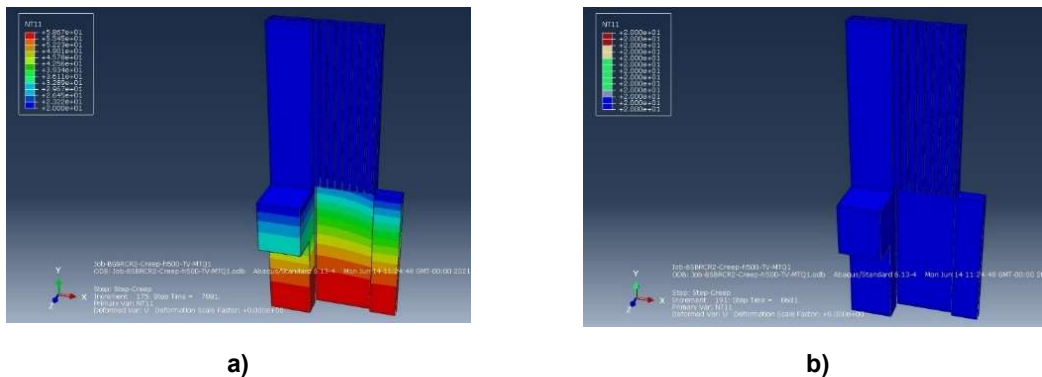
Figure 4.22 - Temperature distribution for the B2-14L geometry when the a) wall temperature is 20 ºC; b) block reaches 20 ºC uniformly (TBC)

The third and final time period is the uniform cooling period. This time period corresponds to the time necessary for the rectangular block to uniformly achieve the room temperature of 20 ºC.

Taking into consideration that the rectangular block geometries are different amongst themselves, due to the sizes (radius) and orientations of the cooling channels (though all rectangular

blocks share similar masses), it is only natural that some rectangular block geometries will take more time in reaching a uniform temperature of 20 ºC than others, due to different heat transfer rates.

After running the analyses for a longer period of time after the flight cycle time with surface cooling period had elapsed, it was possible to register the time instants for which all block geometries achieve the uniform room temperature of 20 ºC. From **Figure 4.22 b)**, it is possible to observe that, for the B2-14L geometry, the first time instant at which the whole block is at 20 ºC is 8681 s. For the remaining block geometries, these time instants (flight cycle time with uniform cooling period) can be consulted in **Table 4.6**, as well as the other relevant time periods.

Table 4.6 - Flight Cycle Time and Cooling Periods for the rectangular block geometries (TBC)

h = 500 W/m²K			
Rectangular Block Geometry	**Flight Cycle Time (s)**	**Flight Cycle Time with Surface Cooling Period (s)**	**Flight Cycle Time with Surface and Uniform Cooling Periods (s)**
B0	7492	7855	8763
B1-7L	7492	7855	8699
B2-14L	7492	7855	8681
B3-7L/11T	7492	7855	8715
B4-11L/17T	7492	7855	8722
B5-11L/11L	7492	7855	8639
B6-11L/17T-Net	7492	7855	8691

Knowing the time instants at which the whole block is at 20 ºC, it was then possible to retrieve the requested variables through the ABAQUS visualization module. The variables that were considered to be of interest in the creep analysis were the von Mises stress (SMises), stress in the longitudinal direction (S22), strain in the longitudinal direction (E22), displacement magnitude (UMag) and displacement in the longitudinal direction (U2).

The plots and numerical results of these variables, with the exception of the displacement in the longitudinal direction (U2), for the B2-14L and the B3-7L/11T rectangular block geometries, can be found in **Appendix C**.

Considering that the displacement in the longitudinal direction (U2) is the most significant variable in this study because it details the deformation of the block by the end of a flight cycle, a more detailed study of this displacement was conducted. The U2 displacement distribution for all block geometries can be viewed, affected by a deformation scale factor, from **Figure 4.23** to **Figure 4.26**.
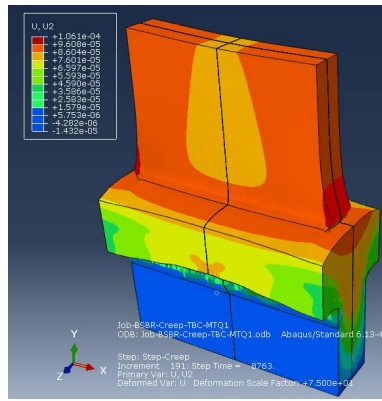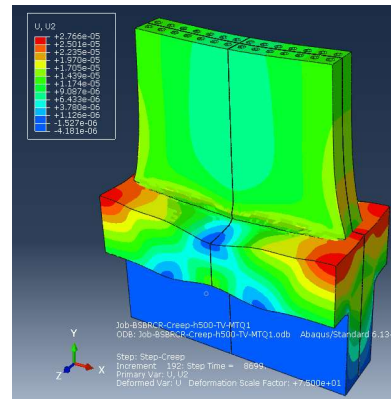
Figure 4.23 - Displacement in the longitudinal direction U2 distribution for the a) B0 block geometry; b) the B1-7L block geometry (TBC)
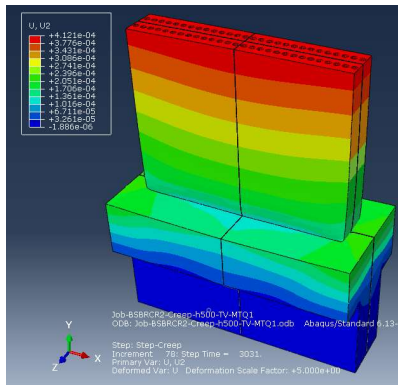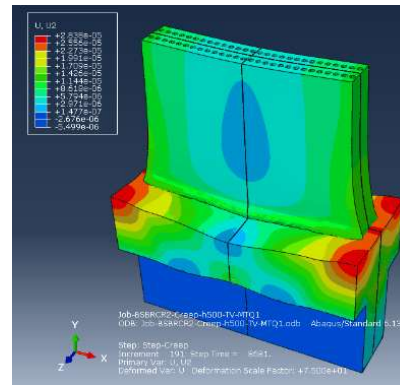
Figure 4.24 - Displacement in the longitudinal direction U2 distribution for the B2-14L block geometry at a) t = 3031 s – cruise flight phase; b) t = 8681 s – after the uniform cooling period (TBC)
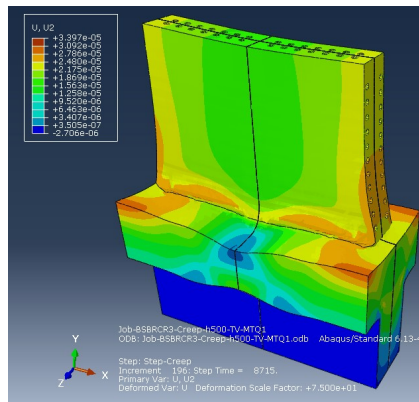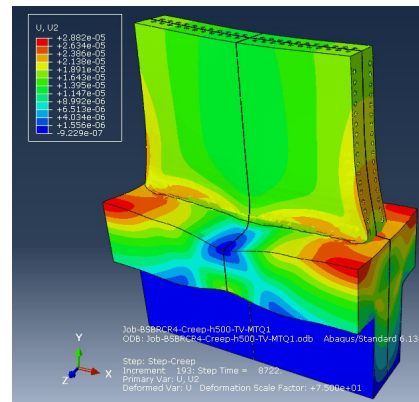
Figure 4.25 - Displacement in the longitudinal direction U2 distribution for the a) B3-7L/11T block geometry; b) B4-11L/17T block geometry (TBC)

<table>
<tr><td align="center">a)</td><td align="center">b)</td></tr>
</table>
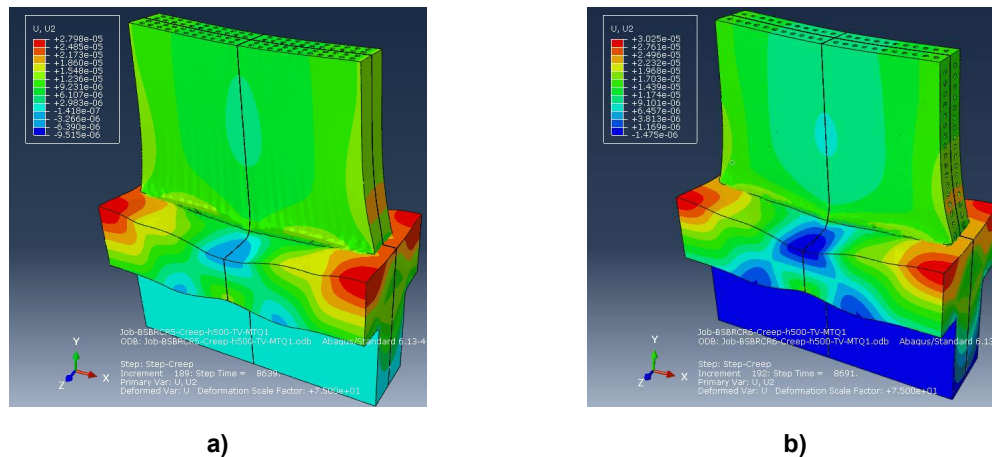
Figure 4.26 - Displacement in the longitudinal direction U2 distribution for the a) B5-11L/11L block geometry; b) B6-11L/17T-Net block geometry (TBC)

Along with addressing the U2 displacement distributions of the rectangular blocks by the end of the flight cycle with both cooling periods, it is of interest to register how these distributions are affected by the existence of very high temperatures and rotation speeds. For this effect, the U2 displacement distribution was obtained for an instant of time during the cruise flight phase (t = 3031 s) as can be seen in **Figure 4.24 a)**.

By looking at the U2 displacement distributions at both time instants, during the cruise flight phase and after the cooling phase, it is easy to notice that they are quite distinct. During the cruise flight phase, due to the effect of the turbine's high rotation speed, and facilitated by the hot gas high temperatures, the blade/block is driven forward in the longitudinal direction, and in this stage of the flight, some of the highest displacement values during the flight cycle are registered. From the study of the U2 displacement distribution in **Figure 4.24 a)**, it i*s easily concluded that the displacement increases from the base of the block to its top, where it reaches its highest value. This falls in line with what the expectations were of the displacement behavior for most of the duration of the flight cycle.

As for the displacement distribution by the end of the flight cycle and cooling period, it is possible to observe that, despite the expected differences due to different sizes, numbers and orientations of the cooling channels and therefore cooling efficiencies, all block geometries follow a similar pattern of deformation. By studying the U2 displacement distribution in any block geometry it is possible to distinguish several distinct deformation sections.

The first section of interest is the one that encompasses the area of the middle-block/top. This section registers the lower displacement values of the block (outside of the base), which can be explained by the fact that it experiences some of the lowest temperatures during the flight, due mainly to the influence of the cooling flow.

The second section in consideration is the one that comprises the area that envelops the first section. This section presents the highest values of U2 displacement of the block, with the exception of its base. This again can be justified by the cooling flow, which has a smaller influence on this section, as this section is farther away from the middle of the block, where some of the lowest temperatures can be found, as seen in the thermal analysis.

With further study of this second deformation section, it is possible to observe that the U2 displacement levels increase as they near the base and the leading and trailing edge, reaching its highest values by the block base and the bottom of both leading and trailing edge. It is also of interest to notice that by the bottom of the leading and trailing edge, there is significant deformation in the transversal direction (XX axis / U1 displacement).

One possible explanation for the U2 displacement distribution lies on the cooling periods of the block. As seen in **Figure 4.24 a)**, the block expands in the longitudinal direction during the duration of the flight cycle. However, when the flight cycle concludes and the cooling period begins, the block starts to contract due to the decrease in temperature and absence of rotation speed. As the top of the block retracts, due to reaching lower temperature values at a quicker rate when compared to the bottom of the block, it starts contracting the remainder of the block and forces the mass at the base to deform in the transversal direction (XX axis), as seen at the bottom of the leading and trailing edge (**Figure 4.24 b)**). These are the sections where the highest values of displacement in the entire block are found, and the displacement in the transversal direction (U1) is twice as much as the displacement in the longitudinal direction (U2). As the base continues to deform in the transversal direction, the section that encompasses the top and middle of the block contracts to compensate for this. This adds to the temperature explanation of why, at the end of the cooling period, this section exhibits lower values of U2 displacement/higher contraction when compared to the leading and trailing edge, as well as the rest of the block. This will be confirmed by the numerical results obtained for points at the top of the block and which are presented in **Table 4.7**, where it will also be possible to observe that these displacement values will be higher or lower, depending on the block geometry being studied.

Table 4.7 - Creep analysis results of the displacement in the longitudinal direction U2 and U2 Max for the rectangular block geometries (TBC)

Rectangular Block Geometry	U2 (m)					U2 Max (m)	t (s) - U2 Max
						$h = 500 \ W/m^2K$	
	Point 1	Point 2	Point 3	Point 4		Top of the block	
B0	8.749E-05	8.578E-05	8.570E-05	9.065E-05		9.587E-04	1163
B1-7L	9.963E-06	7.918E-06	7.894E-06	1.400E-05		5.061E-04	812.6
B2-14L	5.379E-06	3.305E-06	3.255E-06	9.332E-06		4.773E-04	830.6
B3-7L/11T	1.930E-05	1.738E-05	1.733E-05	2.305E-05		5.478E-04	870.2
B4-11L/17T	1.494E-05	1.298E-05	1.293E-05	1.871E-05		5.212E-04	835.6
B5-11L/11L	8.462E-06	6.448E-06	6.383E-06	1.257E-05		4.673E-04	839.3
B6-11L/17T-Net	1.182E-05	9.865E-06	9.800E-06	1.560E-05		5.040E-04	839.3

As previously mentioned, points 1 through 4 were chosen due to their positioning at the top of the block. These points' U2 displacement values provide an indication of how much the block deformed longitudinally during one flight cycle. Also, the comparison of the displacement values of the

block geometries demonstrates which block geometry deforms less in the longitudinal direction, regardless of their cooling efficiencies.

In line with what was observed in the graphical results, for all geometries the displacement values of point 4 are the highest, as this point is located at the leading and trailing edge. On the other hand, points 2 and 3, being positioned mid-block exhibit the lowest displacement values, also for all block geometries, as explained in the graphical results analysis.

Adding to the explanation of the U2 displacement distribution given in the study of the graphical results, is the study of the temperature at these points. It is important to note that point 4 constantly registers the highest values of temperature throughout the flight and practically does not benefit from the influence of the cooling flow. Therefore, because of the harsh conditions, it is expectable for this point to exhibit the highest displacement at the top of the block. At the same time, though points 2 and 3 also register the same high values of temperature as point 4, they benefit far more from the influence of the cooling flow than point 4, which in turn leads to lower displacements.

When directly comparing point results for different geometries, it becomes clear that the block geometries with both longitudinal and transversal cooling channels (B3-7L11T, B4-11L/17T and B6-11L/17T-Net) exhibit higher values of U2 displacement. On the other hand, block geometries with solely longitudinal channels (B1-7L, B2-14L and B5-11L/11L) display lower displacement values, with the B2-14L geometry being the one that displays the lowest values for all points.

This is unexpected when considering that the B3-7L11T, B4-11L/17T geometries presented higher levels of cooling efficiency when compared to those geometries with strictly longitudinal cooling channels. However, though they in fact are more effective at cooling down the block, it doesn't seem to have an implication on the U2 displacements at the top of the block. Possible reasons to explain this behavior can be found by studying the B2-14L geometry, given that it displays the lowest U2 displacement values.

The B2-14L geometry presents the highest number of longitudinal cooling channels in a single line. The cooling flows that originate from the longitudinal cooling channels have their exit at the top of the block. Therefore, it is possible to assume that, locally, the cooling efficiency at the top of the block will improve with the increase of the number of cooling channels. So, even though globally the B4-11L/17T geometry has a higher cooling efficiency, as seen in the thermal analysis study, locally, at the top of the blade, the B2-14L geometry with only longitudinal cooling channels presents lower U2 displacement results. In the case of the top of the block, the number of longitudinal cooling channels a block possesses may be more important than the geometry's overall cooling efficiency.

However, when looking at the B5-11L/11L geometry, one might think, because it presents 22 longitudinal channels, that it would be the geometry that yields the lowest displacement values, but as seen, it is not the case. In comparison, the B2-14L geometry has 14 longitudinal cooling channels in a single line, while B5-11L/11L has 22 divided by two lines of 11. Also, both of these block geometries (as well as the remaining ones) were designed to have the same mass. Looking at both of these factors, the lines of cooling channels and the mass of the block geometry, it is possible to assume that a single line of cooling channels may be an advantage as the distribution of mass comes into play.

As seen before, the B2-14L geometry has a single line of cooling channels located at the middle of the symmetrical rectangular block, whereas the B5-11L/11L has two lines of parallel channels. Looking at the mass of the blocks, one can assume, even though both geometries possess the same mass, that the B2-14L geometry has a more compact mass distribution, considering the single line of cooling channels, as opposed to the B5-11L/11L geometry which has to allocate its mass around two lines of cooling channels. Therefore, it is possible to assume that the B2-14L geometry possesses a sturdier build, which might offer added resistance against its permanent deformation, and hence lower U2 displacement values. This would also explain why the B6-11L/17T-Net geometry, which displayed significantly lower cooling efficiency, as seen in the thermal analysis (TBC), now produces lower displacements when compared to the B4-11L/17T geometry, as the former geometry has both its longitudinal and transversal cooling channels intersected and displayed in a net-like shape in the middle of the symmetrical block, and the latter geometry has the same number of cooling channels but separated in two lines, one transversal and one longitudinal. From these observations it is understandable that to properly evaluate how a block is going to deform at its top, one must weigh in several factors like the block's number of cooling channels, their location and orientation, and its mass distribution.

From the study of these rectangular block geometries, and in order to achieve lower U2 displacement values at the top of the block, one can draw two conclusions: the first conclusion is that, when it comes to producing lower displacement values, it is in general more effective to have less channels in a single line than more channels divided into two lines. Adding to this, one can assume that a geometry with a certain number of cooling channels in a single line, will produce lower displacements than a geometry with double the cooling channels but divided into two lines; the second conclusion that is possible to draw from this study is that, when displaying the cooling channels in a single line, and as far as can be seen from the limited number of geometries studied, as the number of projected cooling channels increases, so does the refrigeration at the top of the block, which leads in turn to lower U2 displacement values. This is valid independently for both the group of block geometries with solely longitudinal channels in a single line (B1-7L and B2-14L), and the group of block geometries with both longitudinal and transversal channels displayed in two lines (B3-7L/11T and B4-11L/17T).

Also in this displacement study, as can be seen in **Table 4.7**, one can observe that the maximum U2 displacement (U2 Max) for all geometries during the flight was also obtained as well as the time instants in which these displacements took place. Naturally, these maximum displacements occur at time instants that belong to the time period in which the flight conditions are the most extreme, which are, when the temperature is at its highest and the rotation speed is at its maximum, as can be confirmed by the plots for TIT and the rotation speed ω.

By studying the maximum displacements of all geometries, it is possible to come to the conclusion that they follow a similar course as the displacements after the flight cycle with cooling period. The geometries that registered the highest U2 displacements after the flight cycle (B3-7L/11T and B4-11L/17T) also registered the highest maximum displacements, and the same can be said of the geometries that registered the lowest U2 displacements after the flight cycle (B2-14L and B5-

11L/11L) as they too registered the lowest maximum displacements. However, it is worth noting that the B2-14L geometry displayed a higher value of maximum displacement, though by a small margin, when compared to the B5-11L/11L geometry, which inverses the results obtained when analyzing the displacement values at the end of the flight cycle with cooling, where the B2-14L geometry presented smaller displacements as opposed to the B5-11L/11L geometry, as seen above. This though is only an observation, as the maximum U2 displacement is merely a transitory displacement, whereas the U2 displacement by the end of the flight cycle with cooling is a permanent displacement and the one relevant to this study.

To finalize the study of the creep analysis in which the temperature is the boundary condition, an analysis of the B2-14L geometry was made but with the change of the cooling flow's convection coefficient to h=923 W/m^{2}K. These results and their comparison to previous results can be viewed in **Figure 4.27** and **Table 4.8**.

a)   b)
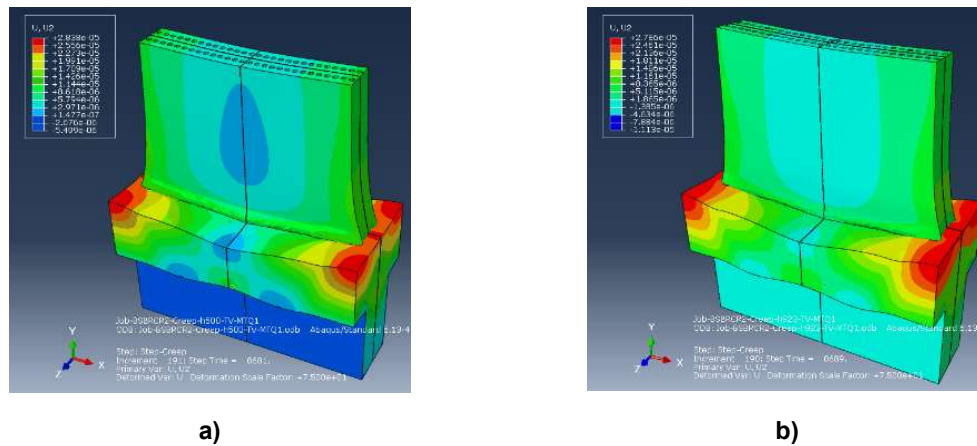
Figure 4.27 - Displacement in the longitudinal direction U2 distribution for the B2-14L block geometry when a) h=500 W/m^{2}K; b) h=932 W/m^{2}K geometry (TBC)

Table 4.8 - Creep analysis results of the displacement in the longitudinal direction U2 for the B2-14L block geometry when h=500 W/m2K and h=932 W/m2K geometry (TBC)

Rectangular Block Geometry	h (W/m^{2}K)	U2 (m)				U2 Max (m)	t (s) U2 Max
		Point 1	Point 2	Point 3	Point 4	Top of the block	
B2-14L	500	5.379E-06	3.305E-06	3.255E-06	9.332E-06	4.773E-04	830.6
B2-14L	923	1.828E-06	-6.044E-08	-6.660E-08	5.359E-06	4.313E-04	839.3

Looking at the results obtained by both analyses in **Table 4.8**, it becomes quite apparent that the increase of the convection coefficient of the cooling flow to h=923 W/m^{2}K yielded significant change in the displacement values at the top of the block. It is possible to observe that with the introduction of this second convection coefficient, the U2 displacement values of all points and even

U2 Max experienced considerable reduction, even to the point of contraction, as seen in points 2 and 3 (mid-block).

Hence, it is possible to draw the conclusion that, for the same geometry, the increase of the convection coefficient leads into less deformation and therefore smaller U2 displacements at the top of the block. This was to be expected as with the increase of the convection coefficient there is a corresponding decrease of temperature, due to an improved cooling performance of the cooling flow, as seen previously in the thermal analysis study (TBC).

4.1.4. Creep Analysis Results – Convection as Boundary Condition (CBC)

This second creep analysis was made using the thermal analysis results when convection is the boundary condition (CBC), that were obtained previously. As explained in the previous section (TBC), to study the results obtained by the creep analysis, the instant of time at which the rectangular block geometries are uniformly at the room temperature of 20 ºC after cooling down was chosen.

Three time periods relevant to the study were then defined: the flight cycle time, the surface cooling period, and the uniform cooling period, as explained before.

For this creep analysis, the flight cycle time naturally remains the same, as the flight time has not changed and is still 7492 s. As in this creep analysis the thermal results in which convection is the boundary condition were utilized, the block's walls are not at a constant temperature but display several temperatures, as explained in the thermal analyses section. In **Figure 4.28 a)** and **b)**, it is possible to observe the block's temperature distributions at the time instants just before and after the flight cycle time instant. The former demonstrates that the heating and cooling flows are still in effect, as the engine is still running. The latter, after engine shutdown, shows a significant drop of temperature, as there are no more hot gases exiting the combustion chamber, and therefore the heating flow's convection coefficient has been greatly reduced.

a)   b)
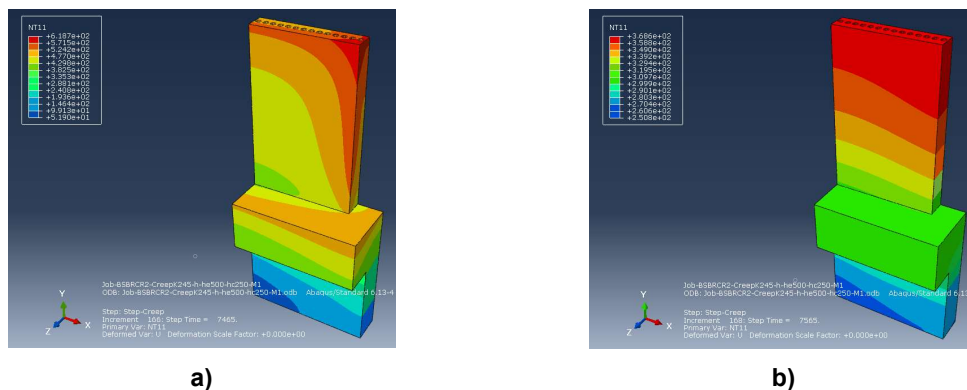
Figure 4.28 - Temperature distribution for the B2-14L geometry a) right before engine shutdown; b) right after engine shutdown (CBC)

At the same time, the cooling fluid has ceased to flow in the cooling channels, and so all block cooling will be achieved by natural convection. It can also be seen that, expectedly, the temperature at the top of the block is superior than at the bottom, as the surrounding atmosphere - represented by the heating flow with a now drastically reduced convection coefficient indicative of natural convection - is still at high temperatures, and the bottom of the block and base is still benefiting from the effects of the recently ceased cooling flow.

The second time period, the surface cooling period, also remains the same. In this case though, a thermal analysis in which convection is the boundary condition (CBC), this surface cooling period was not enforced to decrease the wall temperature until it reached 20º C, but to decrease the heating flow temperature from the last value registered at the end of the flight cycle (which will be different for each geometry, due to the multiplying factor, as explained before), until the same 20 ºC. This 363 s time period was assumed to be the time necessary for the hot gases surrounding the turbine blades to be exhausted from the engine, and so the time it takes for the atmosphere surrounding the blades/blocks to be at 20 ºC, which is to say, the room temperature. In **Figure 4.29 a)** it is possible to observe that globally, at the time instant of 7865 s (ahead of the 7855 s time mark, which corresponds to the flight cycle time with surface cooling period), all temperatures have decreased since the flight cycle time, and that the block exhibits lower values of temperature as opposed to its base, which is to be expected as the block is more exposed to the 20 ºC atmosphere, and therefore more prone to lose heat via natural convection, when compared to the base of the block. Obviously, unlike the TBC analysis in which at this time instant the block wall is immediately at 20 ºC as the temperature is forced as a boundary condition, the CBC analysis will take a significantly longer amount of time to reach the 20 ºC at any point of the block, as is observable in **Figure 4.29 a)**, where the block temperatures vary between 218.1 ºC and 169 ºC, at the same time instant.

| a) | b) |
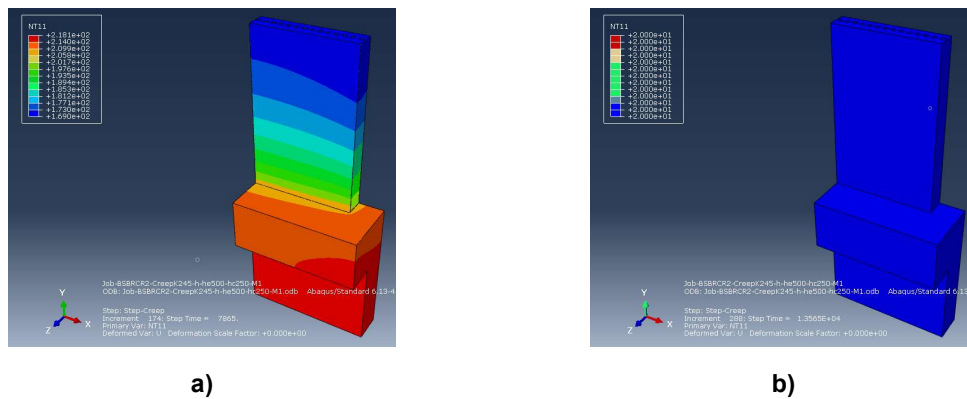
Figure 4.29 - Temperature distribution for the B2-14L geometry when the a) surrounding atmosphere is at 20 ºC; b) block reaches 20 ºC uniformly (CBC)

The third and final time period, the uniform cooling period, is, as explained before, the time period that corresponds to the time necessary for the rectangular block to uniformly achieve the room temperature of 20 ºC. In the case of the CBC analysis, this time period is considerably higher than the one necessary in the TBC analysis, as can be confirmed in **Figure 4.29 b)**, where for the B2-14L

block geometry, the time necessary to cool down the whole block to 20 ºC is 13565 s, much higher than the 8681 s needed in the TBC analysis.

This time discrepancy between both thermal analysis is explained by the fact that in the TBC analysis the wall temperature is forced to be at 20 ºC at the end of the surface cooling period, which in turn will accelerate the cooling of the internal block, making it easier and quicker to reach the uniform temperature of 20 ºC, as there is already a significant area of the block at that temperature. On the other hand, in the CBC analysis what reaches 20 ºC at the end of the surface cooling period is the heating flow temperature. This will allow for a longer period of heat transfer between the block and the surrounding atmosphere at 20 ºC, which, naturally, leads to a longer cooling period.

A longer surface cooling period though, seems to be much more consistent with reality, as an airplane engine can take approximately 2 to 4 hours to completely cool down to room temperature [43]. With the exception of B0 (no cooling channels), all rectangular block geometries have uniformly cooled down at the time mark surrounding 13500 s, which is approximately 3 hours and 45 minutes.

These results for the cooling periods serve to validate the rectangular block model as a fair approximation to the turbine blade, as well as the CBC thermal analysis employed. It is therefore possible to affirm that the thermal analysis in which convection is the boundary condition is a more realistic approach to the heating and cooling dynamics of a turbine blade, when compared to the TBC thermal analysis.

The time periods for all block geometries can be consulted in **Table 4.9.**

Table 4.9 - Flight Cycle Time and Cooling Periods for the rectangular block geometries (CBC)

h=500 W/m²K ; he=500 W/m²K ; hc=250 W/m²K			
Rectangular Block Geometry	Flight Cycle Time (s)	Flight Cycle Time with Surface Cooling Period (s)	Flight Cycle Time with Surface and Uniform Cooling Periods (s)
B0	7492	7855	21529
B1-7L	7492	7855	13736
B2-14L	7492	7855	13565
B3-7L/11T	7492	7855	14118
B4-11L/17T	7492	7855	13748
B5-11L/11L	7492	7855	12165
B6-11L/17T-Net	7492	7855	13915

With the knowledge of the time instants at which the whole block is at 20 ºC, the same variables of interest (SMises, S22, E22, UMag, U2) requested in the TBC creep analysis were retrieved through the ABAQUS visualization module.

The graphical and numerical results of these variables, with the exception of the displacement in the longitudinal direction (U2), for the B2-14L and the B3-7L/11T rectangular block geometries can be consulted in **Appendix C**.

As for the U2 displacement, its distribution for all block geometries can be viewed from **Figure 4.30** to **Figure 4.33**. It is of note that for some of the graphical results (B4-11L/17T), the U2 contour limits were somewhat altered in order to better illustrate the U2 distribution on the rectangular blocks.

a)   b)
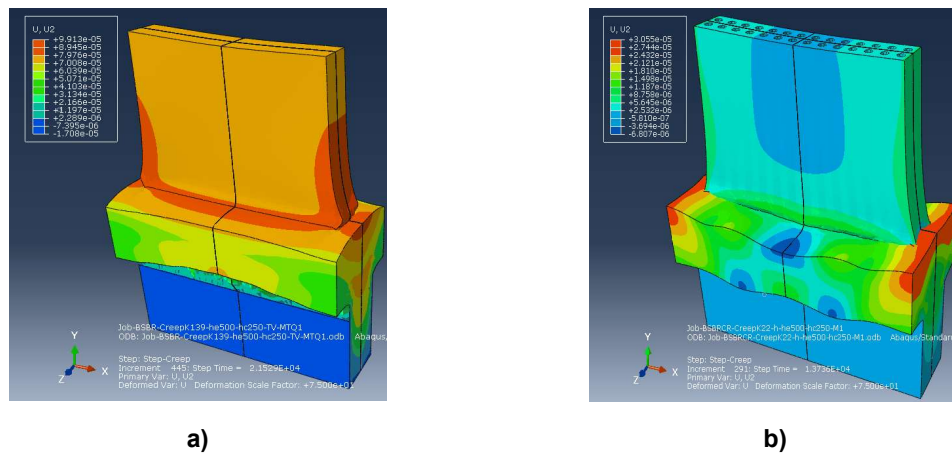
Figure 4.30 - U2 displacement distribution for the a) B0 block geometry; b) B1-7L block geometry (CBC)

a)   b)
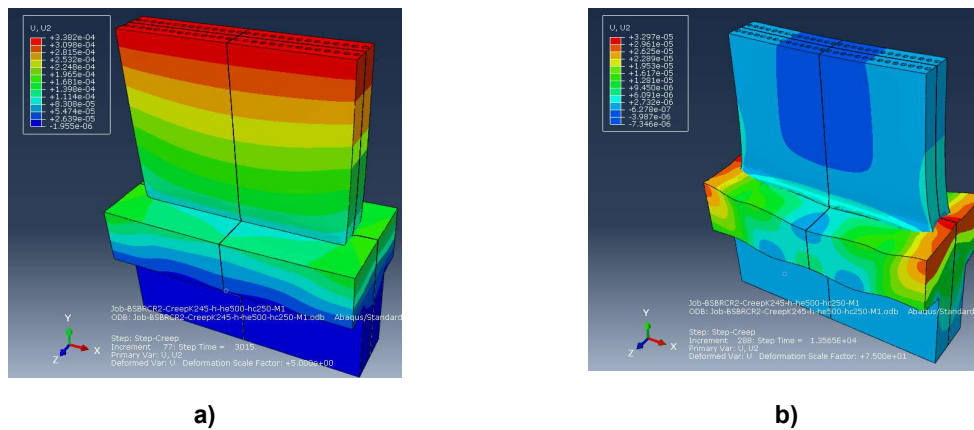
Figure 4.31 – U2 displacement distribution of the B2-14L block geometry for a) t=3015 s – cruise flight phase; b) t=13565 s – after the uniform cooling period (CBC)
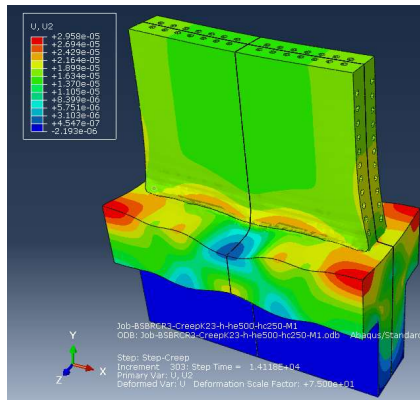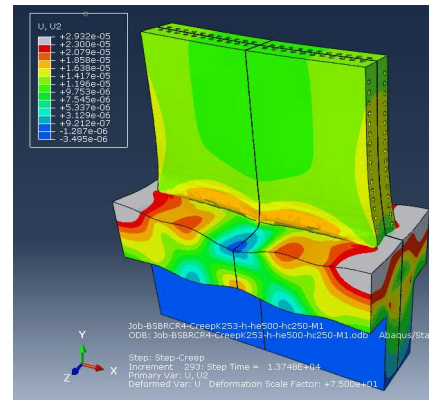
a)   **b)**

Figure 4.32 - U2 displacement distribution for the a) B3-7L/11T block geometry; b) B4-11L/17T block geometry (CBC)
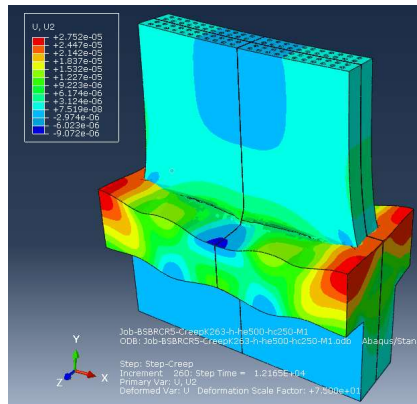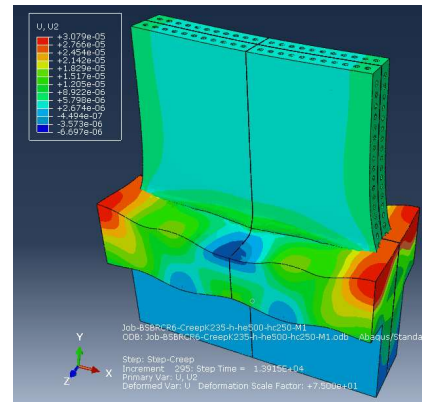
a)   **b)**

Figure 4.33 - U2 displacement distribution for the a) B5-11L/11L block geometry; b) B6-11L/17T-Net block geometry (CBC)

The creep analysis graphical results concerning the U2 displacement distribution also indicate, like the TBC creep analysis, that despite the expected differences due to the number and orientations of the cooling channels, all block geometries exhibit similar displacement distributions, as well as the same deformation sections, that were previously explained in the displacement study of the TBC creep analysis.

Comparing these results for all geometries to the ones obtained in the TBC creep analysis, it is apparent that the distributions follow similar patterns of behavior, as can be seen by their comparison with the distributions and different deformation sections portrayed in the U2 displacement study of the TBC creep analysis. Therefore, in graphical terms, it is acceptable to draw the same conclusions as the ones drawn in the TBC creep analysis.

To properly gauge the difference in U2 displacement between both the CBC and TBC creep analysis, the numerical results for the points at the top of the block were obtained and they can be consulted in **Table 4.10**.

Before proceeding into the comparison between these U2 displacement results and the ones obtained in the TBC creep analysis, it is first necessary to independently study the CBC creep analysis, which is to say, to analyze and compare the displacement values of the block geometries in order to evaluate how each geometry deforms in the longitudinal direction.

Table 4.10 - Creep analysis results of the displacement in the longitudinal direction U2 and U2 Max for the rectangular block geometries (CBC)

h=500 W/m^{2}K ; he=500 W/m^{2}K ; hc=250 W/m^{2}K							
Rectangular Block Geometry	**U2 (m)**					**U2 Max (m)**	**t (s) - U2 Max**
	Point 1	**Point 2**	**Point 3**	**Point 4**		**Top of the block**	
B0	7.596E-05	7.432E-05	7.424E-05	7.901E-05		9.619E-04	1079
B1-7L	2.982E-06	1.665E-06	1.654E-06	5.780E-06		4.085E-04	835.6
B2-14L	-4.173E-07	-1.600E-06	-1.603E-06	2.013E-06		3.893E-04	815.2
B3-7L/11T	1.574E-05	1.464E-05	1.463E-05	1.813E-05		4.218E-04	835.6
B4-11L/17T	1.185E-05	1.078E-05	1.078E-05	1.416E-05		4.112E-04	797.9
B5-11L/11L	3.844E-07	-5.302E-07	-5.567E-07	2.670E-06		3.670E-04	815.2
B6-11L/17T-Net	4.161E-06	2.953E-06	2.932E-06	6.653E-06		3.963E-04	815.2

Just like in the TBC creep analyses, and in line with what was presented in the graphical results, it is perceivable for all geometries, that points 2 and 3 exhibit the lowest displacement values whereas point 4 presents the highest. This, as previously explained, is due to their location, as points 2 and 3 are positioned mid-block and point 4 is positioned at the leading and trailing edge. As was seen in the CBC thermal analysis, point 4 registers the highest temperature on the block during the flight and benefits only a fraction from the cooling flows, whereas points 2 and 3 experience lower temperatures due to being closer to the area of influence of the cooling flows. This, naturally, reflects itself on the displacements of these points.

Also, by the comparison of the U2 displacements of all geometries, it is concluded, like in the TBC creep analysis, that block geometries with both transversal and longitudinal cooling channels (B3-7L11T, B4-11L/17T and B6-11L/17T-Net) present higher values of displacement for all points of analysis, as opposed to those with solely longitudinal channels (B1-7L, B2-14L and B5-11L/11L) – an observation also made in the TBC creep analysis, which means that when it comes to the number, orientation and positioning of the cooling channels of all geometries, it is possible to draw the same conclusions that were drawn in the U2 displacement study of the TBC creep analysis.

A point of interest in this analysis was the appearance of contraction displacements in the B2-14L and B5-11L/11L geometries. Like the TBC creep analysis, B2-14L is the geometry that contracted

more during the cooling period, as it can be seen for points 2 and 3, as the negative displacement values are superior than those presented by the B5-11L/11L geometry.

As for the maximum U2 displacements, these occur at approximately the same time period in which the flight conditions are at their most extreme, as previously explained. As for the maximum displacements themselves, they follow the same pattern of deformations for all geometries after the flight cycle, and so, it is possible to observe that the geometries that registered the highest U2 displacements after the flight cycle (B3-7L/11T and B4-11L/17T) also registered the highest maximum displacements, and the geometries that registered the lowest U2 displacements after the flight cycle (B2-14L and B5-11L/11L) also registered the lowest maximum displacements. Again, this was also noticeable in the TBC creep analysis – in fact, the U2 maximum displacements of the CBC creep analysis for all geometries follow the exact same pattern of deformation as in the TBC creep analysis, even to the point of the B5-11L/11L geometry displaying a lower maximum displacement when compared to the B2-14L geometry (which displayed lower U2 displacements at the end of the flight cycle with cooling when compared to B5-11L/11L).

Finally, comparing both methods of creep analysis, it is quite clear that the CBC creep analysis presents lower U2 displacement values for all points and for all geometries when compared to the TBC creep analysis. Both analyses follow the same patterns of deformation and the same displacement relations between all geometries, as seen in **Table 4.11**, where a ranking of block geometries was assembled, displaying the U2 displacements for all geometries, from the highest contraction/lowest displacement values to the highest displacement values.

As observed, and previously noted, both creep analyses exhibit the same relative results when it comes to the block geometries – from those that display the lowest displacement values/highest contraction, all the way down to those that display the highest displacement values/highest expansion. It is easy to observe from **Table 4.11**, that the geometries with solely longitudinal channels are located at the top of the table, whereas the geometries with both longitudinal and transversal channels are at the bottom (along with the B0 geometry which has no cooling channels), as discussed previously when studying both creep analyses.

As for comparing the U2 displacements of both creep analyses, a direct comparison between points for the same geometry leads to the conclusion that the TBC creep analysis exhibits significantly higher values of displacement, as opposed to the CBC creep analysis – with emphasis on the geometries with solely longitudinal channels.

To justify the differences of displacement in both creep analyses, the most important factor to consider is the cooling period (surface and uniform). As discussed earlier, both creep analyses have different cooling periods due to having different cooling approaches. When convection was used as the boundary condition, the cooling period was significantly longer than when the temperature was the boundary condition, leading to a longer cooling process. This longer period of time, in turn, led to a longer period of contraction for the block, after the expansive process it underwent throughout the duration of the flight. Naturally, as the block contracted for a longer period of time, at the end of the cooling process it exhibits lower U2 displacement values with some geometries, like the B2-14L and

B5-11L/11L geometries, displaying negative values of displacement or contraction displacements at the middle of the block (points 2 and 3).

Table 4.11 - Creep analysis block geometry ranking, from the lowest U2 displacement/highest contraction to the highest U2 displacement (CBC and TBC)

Block Geom.	h=500 W/m²K ; he=500 W/m²K ; hc=250 W/m²K							
	U2 (m) CBC Creep Analysis				U2 (m) TBC Creep Analysis			
	Point 1	Point 2	Point 3	Point 4	Point 1	Point 2	Point 3	Point 4
B2-14L	-4.17E-07	-1.60E-06	-1.60E-06	2.01E-06	5.37E-06	3.30E-06	3.25E-06	9.33E-06
B5-11L/11L	3.84E-07	-5.30E-07	-5.56E-07	2.67E-06	8.46E-06	6.44E-06	6.38E-06	1.25E-05
B1-7L	2.98E-06	1.66E-06	1.65E-06	5.78E-06	9.96E-06	7.91E-06	7.89E-06	1.40E-05
B6-11L/17T Net	4.16E-06	2.95E-06	2.93E-06	6.65E-06	1.18E-05	9.86E-06	9.80E-06	1.56E-05
B4-11L/17T	1.18E-05	1.07E-05	1.07E-05	1.41E-05	1.49E-05	1.29E-05	1.29E-05	1.87E-05
B3-7L/11T	1.57E-05	1.46E-05	1.46E-05	1.81E-05	1.93E-05	1.73E-05	1.73E-05	2.30E-05
B0	7.59E-05	7.43E-05	7.42E-05	7.90E-05	8.74E-05	8.57E-05	8.57E-05	9.06E-05

In conclusion, not only the CBC creep analysis produces lower displacement values/higher contraction at the end of a flight cycle and subsequent cooling period, it also portrays an approach that is closer to reality, as seen in the study of the cooling periods, when compared to the TBC creep analysis. Therefore, one can conclude that the thermal analysis when convection is the boundary condition is the most adequate for the study of the rectangular blocks and turbine blade.

To finalize the study of the rectangular blocks, CBC creep analyses were run for the B2-14L and B3-7L/11T geometries when using the second set of convections coefficients. The results of these analyses and their comparison to previous results can be viewed in **Figure 4.34** and **Table 4.12**.

| | a) | | b) |
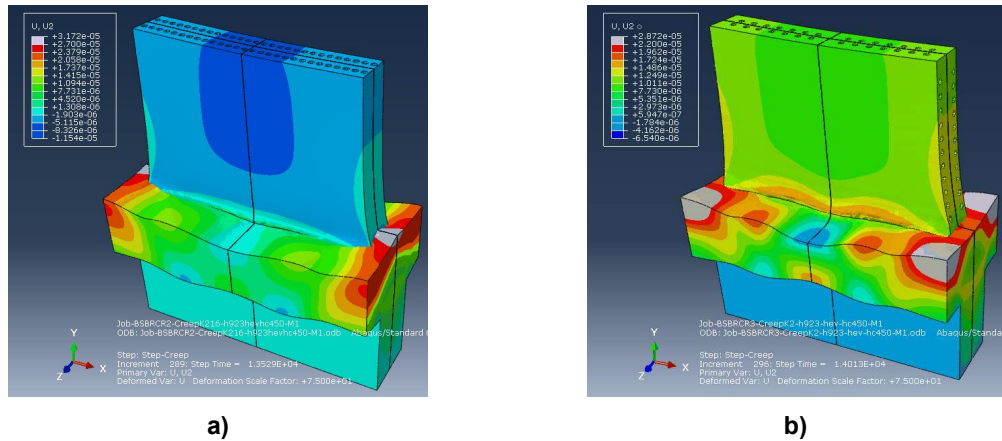
Figure 4.34 - U2 displacement distribution when using the second set of convection coefficients for the a) B2-14L geometry; b) B3-7L/11T geometry (CBC)

Table 4.12 - Creep analysis results of the displacement in the longitudinal direction U2 for the B2-14L and B3-7L/11T geometries with two sets of convection coefficients (CBC)

Rect. Block Geometry	h (W/m²K)	he (W/m²K)	hc (W/m²K)	U2 (m)			
				Point 1	Point 2	Point 3	Point 4
B2-14L	500	500	250	-4.173E-07	-1.600E-06	-1.603E-06	2.013E-06
B2-14L	923	hev	450	-4.560E-06	-5.743E-06	-5.687E-06	-2.279E-06
B3-7L/11T	500	500	250	1.574E-05	1.464E-05	1.463E-05	1.813E-05
B3-7L/11T	923	hev	450	9.832E-06	8.711E-06	8.710E-06	1.224E-05

Looking at the graphical results obtained in **Figure 4.34**, the U2 displacement distributions for both geometries follow the same patterns of deformation that have been seen and explained before, with differences only in the size of the deformation sections.

As for the numerical results of both analyses seen in **Table 4.12,** and starting with the study of the B2-14L geometry, it is clear that the usage of the second set of convection coefficients leads to a higher level of contraction at the top of the blade, when compared to the first set of convection coefficients - in fact, all point values at the top of the block exhibit contraction displacements. This is justified by the increase of the cooling channels' cooling flow and the surface film cooling flow convection coefficients. Despite the increase of the heating flow coefficient for all surfaces of the block, the influence of both cooling flows is more than enough to override this added heating effect.

The numerical results of both analysis for the B3-7L/11T geometry also points to the same behavior of the B2-14L geometry, as there is a reduction of the U2 displacement values with the second set of convection coefficients.

When comparing the results of the B2-14L and B3-7L/11T geometries when using the second set of convection coefficients, it is observable that the conclusions drawn are not different than those drawn when using the first set of convection coefficients. With the second set of coefficients, the U2 displacement results remain considerably different between both geometries, as the B2-14L geometry exhibits much lower displacement values/higher contraction than the B3-7L/11T geometry.

In conclusion, considering all the assumptions made regarding the data input, it is possible to consider that all the analyses run on the rectangular block, be them thermal or creep analyses, delivered consistent results for the U2 displacement variable, based on the expected influence of cooling efficiency on creep deformation. Hence, having these thermal and creep models running consistently on the rectangular block, they can now be applied to the turbine blade model, as will be seen in the following section.

4.2. Turbine Blade

Before proceeding to the thermal and creep analyses of the turbine blade, it was first necessary, like the rectangular block model, to choose study points for which results could be obtained. For this effect six points were chosen, four at the top of the blade, points 1 through 4, and two mid-blade, points 5T and 6T which are purely thermal points for which only temperature values will be obtained. Like the rectangular block, points 1-4 were chosen due to their location at the top of the blade, where the displacements relevant to this study take place. The location of these points and their coordinates can be viewed in **Figure 4.36** and **Table 4.13.** The origin and orientation of the coordinate system can be seen in **Figure 4.35.**
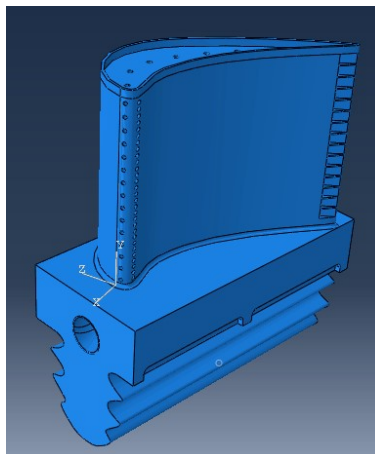
Figure 4.35 - Turbine blade coordinate system
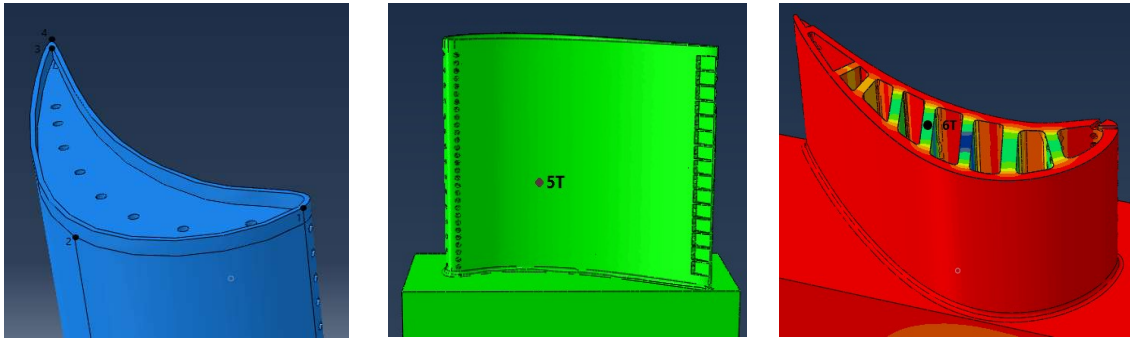
Figure 4.36 - Points selected for the turbine blade

Table 4.13 - Point coordinates for the turbine blade

Points	Point Coordinates (mm)		
	x	y	z
1	0	22.431	0
2	-10.804	21.569	4.576
3	-23.805	22.431	-14.497
4	-24.114	22.431	-15.035
5T	-9.702	8.745	-2.376
6T	-12.913	10.931	-0.953

4.2.1. Thermal Analysis Results – Temperature as Boundary Condition (TBC)

After validating the thermal and creep analyses on the rectangular block, the same analyses in the same conditions were performed on the turbine blade. Therefore, the first thermal analysis run was the TBC analysis, in which the temperature is the boundary condition. Because the same model of analysis is being run, the same time instant of 3000 s (cruise flight phase) was used for the study of the temperature distributions, and the same channels' cooling flow convection coefficients of h=500 W/m^{2}K and h=923 W/m^{2}K were employed. The temperature distributions of the turbine blade using h=500 W/m^{2}K can be viewed in **Figure 4.37**.

From the observation of the temperature distributions, it is clear that the cooling flow is effectively cooling down the interior of the blade. The blade's walls and top of the base are at 750 ºC, as expected per the instant of time (TIT = 750 ºC at 3000 s). At the same time, the interior of the block registers the lowest temperatures as it is closest to feeling the effect of the cooling flow.

Looking at the middle of the blade, one can observe that there is a section in which the temperatures are at its lowest (blue) – this can be explained by the fact that this fin is located in the section in which the width of the blade is the largest. This in turn means that the middle of the fin is farthest from the blade walls, which is the hottest section of the blade, while at the same time being

closest to the cooling flow. In fact, it is possible to conclude that with the reduction of the width of the blade, comes a consequential and gradual increase of the temperature of the internal fins.
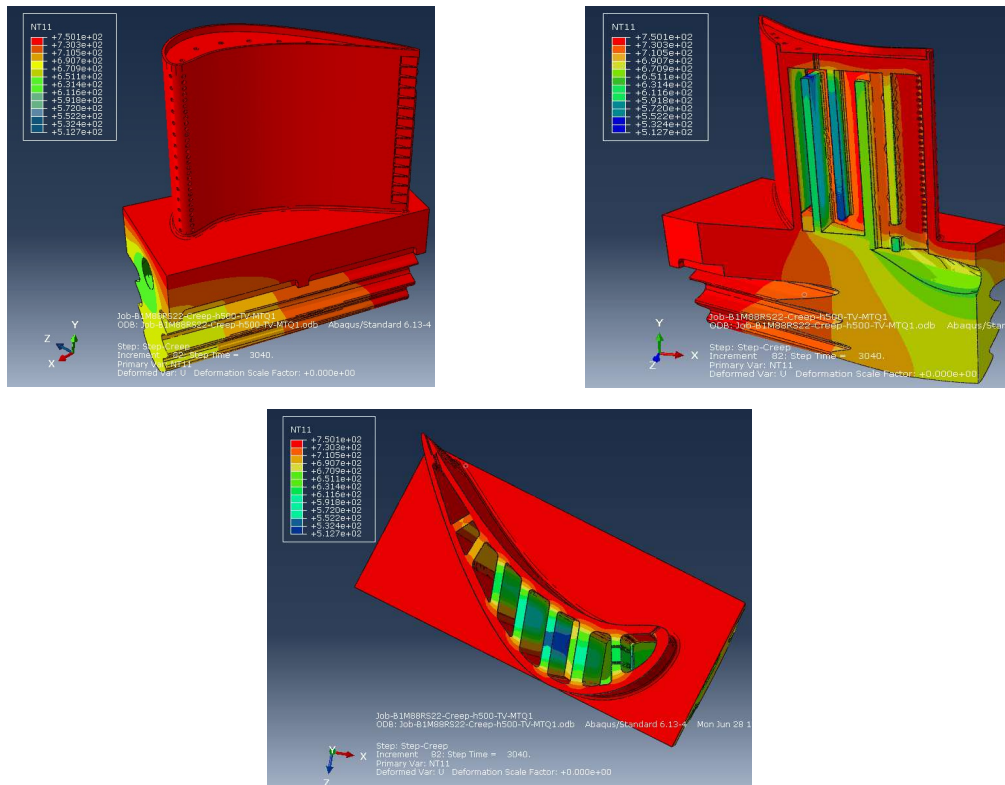
Figure 4.37 - Temperature distribution of the turbine blade using a convection coefficient of h=500 W/m²K (TBC)

As for the numerical results for both cooling flow convection coefficients, they can be viewed in **Table 4.14**.

Table 4.14 - Temperature results for the turbine blade when h=500 W/m²K and h=923 W/m²K (TBC)

Number of Elements	Number of Nodes	h (W/m²K)	Time (s)	Temperature (ºC)	
				Wall Temperature	Point 6T
224197	347280	500	3040	750	576.8
224197	347280	923	3020	750	459.7

For both cooling coefficients, when looking at the temperature results for point 6T, it is easy to conclude that the cooling flow is having its effect as this temperature is significantly lower than the wall temperature. Also, when comparing the results of both convection coefficients, it is clear that the

increase of the convection coefficient value resulted in a decrease of temperature, due to the added cooling capacity of the cooling flow. Therefore, it is possible to state that for the same blade, with the increase of the convection coefficient of the cooling flow, comes a subsequent decrease in temperature in the interior of the blade - an expected conclusion that was also drawn in the rectangular block model analyses.

4.2.2. Thermal Analysis Results – Convection as Boundary Condition (CBC)

The second thermal analysis run was the CBC analysis, in which convection is the boundary condition. Like it was explained in the previous thermal analysis, this CBC analysis will be run in the same conditions as the one for the rectangular block. So, the study of the temperature distributions will be conducted at the 3000 s time instant and using the same two sets of convection coefficients. It is of interest to point out though, that the surface point for which the multiplying factor study was made was point 2, at the top of the convex section of the blade. This point, temperature-wise, will be between surface point 4, which registers the highest temperature, and surface point 5T, which registers the lowest temperature at the surface.

The temperature distribution of the turbine blade for the first and second set of convection coefficients can be viewed in **Figure 4.38** and **4.39** respectively.

Figure 4.38 - Temperature distribution of the turbine blade for the first set of convection coefficients (CBC)
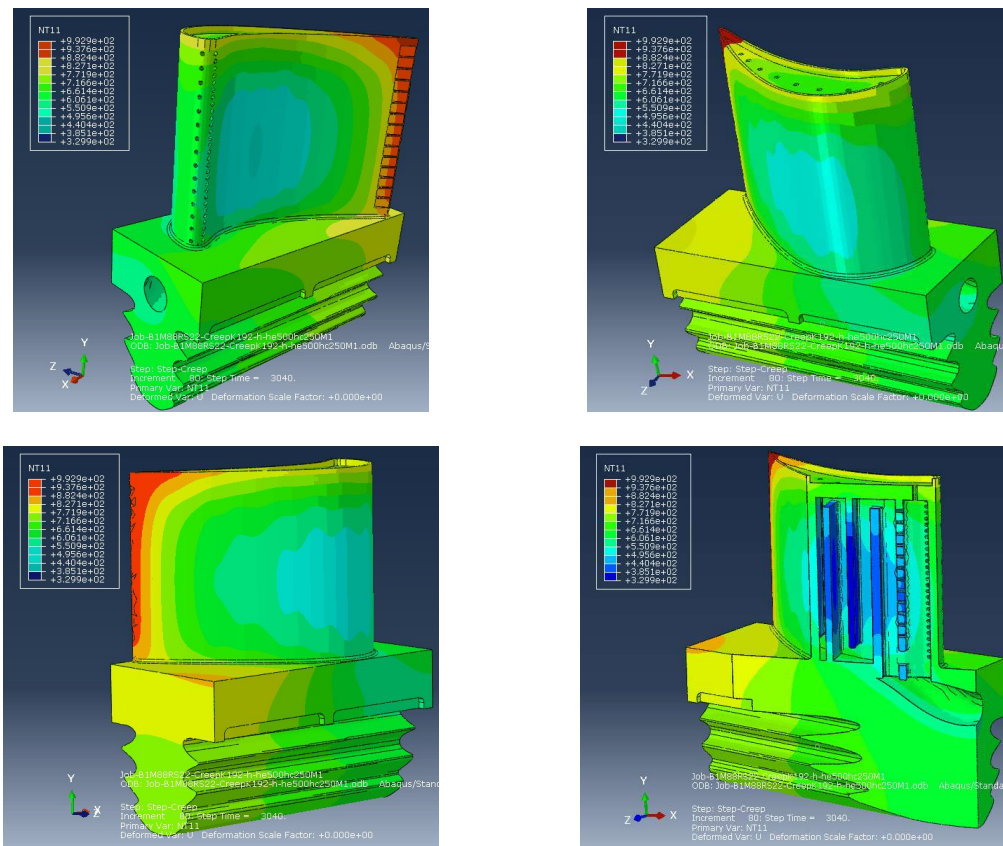
Through the analysis of **Figure 4.38,** it is noticeable that a cooling effect is taking place. Not only is this effect visible inside of the blade but also on the exterior, as can be seen in both the convex and concave sections of the blade. It is also possible to observe that the edges of the tip of the blade, and the areas closest to the trailing edge exhibit high temperature values, due to the effect of the heating flow, but it's the trailing edge that registers the highest temperatures of the blade. This can be explained by the fact that the trailing edge has the smallest width of the blade, and therefore is less subjected to the internal cooling flows while at the same time being under the direct effect of the heating flow. In contrast, the sections with the largest width of the blade present the lowest temperatures, as seen in the convex and concave surfaces – this can be justified by the cooling flow injecting an increased amount of cold air mass that fills up the hollow spaces of the widest sections of the blade, which in turn will produce a higher cooling effect as it increases the heat transfer rate.

It is worth mentioning that the surface film cooling flow originated from the channels seems to be effectively cooling the surface of the blade, as both the convex and concave surfaces exhibit lower temperatures for most of its surface area, right until the whereabouts of the blade tip and trailing edge.
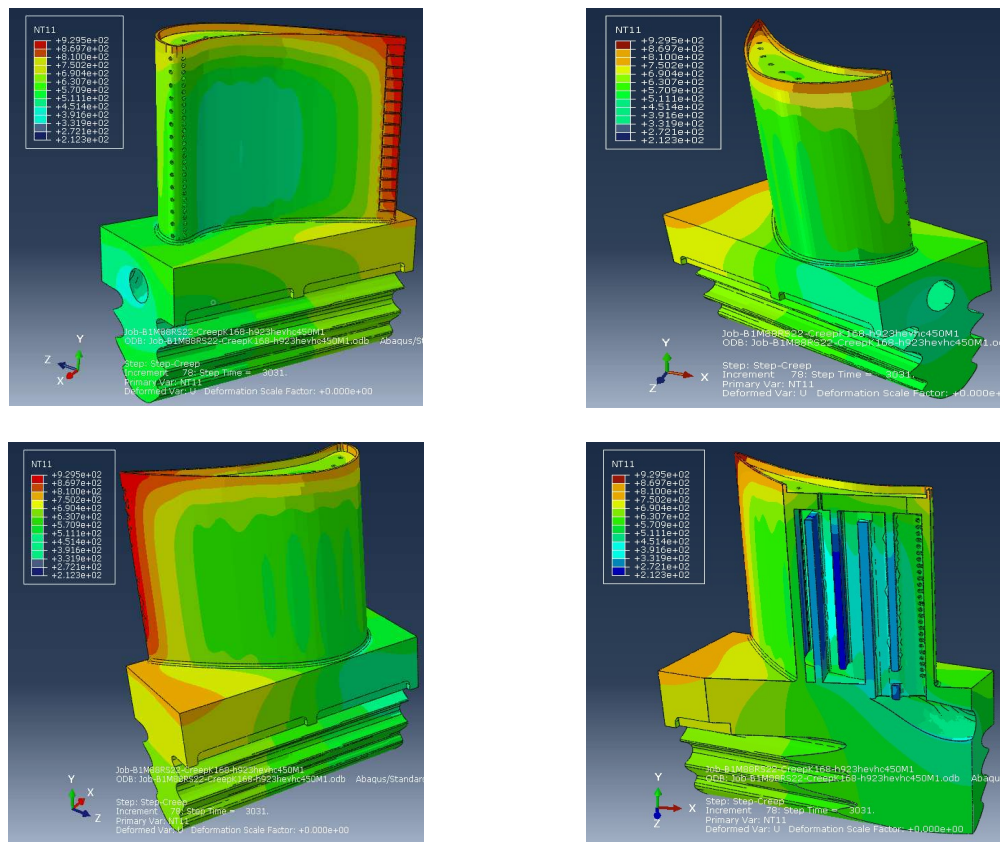
Figure 4.39 - Temperature distribution of the turbine blade for the second set of convection coefficients (CBC)

When it comes to the temperature distribution of the turbine blade when using the second set of convection coefficients, one can observe in **Figure 4.39** that they're quite similar to the distribution

when using the first set of coefficients, as they follow the same pattern of temperature layers. The main differences lie in the leading edge and convex surface.

Looking at the leading edge, it is visible that there's a significant portion of its area that is at a higher temperature than the rest of the convex and concave surfaces. At the same time, it is also visible that the convex surface is, as a whole, approximately at the same temperature, as opposed to the same surface in **Figure 4.38,** where the temperature decrease in the middle of the convex surface is clear. This can be explained by the increase of the heating flow coefficient – an increase that the surface cooling flow doesn't seem to be able to counter-balance. Of course, these differences between both analyses are merely relative for each analysis, as they reveal the different dynamics of the temperature distributions for each case. To properly compare the temperature results of both analyses, in absolute terms, one can observe **Table 4.15**.

Table 4.15 - Temperature results for the turbine blade with two sets of convection coefficients (CBC)

Temp. (K) Multip. Factor	h (W/m²K)	he (W/m²K)	hc (W/m²K)	Temperature (ºC) (t ≈ 3000 s)			Temp. Difference (ºC)
				Point 4 (High Temp. Point)	Point 2 (Approx. 750 ºC)	Point 5T (Low Temp. Point)	Point 4 – Point 5T
1.92	500	500	250	992.9	755.7	487.1	505.8
1.68	923	hev	450	929.5	754.5	450.9	478.6

In absolute terms, it is easy to conclude that using the second set of convection coefficients resulted in the reduction of the temperature values for all points considered. Not only that, but the temperature gradient decreased as well.

Even though the second set of convection coefficients has a significantly increased heating flow coefficient, both cooling flows' coefficients also have had considerable increases. The increase of the heating flow convection coefficient naturally leads to a higher heat transfer rate between the heating flow and the blade surface, which leads to higher values of temperature. However, this effect as a whole is negated by the increase of the cooling flows' convection coefficients, as can be seen by the temperature values for all points studied.

In conclusion, despite the relative differences between both temperature distributions, as can be observed in the graphical results, in absolute terms, the usage of the second set of convection coefficients produces lower temperature values than the first set of convection coefficients. This will lend itself to lower U2 displacement values, as will be seen in the following analyses.

4.2.3. Creep Analysis Results – Temperature as Boundary Condition (TBC)

The first creep analysis of the turbine blade model was conducted using the TBC thermal analysis results. Considering that both the thermal and creep analyses were validated on the rectangular block model, the creep analysis for the blade model was conducted using the same conditions employed previously. Given this, results were obtained for the instant of time at which the turbine blade is uniformly at the ambient temperature of 20ºC after cooling down.

As for the time periods considered in this study, both the flight cycle time and surface cooling period remain the same, due to the temperature being applied on the blade's surfaces remaining unchanged, as well as the cooling flow's convection coefficients, just like all the other conditions employed in the rectangular block model, with the obvious exception of the part being studied. The uniform cooling period will, naturally, be different, as the rectangular block geometry, though an approximation of the turbine blade, is still quite contrasting to it, shape-wise, which changes how long the part takes to completely cool down. A visual of the blade's temperature distribution at the time instants corresponding to the time periods can be consulted in **Figure 4.40** and **Figure 4.41**.

a)   b)
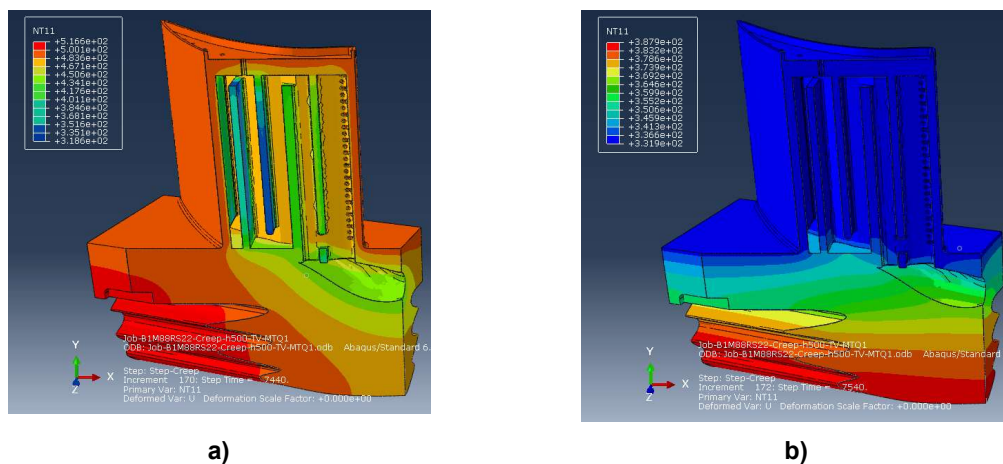
Figure 4.40 - Temperature distribution of the turbine blade a) right before engine shutdown; b) after engine shutdown (TBC)

From **Figure 4.40 a),** at a time instant of 7440 s (right before the engine shutdown), the blade's surface wall is at a temperature of 494 ºC, which as expected, is above the 383 ºC that the TIT data appoints for instant 7492, when the engine is shut down and the flight cycle time reaches its end. It can also be observed that, like the rectangular block model, the cooling flow is still in function, as the engine is still running. After the engine shutdown, as can be observed from **Figure 4.40 b)** (7540 s), the cooling flow has been disabled and the blade's surface walls are at 334 ºC, beneath the 383 ºC at the 7492 s time instant, as expected.

a)   **b)**
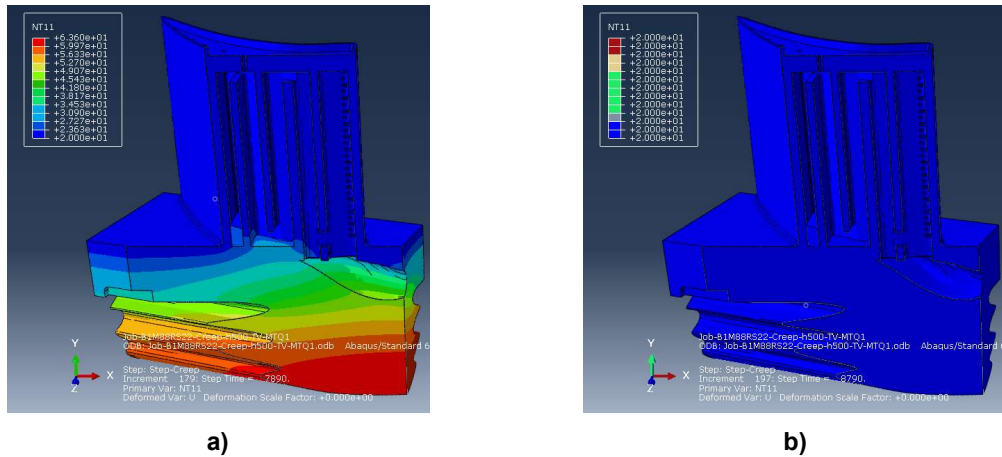
Figure 4.41 - Temperature distribution of the turbine blade when the a) wall temperature is at 20ºC; b) blade reaches 20 ºC uniformly (TBC)

At the end of the surface cooling period (**Figure 4.41 a)**), at the 7890 s time instant, it can be confirmed that the temperature of the blade surface is at the room temperature of 20 ºC, as well as most of the blade, with the exception of its base. The whole part, blade and base, finally cools down until 20 ºC uniformly at the 8790 s time instant which marks the end of the flight cycle time with both cooling periods (**Figure 4.41 b)**). As expected, the turbine blade's cooling process falls in line with what was observed and explained in the time periods' study from the creep analysis of the rectangular block.

The turbine blade's cooling time periods for the TBC creep analysis can be consulted in **Table 4.16**.

Table 4.16 - Flight Cycle Time and Cooling Periods of the turbine blade (TBC)

h (W/m²K)	Flight Cycle Time (s)	Flight Cycle Time with Surface Cooling Period (s)	Flight Cycle Time with Surface and Uniform Cooling Periods (s)
500	7492	7855	8790
923	7492	7855	8820

Knowing the time periods and the time instant at which the whole blade is at 20 ºC, the U2 displacement distributions could then be obtained. These results can be viewed for both convection coefficients in **Figure 4.42** through **4.44**.
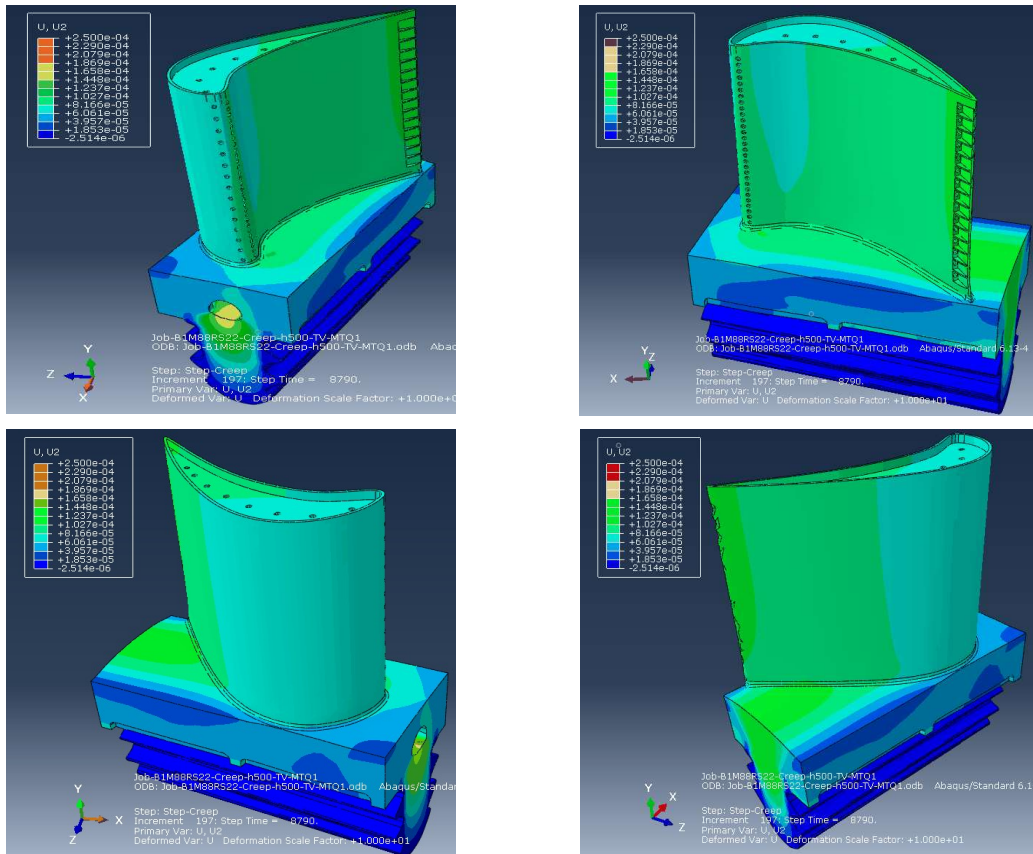
Figure 4.42 - U2 displacement distribution of the turbine blade when h=500 W/m^{2}K (TBC)
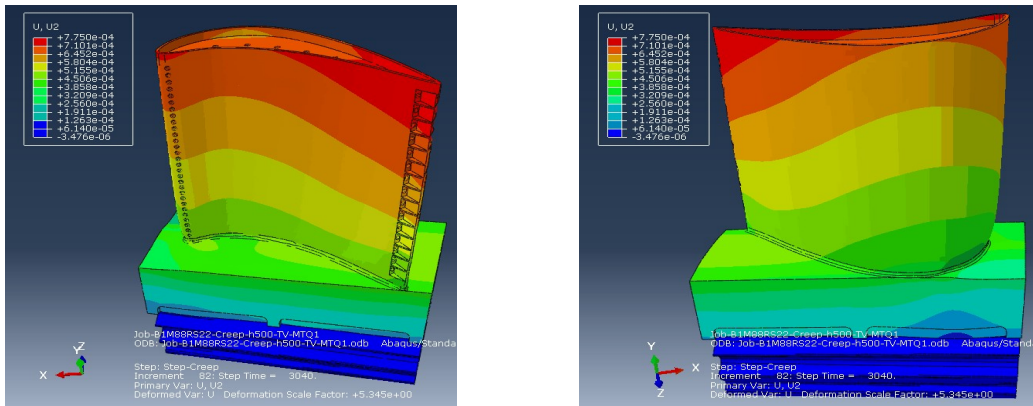
Figure 4.43 - U2 displacement distribution of the turbine blade when h=500 W/m^{2}K for t=3040 s (cruise flight phase) (TBC)

Before addressing the U2 displacement distributions of the turbine blade by the end of the flight cycle with both cooling periods, it is worth mentioning that at the 3040 s time instant, which corresponds to the cruise flight phase, the displacement distribution follows the same pattern of deformation as the rectangular blocks (**Figure 4.43**). As can be seen, the blade faces expansion and very high values of displacement in the longitudinal direction. The higher displacements are at the tip

of the blade while the lowest are by the base, which, as seen previously, is due to the very high temperatures and rotation speeds facilitating the deformation.

Observing the displacement distribution at the end of the cooling periods (**Figure 4.42**), three distinct sections of deformation can be established: the first section contains most of the leading edge, the leading end of the convex surface and the leading end of the concave surface; the second section contains the trailing end of the convex and concave surfaces; the third section contains the trailing edge and its close proximities.

The first section exhibits the lowest U2 displacement values of the blade – this, as explained in the TBC and CBC thermal analyses, is due to this section possessing the largest widths of the blade, which means that its hollow internal spaces contain a higher amount of cold air mass. This, as expected, potentiates the efficiency of the cooling flow in decreasing the blade's internal temperatures.

On the opposing side of the blade, the third section exhibits the highest U2 displacement values of the blade – unlike the leading edge, this section presents the lowest widths of the blade and, therefore, is less influenced by the cooling flow while being affected by the walls' temperature. This, naturally, leads to higher internal temperatures and higher displacement values. The second section, displacement-wise, falls in between both the first and second section, as expected.

In conclusion, one can state that with the increase of the width of the blade comes a decrease of the internal temperature and a consequential decrease of the U2 displacement values.
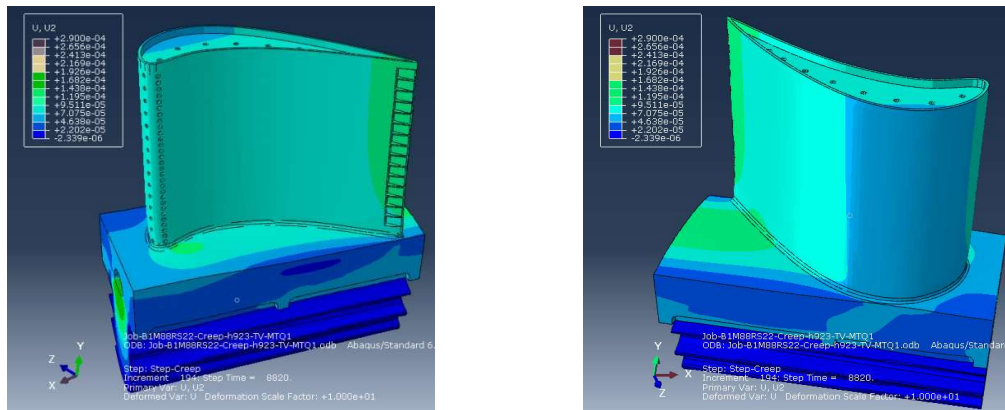
Figure 4.44 - U2 displacement distribution of the turbine blade when h=923 W/m^{2}K (TBC)

In **Figure 4.44,** it is observable that the graphical results when h=923 W/m^{2}K follow, in a somewhat analogous way, the U2 displacement distributions when h=500 W/m^{2}K. However, there are a few noticeable differences in the deformation sections. The first section now comprises only the leading end of the convex surface. The second section encompasses the leading edge and most of the concave surface. The third section, the trailing edge and its close surroundings, remains the same.

The main difference between both graphical results lies in the first section, as now it is only the leading end of the convex surface that exhibits the lowest displacement values of the blade, in contrast to the previous results that exhibited these low values in most of the leading end. This leads into the notion that the increase of the cooling flow was particularly felt at the center of the convex

surface, where the blade's largest width is located and, consequently, the cooling efficiency is improved.

It is important to note that the center of the convex surface has a lower displacement value than the center of the concave surface, even though both are located where the blade's width is the largest and where the cooling flow is most efficient. This difference in displacements can possibly be explained by the turbine's rotation. As the blade rotates in the direction pointing from the concave to the convex surface (counter-clockwise if the observer is looking in the negative direction of the XX axis, from the leading to the trailing edge), the concave surface will experience the effect of a higher centrifugal force when compared to the convex surface - this in turn will lead into a larger longitudinal projection of the concave surface, with the consequential increase of its U2 displacement.

To confirm the conclusions taken from the graphical results, a study of the numerical results was made. These results can be found in **Table 4.17**.

Table 4.17 - Creep analysis results of the displacement in the longitudinal direction U2 and U2 Max of the turbine blade (TBC)

h (W/m²K)	U2 (m)				U2 Max (m)	t (s) - U2 Max
	Point 1 Leading edge	Point 2 Center Convex Surf.	Point 3 Trailing edge	Point 4 Trailing edge tip	Trailing edge	
500	7.936E-05	7.136E-05	1.071E-04	1.082E-04	8.538E-04	1240
923	7.621E-05	6.728E-05	1.012E-04	1.023E-04	8.379E-04	1270

With the study of the numerical results, it is possible to make a few observations and confirm the conclusions drawn in the graphical results.

The first observation is that the lowest U2 displacement can be found on the center of the convex surface (point 2) – this, as seen and explained in the graphical results, is due to its positioning at the widest section of the blade.

As for the highest U2 displacement, it is significantly larger than the lowest displacement. It can be observed on the trailing edge tip (point 4) – this is due to its location on the blade where its width is the lowest.

The leading edge (point 1) displays higher values of U2 displacement than the center of the convex surface (point 2), which, as explained, is due to the difference of widths and, therefore, the influence of the cooling flow. At the same time, the leading edge displays considerably lower displacement values when compared to the trailing edge. Despite both having low widths when compared to the section of the blade that comprises point 2, the leading edge is very affected by the cooling flow as there is a significant mass of cold air nearby as opposed to the trailing edge which suffers a lesser influence by the cooling flow, while experiencing the same wall temperature as the leading edge.

These observations are valid for both analyses with different convection coefficients. The main difference between the analyses is that, as expected, the analysis in which the higher convection

coefficient was used delivered lower displacement values for all the points, even for the maximum displacement U2 Max. Again, it can be concluded that, for the same part/geometry, an increase of the convection coefficient leads to lower U2 displacement values.

Also of interest is the study of an additional point at the center of the concave surface, directly opposed to the center of the convex surface (point 2). This point, represented in ABAQUS by node 5268, for the analysis in which h=500 W/m²K registers, at the same time instant, the U2 displacement value of 8.213E-5 m which is larger than the value obtained for point 2 (center of the convex surface) as seen in **Table 4.17**. For the analysis in which h=923 W/m²K, node 5268 registers the U2 displacement value of 7.82E-5 m, again larger than the value obtained for point 2. This confirms that for both analyses, the center of the convex surface exhibits lower U2 displacement values when compared to the center of the concave surface, which, as explained in the study of the graphical results, could be due to the influence of the rotation speed and the centrifugal force.

4.2.4. Creep Analysis Results – Convection as Boundary Condition (CBC)

The second creep analysis was conducted using the CBC thermal analysis results. Like the TBC creep analysis, the CBC creep analysis was performed using the same conditions that were employed, explained and validated in the rectangular block analysis.

The same can be said of the time periods. The flight cycle time and surface cooling period remain the same. At the end of the flight cycle time, the engine is shut down and the heating and cooling flows cease to operate. At the end of the surface cooling period, the atmosphere surrounding the blade reaches the ambient temperature, which is to say 20 ºC. When the uniform cooling period has ended, the blade has been uniformly cooled down to 20ºC and the analysis of the U2 displacement can be made.

The temperature distributions of the blade at the time instants relating to these time periods can be viewed in **Figure 4.45**.

From **Figure 4.45 a),** at a time instant of 7440 s (right before the engine shutdown), it is possible to see by the high temperatures at the trailing edge that the heating flow is still in effect. At the same time, it is observable that the interior of the blade is having its temperatures decreased by the cooling channels' flow. In **Figure 4.45 b),** at the time instant of 7540 s, one can see the effects that the engine shutdown produced, as the heating flow and cooling flows ceased to operate. Analyzing the blade's temperature distribution, it is evident that, globally, all temperatures are decreasing and that the upper part of the blade is cooling down faster than the bottom part and the base, as it is more exposed to an atmosphere with a rapidly declining temperature.

After the surface cooling period (time instant of 7890 s), one can observe in **Figure 4.45 c)**, that the temperatures, globally, have significantly been reduced as the outside atmosphere's temperature has decreased to the ambient temperature of 20 ºC. From **Figure 4.45 d)**, it is clear that the blade has achieved a uniform temperature of 20ºC.
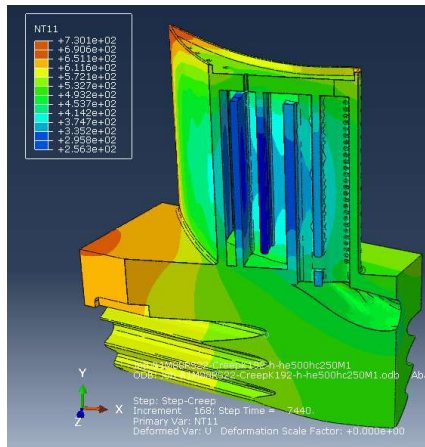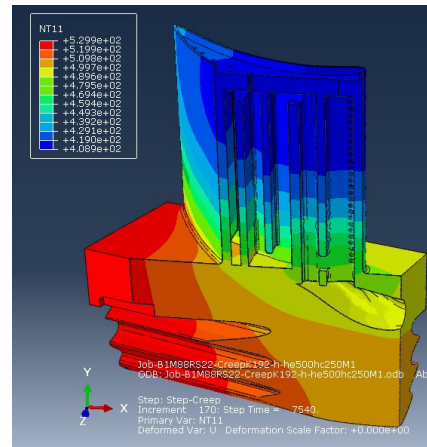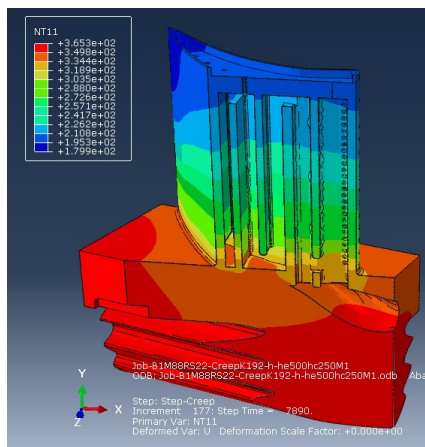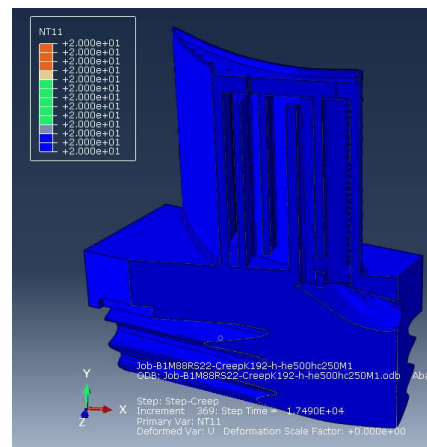
Figure 4.45 - Temperature distribution of the turbine blade a) right before engine shutdown; b) after engine shutdown; c) when the surrounding atmosphere is at 20 ºC; d) when the blade reaches 20 ºC uniformly

The turbine blade's cooling time periods for the CBC creep analysis can be consulted in **Table 4.18**.

Table 4.18 - Flight Cycle Time and Cooling Periods of the turbine blade (CBC)

h (W/m²K)	Flight Cycle Time (s)	Flight Cycle Time with Surface Cooling Period (s)	Flight Cycle Time with Surface and Uniform Cooling Periods (s)
500	7492	7855	17490
923	7492	7855	17381

Like the CBC creep analysis of the rectangular block geometry, it is possible to observe that the uniform cooling period is significantly larger than the one observed in the TBC creep analysis. This

was expected as the TBC analysis forces the blade's surfaces to be at 20 ºC by the end of the surface cooling period and, by consequence, accelerates the cooling down of the blade. In the CBC analysis, as explained in the CBC creep analysis of the rectangular block, at the end of the surface cooling period, it's the outside atmosphere that has reached the 20 ºC temperature and not the surfaces of the blade. This naturally leads to longer cooling periods, but also more realistic cooling periods, as concluded in the CBC creep analysis of the rectangular block.

With the knowledge of the flight cycle time with both cooling periods, the U2 displacement distribution could then be obtained. These results can be viewed for both sets of convection coefficients in **Figure 4.46** and **4.47**.
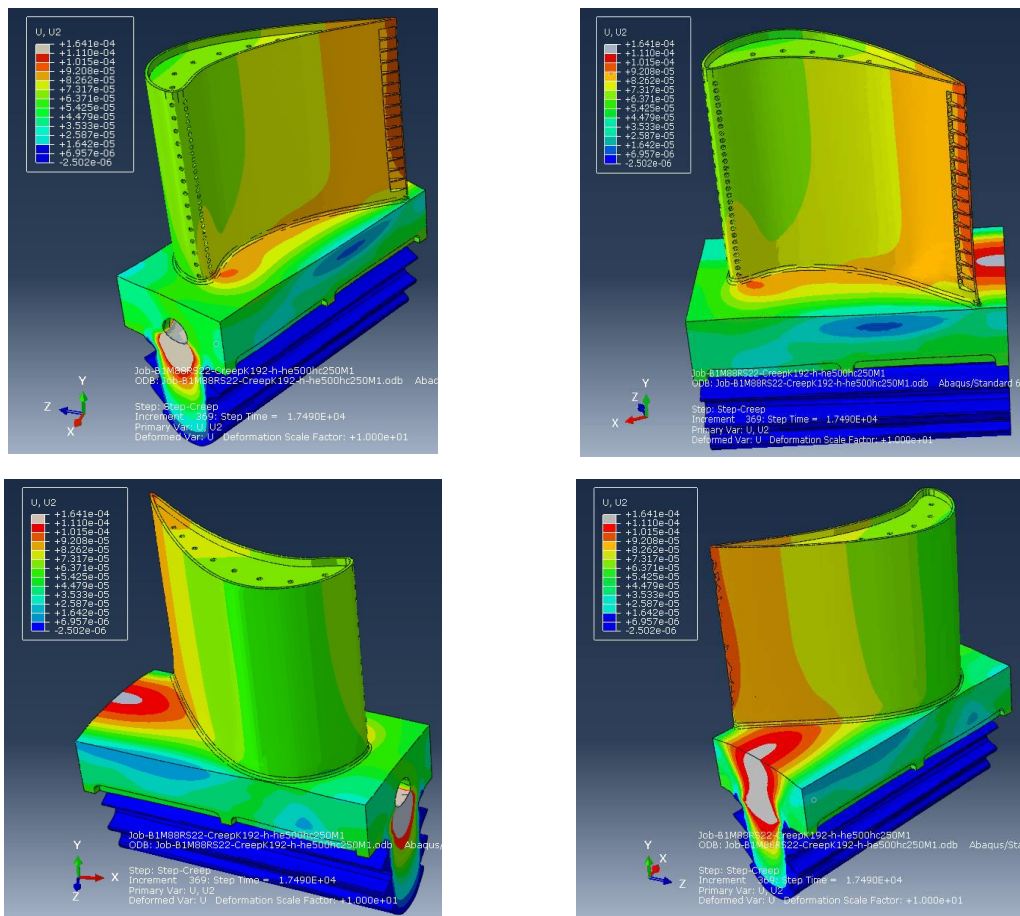
Figure 4.46 - U2 displacement distribution of the turbine blade for the first set of convection coefficients (CBC)

Like the TBC creep analysis, three distinct sections of deformation can be observed in the blades' displacement distribution: the first section contains most of the leading edge, the leading end of the convex surface and the leading end of the concave surface. The second section contains the

71

middle area of the convex and concave surfaces. The third section contains the trailing edge and the trailing end of the convex and concave surfaces.

Following similar patterns of deformation to the TBC creep analysis, it is observable that the first section exhibits the lowest U2 displacement values of the blade. This, as previously explained, is due to this first section having the largest widths of the blade and therefore containing within its internal spaces an increased mass of cooling air which, consequently, leads to lower internal temperatures in this section. In the particular case of the convex surface, it is possible to see that the surrounding area of its center presents the lowest displacement values of this section, as it also exhibits the highest widths of the blade.

The second section is a middle section that presents higher displacements than those of the first section, and lower displacements than those of the third section. This was expectable as the second section has smaller widths than the first section and larger widths than the third.

The third section exhibits the highest U2 displacements of the blade, due to this section presenting the blade's smallest widths and, therefore, limited cooling flow influence, as explained in the TBC creep analysis.

The CBC graphical results are clearer than the TBC graphical results in revealing that there's a gradual increase of the U2 displacement as the width decreases along the direction of the trailing edge. This conclusion though, was reached in both the TBC and CBC creep analyses.
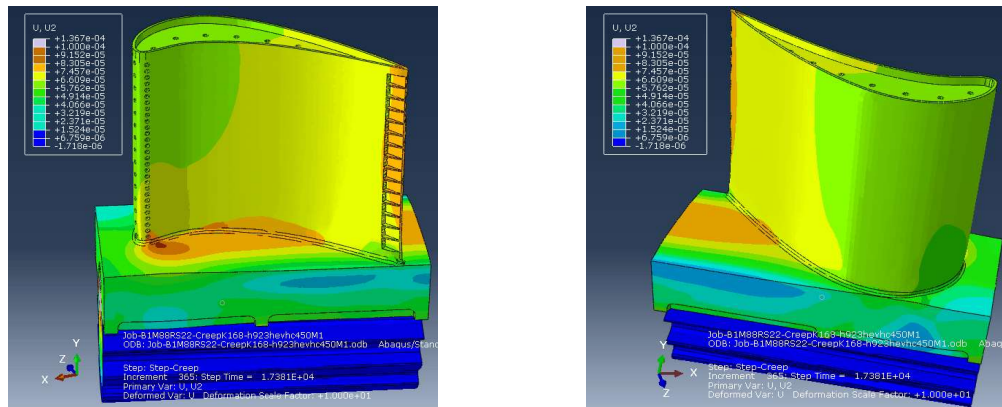
Figure 4.47 - U2 displacement distribution of the turbine blade for the second set of convection coefficients (CBC)

When using the second set of convection coefficients, the three distinct deformation sections are still perceivable but less clear than those observed using the first set of convection coefficients. Nevertheless, this analysis follows a similar pattern of deformation, as the leading end of the blade exhibits the lowest displacement values (with the convex surface presenting the lowest) and the trailing end exhibits the highest – which leads to the same conclusion regarding the width of the blade, as seen in the analysis in which was used the first set of convection coefficients.

To confirm the conclusions taken from the graphical results, a study of the numerical results was made. These results can be found in **Table 4.19**.

Table 4.19 - Creep analysis results of the displacement in the longitudinal direction U2 and U2 Max of the turbine blade (CBC)

h ; he ; hc (W/m²K)	U2 (m)				U2 Max (m)	t (s) - U2 Max
	Point 1 Leading edge	Point 2 Center Convex Surf.	Point 3 Trailing edge	Point 4 Trailing edge tip	Trailing edge	
500 ; 500 ; 250	6.962E-05	6.253E-05	9.282E-05	9.369E-05	8.557E-04	990
923 ; hev ; 450	6.356E-05	6.139E-05	7.530E-05	7.534E-05	7.327E-04	931

Just like the graphical results, it is possible to make the same observations as were made in the TBC creep analysis, for both sets of convection coefficients.

The lowest U2 displacement can be found in point 2, the center of the convex surface, as it is positioned where the blade's width is the largest. As seen before, the highest U2 displacement can be found where the width is the lowest, which is point 4, the trailing edge tip. The leading edge (point 1) again exhibits higher displacement values than the center of the convex surface (point 2) but lower values than the trailing edge tip (point 4) due to the larger influence of the cooling flow in the leading end of the blade.

As for the influence of both sets of convection coefficients, it can be concluded that the use of the second set produces lower displacement values for all points, as also seen in the CBC creep analysis of the rectangular block. Even though there's an increase of the convection coefficients of the heating flow, the increase of both cooling flows' convection coefficients is enough to compensate for it, which in turn leads to lower temperatures and, consequently, to lower displacement values.

It is of interest to register that when using the second set of convection coefficients, the U2 displacements at the trailing edge, though larger than those of the leading edge and the center of the convex surface, are lower in proportion, to those when using the first set of convection coefficients. This can be explained by the heating flow's convection coefficient at the tip of the blade. This coefficient, he=840 W/m²K, is larger than the one used in the first set, he=500 W/m²K. At the same time, the cooling channel's flow convection coefficient from the second set also increased its value in relation to the first set. However, in proportion, the cooling flow convection coefficient has a larger increase, from the first set to the second set, than the increase seen in the heating flow's convection coefficient. Therefore, it is possible to affirm that the cooling effect is more accentuated at the tip of the blade, when using the second set of convection coefficients, which in turn seems to benefit the trailing edge more than the leading end, in this case.

As for the study of the displacement at the center of the concave surface, U2 displacement values were obtained for the same point directly opposed to the center of the convex surface (node 5268) as in the TBC creep analysis. For the first set of convection coefficients, this point registers the U2 displacement value of 7.217E-5 m, which is larger than the displacement value obtained for the

center of the convex surface (point 2). For the second set of convection coefficients, node 5268 registers the U2 displacement value of 6.533E.5 m, also larger than the one obtained for point 2. This again leads to the conclusion that the center of the convex surface exhibits lower U2 displacement values than the center of the concave surface, which can be justified by the influence of the rotation speed and the centrifugal force – a conclusion that confirms the one previously obtained in the TBC creep analysis.

To finalize the CBC creep analysis study, it is possible to conclude that the U2 displacement values obtained when performing the CBC analysis are lower than those obtained when performing the TBC creep analysis. This was to be expected as in the CBC analysis the cooling periods are significantly larger than those of the TBC analysis, which in turn leads to a higher contraction of the blade and lower displacement values. This conclusion confirms and validates the one obtained in the rectangular block, as they are the same.

4.2.5. Cycle Accumulation Study

One of the objectives of this thesis was to predict how much the turbine blade deforms throughout its lifetime. So far, this work has been focused on the U2 displacement results for a single flight cycle with cooling periods. Therefore, in order to properly make a prediction of the deformation the blade endures, it was necessary to acquire information regarding the blade's lifetime, the airplane's turnaround time for the PDL-FNC flight cycle, and the rest time after a day's work.

In the thesis of which this study is a continuation, it was possible to find that the duration of the blade's lifetime is 3000 flight hours [2]. From these 3000 flight hours, and knowing that a flight cycle for the PDL-FNC airway takes 7492 s between the engine starting and its shutdown, the number of cycles that the blade can go through could be calculated. Therefore, a turbine blade can perform for 1442 flight cycles (C) before having to be replaced.

In order to base this study in reality as much as possible, the turnaround time information was obtained from the airline. The turnaround time, which is the time between the plane landing and taking off again is, for the flight in question, approximately 30 minutes or 1800 s.

With the knowledge of both the flight cycle time and the turnaround time, it was defined that each cycle studied would begin at the start of the flight cycle time and would close at the end of the turnaround time.

As for the rest time, it was first necessary to know how many flight hours are registered by the airplane during a workday - defined by the sum of block hours, which is the time between the closing of the airplane's door before departure and the opening of the door upon arrival at the gate. According to the airline, during peak season, an airplane can register up to 11/12 flight hours a day – approximately 6 PDL-FNC flight cycles. Therefore, the rest time can be assumed to be in the vicinity of 10 hours a day (36000 s). However, given that the ABAQUS finite element software takes approximately 4 hours to perform both the thermal and creep analyses for a single flight cycle with turnaround time (7492 s + 1800 s = 9292 s), adding a 36000 s rest time after every 6 flight cycles was considered to be too time-consuming. Hence, the rest time (R) considered was 10400 s, which is a

time period that allows for the complete cooling of the blade in the CBC analysis. This was considered to be a fair compromise, as during the rest time, the engine has enough time to completely cool down before the next workday. This rest time though, is added after the flight cycle time and not after the turnaround time, and so, at the end of every 6th cycle there is no turnaround time. However, this does not change how the cycles are defined, and so, the U2 displacements are obtained at the end of the flight cycle with turnaround time (a time instant of the rest time that would be the equivalent of the turnaround time), in order to maintain a coherence between all cycle analyses.

Also of relevance is the fact that for these analyses, a finite element with a seed size of 1.8 mm was used instead of the 1 mm seed size element used in the analyses made in **Chapter 4**. This choice was made due to the amount of time that an analysis takes when using a 1 mm element, which is considerably superior to the amount of time that it takes to make one with a 1.8 mm element, due to a larger refinement of the mesh when using an element with a 1 mm seed size. However, the results obtained when using the 1.8 mm element are fairly close to those obtained when using a 1 mm element, as the errors for points 1, 2 and 3 are respectively 2.06 %, 11,2 % and 6.1 %. Therefore, the results obtained by the analyses when using an element with an 1.8 mm seed size were considered to be reliable.

With this information, an analysis of 4 airplane workdays and two extra cycles when using the second set of convection coefficients, was performed by ABAQUS, which is to say, 4(6 Cycles + Rest) + 2 Cycles, or 26 cycles and 4 rest periods in total. These analyses were both TBC and CBC creep analyses, and the U2 displacement results at the end of each cycle were obtained, as well as the U2 displacement trendlines. These trendlines – power and logarithmic trendlines - were chosen for each set of displacement results by selecting the trendline with the highest correlation coefficient (R^2). The results obtained can be viewed in **Figures 4.48** through **4.51**.
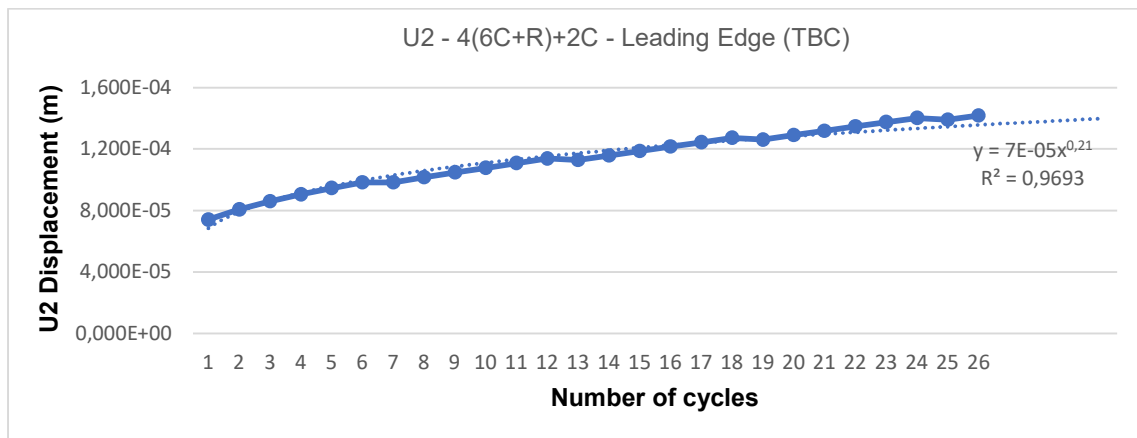
Figure 4.48 - Displacement (U2) and trendline of the leading edge for 4(6C+R)+2C (TBC)
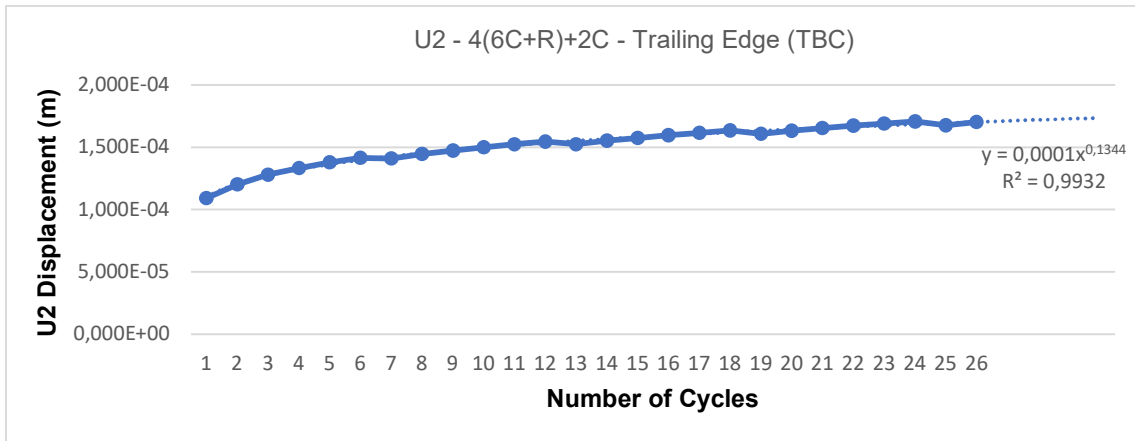
Figure 4.49 - Displacement (U2) and trendline of the trailing edge for 4(6C+R)+2C (TBC)
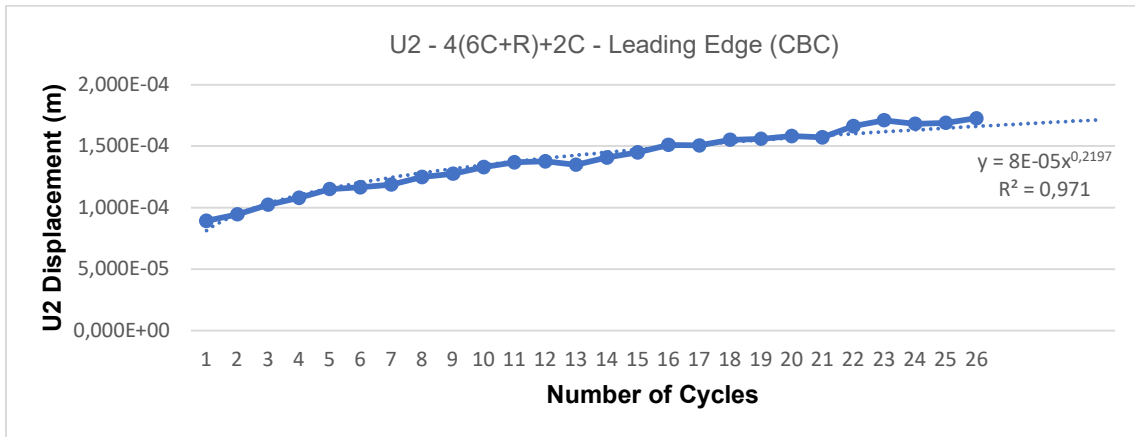
Figure 4.50 - Displacement (U2) and trendline of the leading edge for 4(6C+R)+2C (CBC)
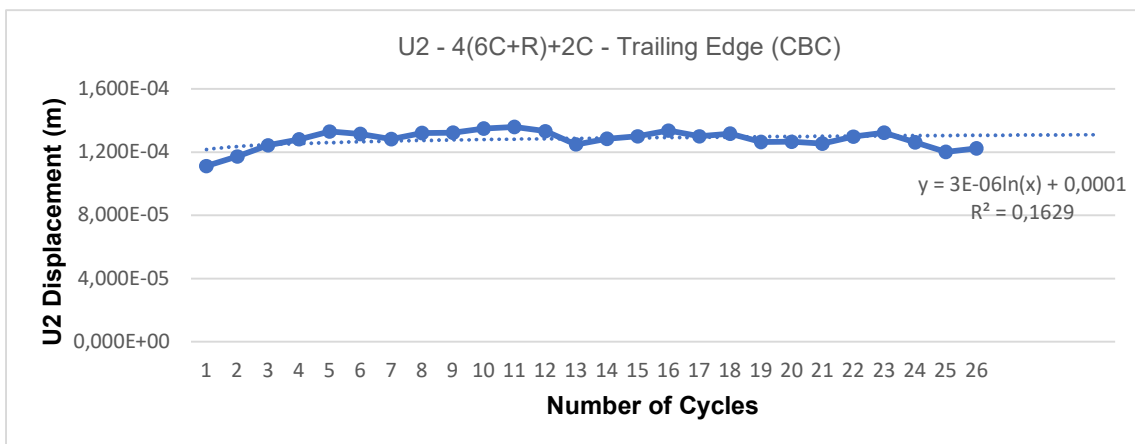
Figure 4.51 - Displacement (U2) and trendline of the trailing edge for 4(6C+R)+2C (CBC)

With the trendlines obtained from the cycle analyses for all cycles, and knowing that the blade has a lifetime of 1442 cycles, a prediction of the deformation at the end of the blade's lifetime could be calculated. These results can be consulted in **Table 4.20**. Also, the U2 displacement of the blade after the conclusion of the 26th cycle can be viewed in **Figure 4.52**.
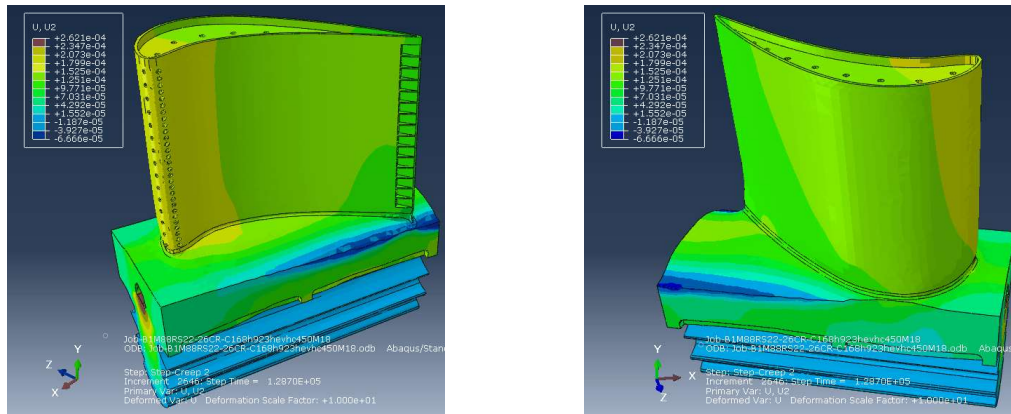
Figure 4.52 - U2 displacement distribution of the turbine blade for the second set of convection coefficients after the 26th cycle (CBC)

Table 4.20 - Displacement (U2) of the turbine blade for 1442 cycles based on the U2 trendlines (TBC and CBC)

Study Points	U2 (m) (1442 cycles)	
	U2 Trendlines - TBC	U2 Trendlines - CBC
	4(6C+R)+2C	4(6C+R)+2C
Point 1 - Leading Edge	3.225E-04	3.955E-04
Point 2 – Center of Convex Surface	1.182E-04	2.645E-04
Point 3 - Trailing Edge	2.658E-04	1.218E-04

Analyzing the results, it is possible to see that, somewhat unexpectedly, the U2 displacement values of the leading end of the blade are higher in the CBC creep analyses than the ones obtained in the TBC creep analyses. However, when taking into account that in the TBC analysis the uniform cooling period of the blade is inferior to the turnaround time, it is easy to understand that at the end of the turnaround time, the blade has achieved a uniform temperature of 20 ºC. On the other hand, for the CBC analysis, the uniform cooling period is significantly larger than the turnaround time, and the blade is still at temperatures between 35 ºC and 51 ºC when the turnaround time ends and the airplane takes off again, beginning a new cycle. Therefore, because in the TBC analysis the blade cools down faster than in the CBC analysis, the contraction of the blade in the TBC analysis will also be superior. The rest time helps in attenuating this effect for the CBC analysis – this can be confirmed by the graphical results for all analyses where it is possible to see that at the 7th cycle (which already

takes into account the rest time after the 6th cycle) there is a drop or a stabilization of the U2 displacement (this can also be seen at the 13th, 19th and 25th cycle, after every rest time). During the rest time the blade has an opportunity to cool down to 20 ºC and, by consequence, experience a larger contraction than during the turnaround time. Still, these results do not contradict the conclusions regarding the CBC approach obtained previously in the analyses for 1 cycle, as an engine takes 2 to 4 hours to completely cool down, and the blade temperatures registered at the end of the turnaround time are very low compared to the temperatures that it experiences during the flight.

Another unexpected observation from the results obtained from the TBC and CBC analyses, in the sense that they appear to contradict the ones obtained for a single flight cycle, is the fact that it is now the leading edge that presents the highest U2 displacement values, as can be seen in **Figure 4.52**. In fact, in the CBC analysis – the one closest to reality - the entire leading end of the blade deforms significantly more than the trailing edge.

A possible explanation for why the trailing edge deforms less than the leading edge lies in the width of the blade. For 1 cycle, as previously seen, the lack of internal space near the trailing edge resulted to its detriment as there was a small amount of cooling flow decreasing the trailing edge's temperature, which naturally lead to higher U2 displacement values. On the opposing side, due to a larger width and therefore more cooling air in the hollow spaces, the leading end of the blade presents lower displacement values. However, as the cycles keep accumulating, the small widths of the trailing edge, and therefore lack of significant internal space nearby, results in its favor. As the cycles add up, the trailing edge deforms at a lower rate than the leading end, with the results being that the leading end of the blade, by the end of the blade's lifetime, has deformed more than the trailing edge, and so presents higher U2 displacement values. As for the leading end, the leading edge still presents higher U2 displacement values than the ones obtained in the center of the convex surface, as previously seen in the analyses for 1 cycle.

An important note to make is that, for one cycle, in which the thermal load significantly impacts the blade's deformation, the material deforms by plasticity and creep mechanisms, with the higher percentage of deformation being necessarily attributed to plasticity. However, on the second cycle, and as the cycles add up, the plasticity percentage of deformation decreases – and strain hardening factors in - and creep becomes the dominant mechanism of deformation.

Even though the results obtained are merely predictions based on 26 cycles, overall, one can conclude that the U2 displacement values by the end of the blade's lifetime can be considered very reasonable, as the blade has deformed, at most, less than half a millimeter (0.3955 mm). This seems to coincide with reality, as these blades are substituted by new ones at the end of their lifetime, before significant deformation occurs.

5. Conclusions

At the conclusion of this work, it is possible to state that a finite element model for temperature and deformation of a gas engine turbine blade taking into account different cooling modes was developed. Certain assumptions, approximations and simplifications had to be made though, as precise information regarding the blade's material and flow convection coefficients is difficult to come by. For this reason, rectangular blocks with several cooling channel configurations were studied, so as to establish the consistency of the proposed approach. This allowed the assumptions and approximations made to be considered reasonable and leading to results that both for block geometries and for a blade shape are fairly close to what could be expected in reality. The main conclusions that were taken from this work can be read below:

- The B0 block geometry with no cooling channels displayed the highest U2 displacement results;

- The B4-11L/17T block geometry proved to be the most efficient at distributing the cooling flow and, by consequence, reducing its internal temperatures - in general, block geometries with both longitudinal and transversal cooling channels exhibit lower internal temperatures, and therefore superior cooling efficiency, than geometries with solely longitudinal cooling channels;

- The B2-14L geometry displayed lower U2 displacement values when compared to the other geometries – in general, block geometries with solely longitudinal channels exhibited lower U2 displacements/higher contractions when compared to geometries with both longitudinal and transversal cooling channels;

- Geometries with a higher number of longitudinal cooling channels (and no transversal channels), displayed in a single line at the middle of the width of the symmetrical block, exhibit lower U2 displacements;

- The distribution of mass at the top of the block has to be taken into consideration when examining the U2 displacement at the top of the block;

- The geometry that, U2 displacement results-wise, is closest to the blade model is the B3-7L/11T geometry;

- With the increase of the cooling flow's convection coefficient, comes a decrease of the temperature of the block/blade and a decrease of the U2 displacement values;

- The CBC creep analysis, which utilizes the temperature results obtained by the CBC thermal analysis, seems to be a more realistic approach than the TBC creep analysis;

- The rectangular block model proved to be a successful model in establishing the consistency of the thermal and creep analyses before their implementation in the blade model;

- For one flight cycle and cooling periods, the blade exhibits its lowest U2 displacement values where its widths are the largest (with the center of the convex surface exhibiting the lowest displacement), and its highest U2 displacement values where its widths are the smallest (with the trailing edge exhibiting the highest displacement);

- For one flight cycle and for the ranges of heat transfer coefficients that were analyzed, the U2 displacements for both the CBC and the TBC analysis are within the same order of magnitude;

- By the end of the blade's lifetime, the leading edge displays the highest U2 displacements, and the trailing edge displays the lowest; these displacement results are in the sub-millimeter range and they are similar for both the CBC and the TBC analysis;

- The cycle accumulation study provided a solid prediction of the blade's deformation by the end of its lifetime;

Overall, in conclusion, the rectangular block model provided a suitable model for the validating of the thermal and creep analyses, and the blade model offered reasonable results and proved itself a useful model in analyzing temperatures, U2 displacements and predicting the deformation by the end of the blade's lifetime. This highlights something that is well known, which is how important the cooling channels and cooling dynamics are in minimizing the deformation and maximizing the lifetime of the turbine blade.

5.1. Future Work

For future work, it would be of interest to make a few improvements on the current blade model. Even though the blade studied in this work is very close to the one obtained from the regional airline company, a more precise model could provide different results. Also, new flight routes could be studied. The PDL-FNC is the longest flight cycle that this airplane experiences, so a shorter flight cycle could be of interest, especially a cycle accumulation study, as the cruise flight phases of these flights are small.

The most important improvement that could be made is the running of a computational fluid dynamics analysis on the model, as the choices and assumptions made in the development of the CBC thermal analysis regarding the convection coefficients and sink temperatures, offer a somewhat simplistic view of the fluid and heat transfer dynamics at play on the exterior of the turbine blade.

6. References

[1]   OECD, "Airline competition," [Online]. Available:
        https://www.oecd.org/competition/airlinecompetition.htm. [Accessed on August 2021].

[2]   P. M. B. Brandão, "Thermo-mechanical Modeling of a High Pressure Turbine Blade of an
        Airplane Gas Turbine Engine", 2005.

[3]   M. P. Boyce, "An Overview of Gas Turbine," em *Gas Turbine Engineering Handbook*, 2nd ed.,
        Woburn, MA, Butterworth-Heinemann, 2002, pp. 9-15.

[4]   M. P. Boyce, "Axial-Flow Turbines," em *Gas Turbine Engineering Handbook*, 2nd ed., Woburn
        MA, Butterworth-Heinemann, 2002, pp. 351-363.

[5]   LibreTexts, "Brayton Cycle," Chemistry Library, 15 August 2020. [Online]. Available:
        https://chem.libretexts.org/Bookshelves/Physical_and_Theoretical_Chemistry_Textbook_Map
        s/Supplemental_Modules_(Physical_and_Theoretical_Chemistry)/Thermodynamics/Thermody
        namic_Cycles/Brayton_Cycle. [Accessed on October 2021].

[6]   S. Abed, K. Tahar e A. Ben Brahim, "Thermodynamic and Energy Study of a Regenerator in
        Gas Turbine Cycle and Optimization of Performances," April 2016.

[7]   C. L. Proctor II, Encyclopedia of Physical Science and Technology - Third Edition, Elsevier
        Science Ltd. , 2001.

[8]   R. E. Sonntag e C. Borgnakke, Introduction to Engineering Thermodynamics - Second Edition,
        John Wiley & Sons, Inc., 2006.

[9]   NASA, "Turboprop Engine," NASA - National Aeronautics and Space Administration, [Online].
        Available: https://www.grc.nasa.gov/www/k-12/airplane/aturbp.html. [Accessed on October
        2021].

[10]   Waqar, "What is a Turboprop? How does a Turboprop Engine work?," Mechanical Boost,
        [Online]. Available: https://mechanicalboost.com/turboprop/. [Accessed on October 2021].

[11]   Michael, "CBT and the Q400," Mike's Flying, 2012. [Online]. Available:
        http://mikesflying.blogspot.pt/2012/08/cbt-and-q400.html. [Accessed on October 2021].

[12]   Bombardier, "Engine, General," em *Aircraft Maintenance Manual - System Description
        Section*, Montreal, Canada, Bombardier, 2008.

[13]   Bombardier, "Turbines," em *Aircraft Maintenance Manual - System Description Section*,
        Montreal, Canada, Bombardier, 2008.

[14]   Bombardier, "Power Turbines," em *Aircraft Maintenance Manual - System Description Section*,
        Montreal, Canada, Bombardier, 2008.

[15]   T. Okura, "Materials for Aircraft Engines," 2015. [Online]. Available:
        https://www.colorado.edu/faculty/kantha/sites/default/files/attached-files/73549-116619_-
        _takehiro_okura_-_dec_17_2015_1027_am_-_asen_5063_2015_final_report_okura.pdf.
        [Accessed on October 2021].

[16]   VBR Turbine Partners, "VBR Turbine Partners," VBR Turbine Partners, [Online]. Available:
        https://vbr-turbinepartners.com/l47459g03/. [Accessed on October 2021].

[17]   J. Han e L. M. Wright, "Enhanced Internal Cooling of Turbine Blades and Vanes," em *The Gas*

Turbine Handbook, Morgantown, WV, U.S. Department of Energy-National Energy Technology Laboratory (NETL), 2006, pp. 321-354.

[18]   J. Han, "Recent Studies in Turbine Blade Cooling," em *Int. J. Rotating Mach*, vol. 10, 2004, pp. 443-457.

[19]   D. G. Bogard e K. A. Thole, "Gas Turbine Film Cooling," em *J. Propuls. Power*, vol. 21, 2005, p. 24.

[20]   K. P. Shah, "The Hand Book on Mechanical Maintenance," Practical Maintenance, [Online]. Available: https://practicalmaintenance.net/?p=989. [Accessed on October 2021].

[21]   Academic Resource Center, "Creep Deformation in Materials," Illinois Tech. [Online]. [Accessed on October 2021].

[22]   M. Danylenko, "Why Design Engineers Should Consider Creep Resistance of Materials," Matmatch, 25 July 2018. [Online]. Available: https://matmatch.com/resources/blog/materials-creep-resistance/. [Accessed on October 2021].

[23]   W. D. Callister Jr., Materials Science and Engineering: An Introduction (7th Edition), John Wiley and Sons, Inc., 2007.

[24]   West Virginia University, *Materials at High Temperature, Creep,* 2015.

[25]   F. P. Incropera e D. P. DeWitt, Fundamentals of Heat and Mass Transfer, Fifth Edition, New York: John Wiley & Sons, Inc, 2002.

[26]   Machine Design, "What's the Difference Between Conduction, Convection, and Radiation?," Machine Design, 30 October 2015. [Online]. Available: https://www.machinedesign.com/learning-resources/whats-the-difference-between/document/21834474/whats-the-difference-between-conduction-convection-and-radiation. [Accessed on October 2021].

[27]   Simscale, "What is Heat Transfer?," Simscale, 2 September 2021. [Online]. Available: https://www.simscale.com/docs/simwiki/heat-transfer-thermal-analysis/what-is-heat-transfer/. [Accessed on October 2021].

[28]   Wikipedia, "Convection (heat transfer)," Wikipedia, 25 November 2021. [Online]. Available: https://en.wikipedia.org/wiki/Convection_(heat_transfer). [Accessed on October 2021].

[29]   Software Cradle Co., Ltd, "Natural Convection," Software Cradle Co., Ltd, [Online]. Available: https://www.cradle-cfd.com/technology/glossary/ja_K/detail0052.html. [Accessed on October 2021].

[30]   Boyd Corporation, "What is Buoyancy?," Boyd Corporation, [Online]. Available: https://blog.boydcorp.com/buoyancy-drives-natural-convection.html. [Accessed on October 2021].

[31]   Bombardier, "First Bombardier Q400 NextGen Airliner Headed to SATA Air Açores of the Azores, Portugal," Bombardier, 24 January 2010. [Online]. Available: https://bombardier.com/en/media/news/first-bombardier-q400-nextgen-airliner-headed-sata-air-acores-azores-portugal. [Accessed on October 2021].

[32]   Axel, "GRABCAD Community," 8 Sept 2020. [Online]. Available: https://grabcad.com/library. [Accessed on January 2021].

[33]   Wikipedia, "Snecma M88," [Online]. Available: https://en.wikipedia.org/wiki/Snecma_M88.

[Accessed on January 2021].

[34]   Wikipedia, "Turbine blade," [Online]. Available: https://en.wikipedia.org/wiki/Turbine_blade. [Accessed on August 2020].

[35]   R. C. Reed, T. Tao e N. Warnken, "Alloys-By-Design: Application to nickel-based single crystal superalloys," em *Acta Mater. vol 57, no.19*, 2009.

[36]   Wikipedia, "De Havilland Canada Dash 8," [Online]. Available: https://en.wikipedia.org/wiki/De_Havilland_Canada_Dash_8. [Accessed on September 2020].

[37]   M. Abdo, P. Piperni, A. T. Isikveren e F. Kafyeke, "Optimization of a Business Jet," em *Canadian Aeronautics and Space Institute Annual General Meeting*, 2005.

[38]   R. Seresinhe, C. Lawson, A. Shinkafi, D. Quaglia e I. Madani, "Airframe Systems Power Off-Take Modelling in More-Electric Large Aircraft for Use in Trajectory Optimisation," em *29th Congress of the International Council of the Aeronautics Sciences*, St Petersburg, Russia, 2014.

[39]   Aerodynamics for students, "Standard Atmosphere Computations," [Online]. Available: http://www.aerodynamics4students.com/properties-of-the-atmosphere/atmosphere7.php. [Accessed on October 2020].

[40]   Engineers Edge, "Overall Heat Transfer Coefficient Table Chart," [Online]. Available: https://www.engineersedge.com/thermodynamics/overall_heat_transfer-table.htm. [Accessed on October 2020].

[41]   A. H. Ayaal, J. M. Jalil e K. K. Abbas, "Thermal Analysis of a Cooled Turbine Blade," em *2nd International Conference on Sustainable Engineering Techniques*, Baghdad, Iraque, 2019.

[42]   G. Creci, M. Teixeira de Mendonça, J. C. Menezes e J. R. Barbosa, "Heat Transfer Analysis in a Single Spool Gas Turbine" *Applied Sciences,* 24 November 2020.

[43]   Quora, "How long does it take for an aircraft engine to cool down to room temperature from the point it is turned off by the pilot?," Quora. [Online]. Available: https://www.quora.com/How-long-does-it-take-for-an-aircraft-engine-to-cool-down-to-room-temperature-from-the-point-it-is-turned-off-by-the-pilot. [Accessed on May 2021].

Appendix

Appendix A – Mesh Convergence

The choice of mesh with which to run simulations is paramount, as they define the precision of the results obtained. To evaluate the precision of the results, several creep analyses were performed using meshes of heat transfer and 3D stress elements with different seed sizes. The results for all the U2 displacements and their corresponding errors were tabulated for both a baseless block model and the blade model. These results can be seen in **Table A.1** and **A.2**.

Table A.1 - Mesh convergence and errors for a baseless block model (TBC)

Seed Size (mm)	Number of nodes	U2 (m)	Error (%)	U2 (m)	Error (%)	U2 (m)	Error (%)
		Point 1		Point 2		Point 3	
1.75	37928	-3.01E-06	-	-4.61E-06	-	-4.59E-06	-
1	45893	-3.33E-06	10.78	-4.91E-06	6.45	-4.90E-06	6.55
0.5	86320	-3.41E-06	2.35	-4.98E-06	1.52	-4.97E-06	1.55
0.35	156553	-3.49E-06	2.35	-5.05E-06	1.39	-5.04E-06	1.37
0.25	415943	-3.51E-06	0.52	-5.06E-06	0.12	-5.04E-06	0.11

Table A.2 - Mesh convergence and errors for the blade model (TBC)

Seed size (mm)	Number of nodes	U2 (m)	Error (%)	U2 (m)	Error (%)	U2 (m)	Error (%)
		Point 1		Point 2		Point 3	
1.8	161365	7,78E-05	-	6,42E-05	-	1,14E-04	-
1.4	239106	7,92E-05	1,82	6,63E-05	3,23	1,13E-04	-1,36
1	347280	7,94E-05	0,17	7,14E-05	7,63	1,07E-04	-4,9
0.85	417373	7,94E-05	0,11	7,13E-05	-0,16	1,07E-04	0,21

From the study of these results, it was concluded that the use of a mesh composed of elements with a seed size of 1 mm was appropriate for the obtaining of solid results. This 1 mm seed size produced small errors when compared to smaller seed sizes, and so it was not necessary to over-refine the mesh, as this would lead to a much longer computing time.

Appendix B – Convection Coefficient Study for a Baseless Block

To study the effect of the convection coefficient on baseless block geometries (**Figure B.1**), several TBC simulations were run using different convection coefficients. The temperature results obtained using the first convection coefficient h=500 W/m^{2}K were compared to those obtained using both a four times smaller (125 W/m^{2}K) and four times larger (2000 W/m^{2}K, already in the domain of forced convection using liquids) convection coefficients. These results can be seen in **Table B.1**.
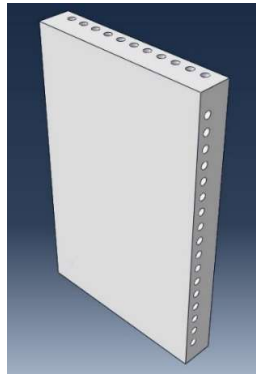

Figure B.1 - Baseless BB4-11L/17T rectangular block

Table B.1 - Convection coefficient study for the baseless BB4-11L/17T rectangular block

Baseless Block Geometry	h (W/m^{2}K)	Time (s)	Temperature (ºC)	
			Wall Temperature	Minimum Temperature
BB1-7L	125	≈ 3000	750	734.1
	500	≈ 3000	750	688.3
	2000	≈ 3000	750	528.3
BB2-14L	125	≈ 3000	750	729.1
	500	≈ 3000	750	669.5
	2000	≈ 3000	750	471.3
BB3-7L/11T	125	≈ 3000	750	728.3
	500	≈ 3000	750	666.4
	2000	≈ 3000	750	460.4
BB4-11L/17T	125	≈ 3000	750	724.9
	500	≈ 3000	750	654.1
	2000	≈ 3000	750	426.5

From the study of these results, it is possible to conclude that, for all geometries, an increase of the convection coefficient leads to the decrease of the minimum temperatures. This leads to the conclusion that as the convection coefficient rises, so does the temperature performance of the cooling flow in lowering the blocks' temperatures. This conclusion was also obtained in **Chapter 4**.

The results also demonstrate that when using liquid as the refrigerating fluid, it is possible to achieve drastically lower temperatures than when using air as the refrigerating fluid.

Finally, like the rectangular blocks studied in **Chapter 4**, the baseless block geometries with both longitudinal and transversal cooling channels are more efficient at reducing the blocks' temperatures than geometries with solely longitudinal channels. Again, this coincides with the conclusions drawn in **Chapter 4,** concerning the thermal efficiency of the rectangular blocks.

Appendix C – Creep results of stresses and strains

TBC Creep Analysis

The graphical results of the variables von Mises stress (SMises), stress in the longitudinal direction (S22), strain in the longitudinal direction (E22) and displacement magnitude (UMag), are presented in **Figures C.1** through **C.4** for the B2-14L and the B3-7L/11T rectangular block geometries. As for the numerical results of the same variables for the points at the top of the block, they can be seen in **Table C.1** for all block geometries.
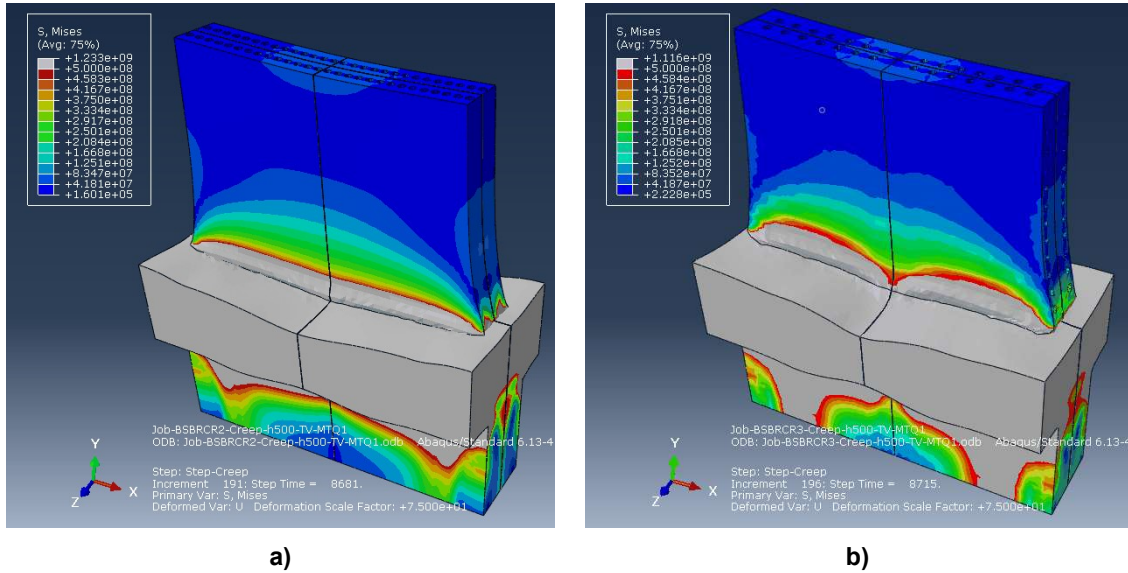

a)   **b)**

Figure C.1 - von Mises stress SMises distribution for the a) B2-14L geometry; b) B3-7L/11T geometry (TBC)
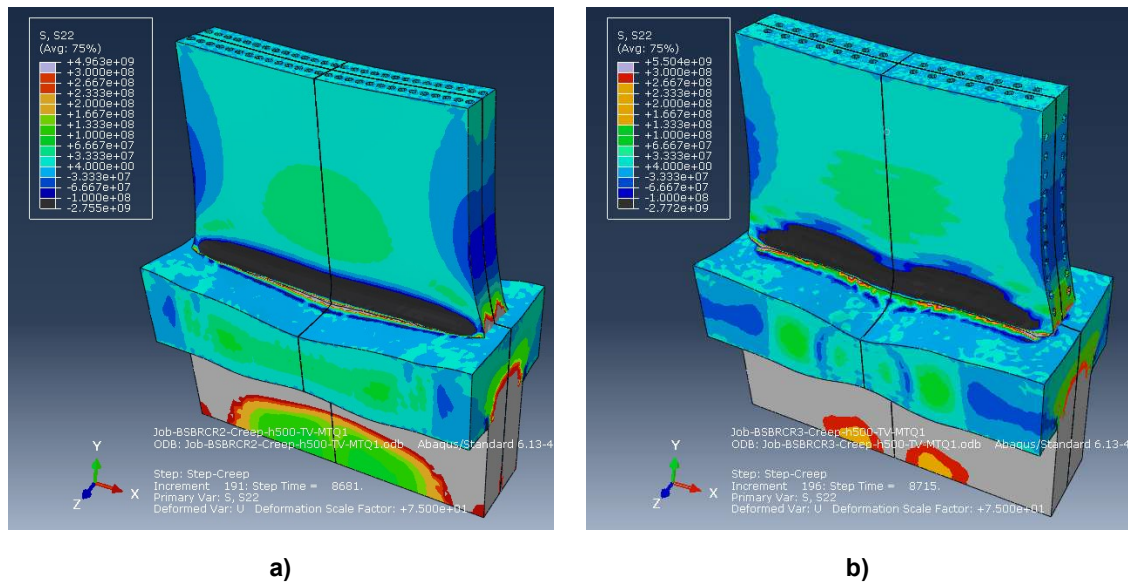

a)   **b)**

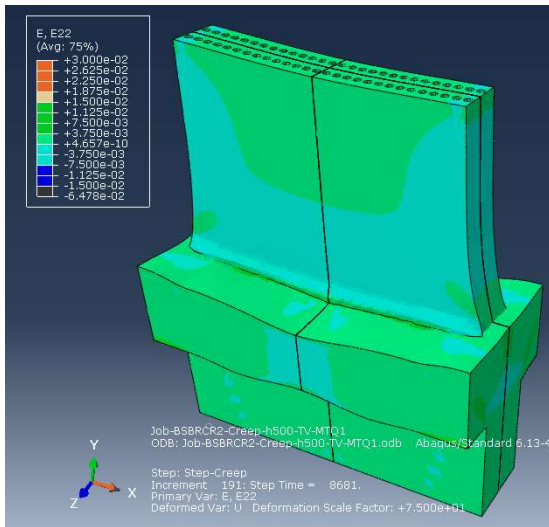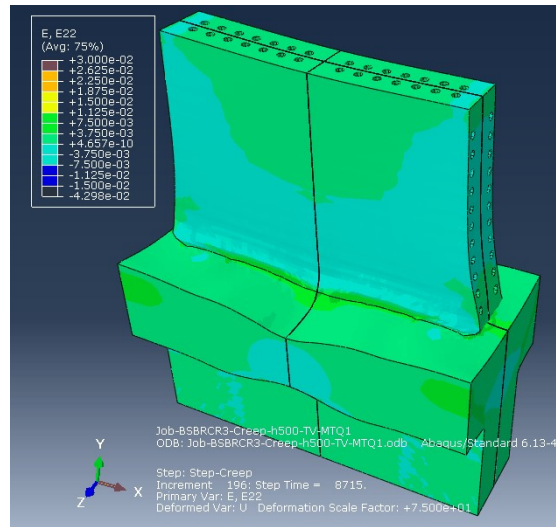**Figure C.2 - Stress in the longitudinal direction S22 distribution for the a) B2-14L geometry; b) B3-7L/11T geometry (TBC)**
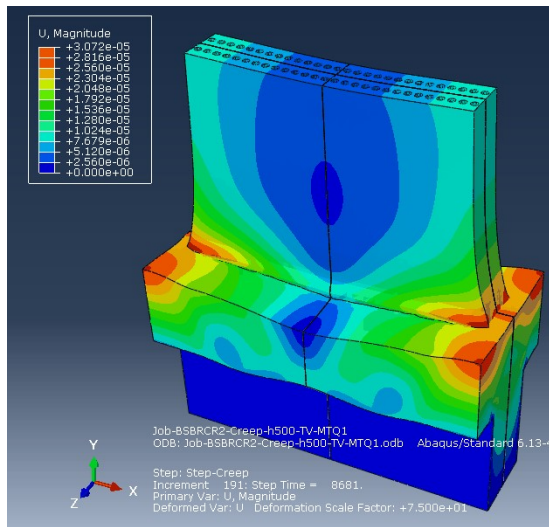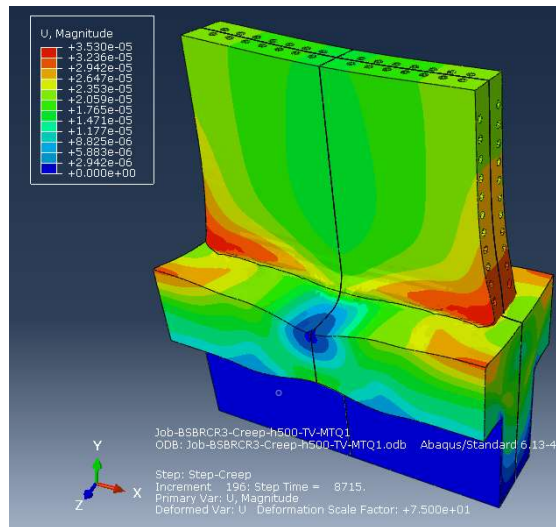
Figure C.3 - Strain in the longitudinal direction E22 distribution for the a) B2-14L geometry; b) B3-7L/11T geometry (TBC)

Figure C.4 - Displacement magnitude UMag distribution for the a) B2-14L geometry; b) B3-7L/11T geometry (TBC)

Table C.1 - Creep analysis results of the SMises, S22, E22, UMag variables for the rectangular block geometries (TBC)

Points	SMises (Pa)	S22 (Pa)	E22	UMag (m)
h = 500 W/m²K				

Points	SMises (Pa)	S22 (Pa)	E22	UMag (m)
B0 Block Geometry				
1	3.119E+07	-3.640E+04	7.502E-05	8.751E-05
2	6.279E+07	-5.355E+04	1.392E-04	8.578E-05
3	6.196E+07	7.682E+03	1.365E-04	8.570E-05
4	6.712E+05	2.438E+05	1.375E-06	9.069E-05
B1-7L Block Geometry				
1	2.717E+07	8.373E+05	8.210E-05	1.021E-05
2	7.614E+07	-8.529E+05	1.326E-04	7.918E-06
3	6.008E+07	-8.987E+05	1.492E-04	7.898E-06
4	7.890E+05	1.588E+05	1.175E-06	1.426E-05
B2-14L Block Geometry				
1	3.056E+07	-5.258E+04	8.693E-05	5.881E-06
2	6.352E+07	1.864E+05	1.588E-04	3.305E-06
3	5.907E+07	-4.322E+05	1.570E-04	3.269E-06
4	6.225E+05	4.162E+04	7.707E-07	9.767E-06
B3-7L/11T Block Geometry				
1	2.561E+07	-1.238E+05	7.842E-05	1.941E-05
2	4.068E+07	2.330E+05	1.221E-04	1.738E-05
3	5.037E+07	-1.140E+05	1.350E-04	1.733E-05
4	5.304E+05	2.729E+04	3.174E-07	2.318E-05
B4-11L/17T Block Geometry				
1	2.487E+07	-2.984E+05	8.054E-05	1.508E-05
2	4.824E+07	-4.384E+05	1.282E-04	1.298E-05
3	5.186E+07	-3.091E+05	1.410E-04	1.294E-05
4	6.821E+05	7.906E+04	7.270E-07	1.889E-05
B5-11L/11L Block Geometry				
1	2.698E+07	2.110E+06	1.039E-04	8.754E-06
2	5.315E+07	-1.339E+04	1.242E-04	6.448E-06
3	4.881E+07	-4.516E+05	1.330E-04	6.388E-06
4	6.726E+05	1.199E+04	6.811E-07	1.287E-05
B6-11L/17 - Net Block Geometry				
1	2.686E+07	1.783E+05	8.237E-05	1.202E-05
2	5.993E+07	3.685E+05	1.506E-04	9.865E-06
3	5.615E+07	-3.413E+05	1.502E-04	9.805E-06
4	5.623E+05	2.342E+04	5.126E-07	1.583E-05

From the graphical analyses results in **Figures C.1** through **C.4** it is observable that, in general and despite a few differences, there is a certain consistency between the results obtained for both the B2-14L and B3-7L/11T block geometries, as examples of a geometry with solely longitudinal cooling channels and one with both longitudinal and transversal cooling channels.

Looking at the variables' results and starting with SMises and S22 stress, it is easily seen that the higher values of stress are located at the bottom of the blocks, by their base. This is most likely due to the constraints applied at the base by the boundary conditions – it is of note that these areas appear in grey and black due to the adjustment of the limits of the variables' interval values, which was done so that the variable's distribution on the block could be visible.

Also observable on the stress distribution is high values of stress on the block's trailing and leading edge, and also, in smaller distribution, on the top of the block. In the S22 distribution, it is visible that these stresses are compressive stresses while in the center part of the block there is a predominance of tensile stresses.

As for the strains, as expected, they follow somewhat the same pattern of behavior as the stresses, as the compressive strains are mostly situated at the leading and trailing edge, as well as in sections near the base, and the tensile strains are mostly located from the mid-block up until its top.

Taking into account that the UMag variable has a similar graphical behavior to the U2 variable, the study of its distribution was made in **Chapter 4**.

CBC Creep Analysis

The graphical results of the variables von Mises stress (SMises), stress in the longitudinal direction (S22), strain in the longitudinal direction (E22) and displacement magnitude (UMag), are presented in **Figures C.5** through **C.8** for the B2-14L and the B3-7L/11T rectangular block geometries. As for the numerical results of the same variables for the points at the top of the block, they can be seen in **Table C.2** for all block geometries.
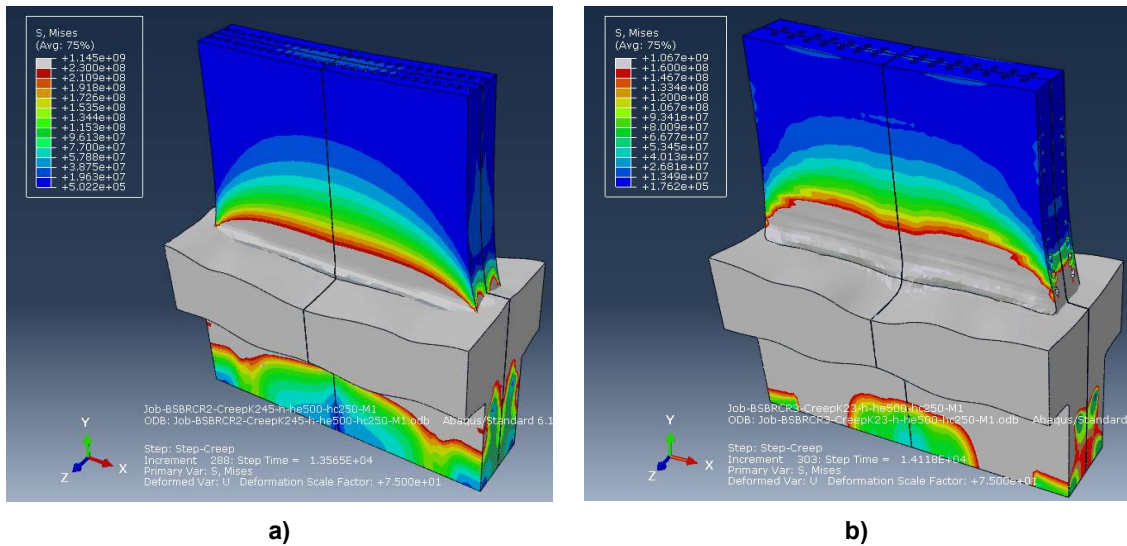

a)   b)

Figure C.5 - von Mises stress SMises distribution for the a) B2-14L geometry; b) B3-7L/11T geometry (CBC)
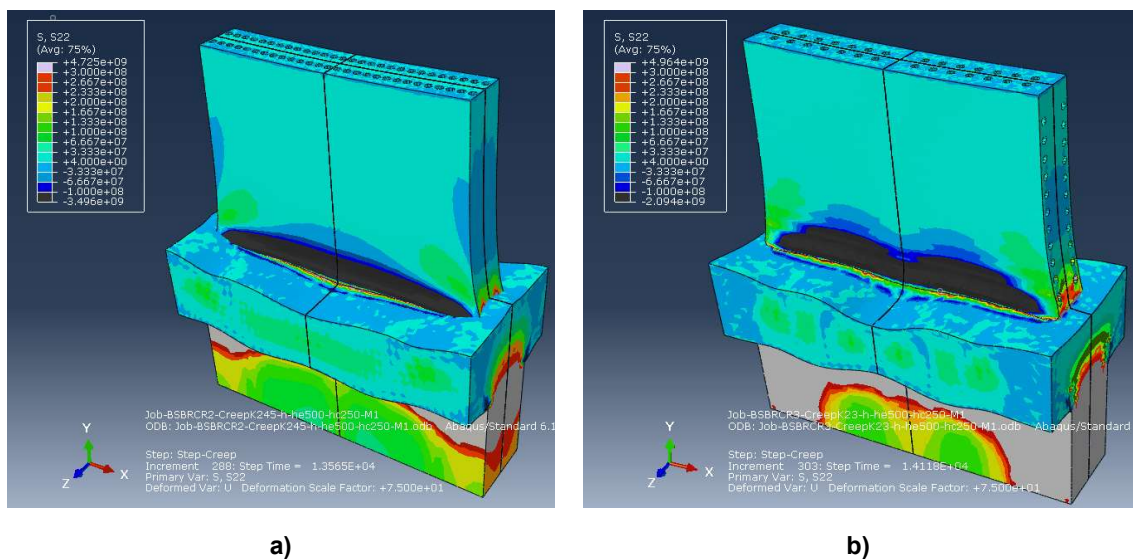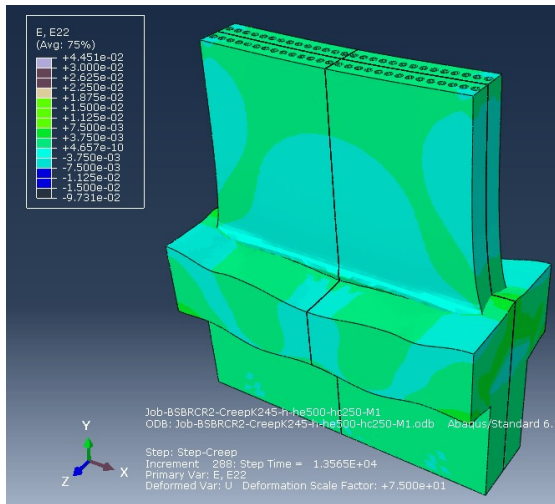

a)   b)

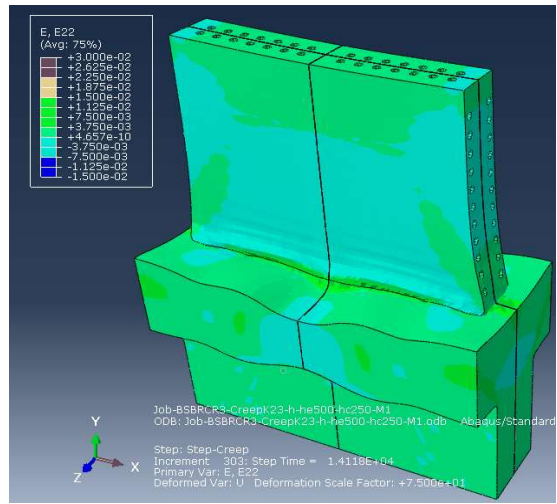**Figure C.6 - Stress in the longitudinal direction S22 distribution for the a) B2-14L geometry; b) B3-7L/11T geometry (CBC)**
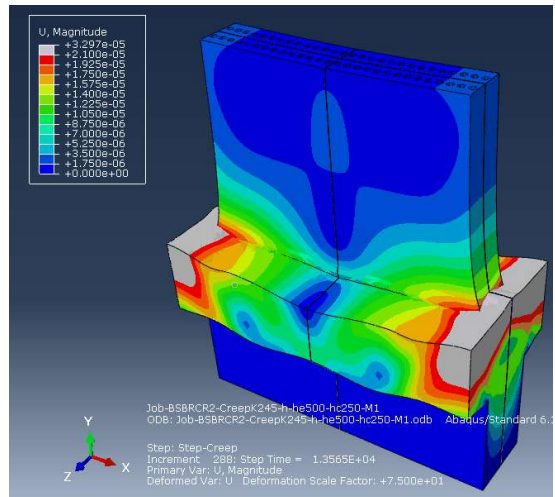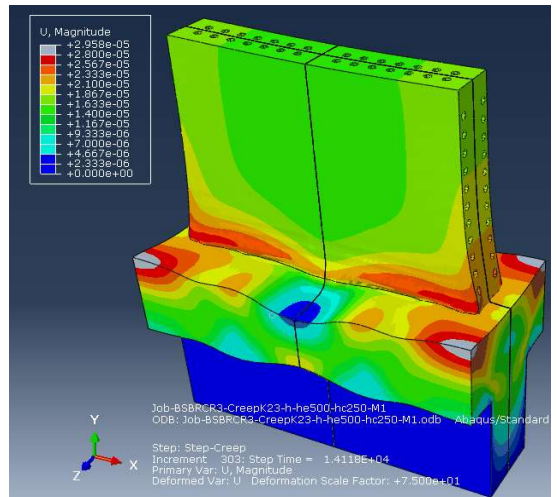
Figure C.7 - Strain in the longitudinal direction E22 distribution for the a) B2-14L geometry; b) B3-7L/11T geometry (CBC)

Figure C.8 - Displacement magnitude UMag distribution for the a) B2-14L geometry; b) B3-7L/11T geometry (CBC)

Table C.2 - Creep analysis results of the SMises, S22, E22, UMag variables for the rectangular block geometries (CBC)

Points	SMises (Pa)	S22 (Pa)	E22	UMag (m)
h=500 W/m²K ; he=500 W/m²K ; hc=250 W/m²K				
	B0 Block Geometry			
1	2.868E+07	-3.577E+04	7.191E-05	7.599E-05
2	5.683E+07	-5.015E+04	1.353E-04	7.432E-05
3	5.607E+07	8.118E+03	1.324E-04	7.424E-05
4	6.274E+05	2.284E+05	1.317E-06	7.904E-05
	B1-7L Block Geometry			
1	5.071E+06	3.871E+05	6.085E-05	3.262E-06
2	4.032E+07	-4.682E+05	7.811E-05	1.665E-06
3	1.967E+07	-5.928E+05	9.526E-05	1.661E-06
4	6.609E+05	-5.038E+04	2.973E-07	6.014E-06
	B2-14L Block Geometry			
1	6.289E+06	-2.512E+05	6.546E-05	1.284E-06
2	2.589E+07	8.214E+04	9.020E-05	1.600E-06
3	2.333E+06	-4.208E+05	9.593E-05	1.610E-06
4	7.212E+05	-1.246E+05	-4.099E-07	2.511E-06
	B3-7L /11T Block Geometry			
1	1.762E+07	-2.311E+05	7.194E-05	1.578E-05
2	1.367E+07	1.514E+05	6.294E-05	1.464E-05
3	1.789E+06	-1.077E+05	7.892E-05	1.463E-05
4	3.580E+05	-1.415E+05	-2.448E-07	1.818E-05
	B4-11L/17T Block Geometry			
1	2.685E+07	-3.361E+05	7.733E-05	1.190E-05
2	1.507E+07	-2.432E+03	6.799E-05	1.078E-05
3	1.322E+07	-2.573E+05	9.060E-05	1.078E-05
4	7.717E+05	-2.879E+05	-6.628E-07	1.422E-05
	B5-11L/11L Block Geometry			
1	3.586E+07	-8.441E+05	1.020E-04	9.448E-07
2	1.455E+07	-3.330E+04	4.042E-05	5.302E-07
3	6.363E+06	-3.162E+05	4.171E-05	5.622E-07
4	9.071E+05	-3.985E+05	-7.020E-07	2.918E-06
	B6-11L/17T - Net Block Geometry			
1	4.514E+06	-1.877E+05	6.446E-05	4.338E-06
2	2.613E+07	2.491E+05	9.210E-05	2.953E-06
3	8.048E+06	-4.579E+05	9.599E-05	2.937E-06
4	6.105E+05	-2.198E+05	2.352E-07	6.823E-06

Like in the TBC creep analysis, the graphical results in **Figures C.5** through **C.8** reveal that, in general and despite a few differences, there is a certain consistency between the results obtained for both the B2-14L and B3-7L/11T block geometries.

As for the comparison between these results and the ones obtained in the TBC creep analysis, the graphical results obtained above indicate that they are not dissimilar to those from the TBC creep analysis, as they follow somewhat close patterns to those results.

Despite the usage of a different type of thermal analysis in this CBC creep analysis, the same conclusions that were drawn in the TBC analysis can equally be drawn from the graphical results of the stress (SMises and S22) and strain (E22) variables.

Numerically though, these variables' results are not easily comparable as they are somewhat erratic and of unpredictable behavior. However, in most points and block geometries it is noticeable that there is a decrease in the stress and strain values in the CBC creep analysis, as opposed to the TBC analysis. This can possibly be explained by the longer cooling periods of the CBC creep analysis, as the mechanical stresses created by the change in temperature of the material are reduced, due to the temperature changes occurring during a longer period of time.